



Aalborg Universitet

AALBORG UNIVERSITY
DENMARK

Control and Protection of Wind Power Plants with VSC-HVDC Connection

Chaudhary, Sanjay

Publication date:
2011

Document Version
Publisher's PDF, also known as Version of record

[Link to publication from Aalborg University](#)

Citation for published version (APA):
Chaudhary, S. (2011). *Control and Protection of Wind Power Plants with VSC-HVDC Connection*. Department of Energy Technology, Aalborg University.

General rights

Copyright and moral rights for the publications made accessible in the public portal are retained by the authors and/or other copyright owners and it is a condition of accessing publications that users recognise and abide by the legal requirements associated with these rights.

- ? Users may download and print one copy of any publication from the public portal for the purpose of private study or research.
- ? You may not further distribute the material or use it for any profit-making activity or commercial gain
- ? You may freely distribute the URL identifying the publication in the public portal ?

Take down policy

If you believe that this document breaches copyright please contact us at vbn@aub.aau.dk providing details, and we will remove access to the work immediately and investigate your claim.

Control and Protection of Wind Power Plants with VSC-HVDC Connection

By

Sanjay K Chaudhary

A dissertation submitted to

The Faculty of Engineering, Science, and Medicine, Aalborg University
in partial fulfilment of the requirements for the degree of

Doctor of Philosophy



Department of Energy Technology
Aalborg University, Aalborg, Denmark

2011

Aalborg University,
Department of Energy Technology,
Pontoppidanstraede 101, 9220 Aalborg East, Denmark.

Phone: +45 9940 9240

Fax: +45 9815 1411

Web: <http://www.et.aau.dk>

Copyright © Sanjay K Chaudhary, 2011

Printed in Denmark by UniPrint.

ISBN: 978-87-92846-02-0

Abstract

Wind power plants are the fastest growing source of renewable energy. The European Union expects to generate 230 GW wind power, in which the offshore wind power is expected to contribute 40 GW. Offshore wind power plants have better wind velocity profile leading to a higher energy yield. Europe has a huge potential of offshore wind energy, which is a green and sustainable resource. All these have led to the development of offshore wind power plants.

However, overall cost of the offshore installation, operation, and maintenance are higher than those of the onshore wind power plants. Therefore, the plant size needs to be higher such that the unit cost of energy can be lowered. An overall increase in operating efficiency would further reduce the cost of energy, thereby increasing the viability of the project. Multi-MW variable speed wind turbine generators, of unit sizes between 3-10 MW, have been developed so as to take advantage of the lower cost per MW of installed wind power capacity. The current trend is that these large units will comprise of multi-pole, low-speed synchronous generators equipped with full scale converters. VSC-HVDC cable transmission is a favourable option for a large and remote offshore wind power plant, which needs a long distance cable connection to the onshore power grid. It has lower power losses, higher transmission efficiency, and fast control of both the active and the reactive power.

This dissertation presents a test system for the simulation analysis of different operational and control aspects of a potential wind power plant with VSC-HVDC connection to the onshore grid. The test system is modelled in the PSCAD/EMTDC environment for the time domain electromagnetic simulation. In such a system, the offshore terminal of VSC-HVDC is controlled to establish the reference voltage waveform in the offshore grid. The ac voltage controller in the offshore VSC-HVDC terminal has been improved by utilizing the measured active and reactive power-flows to determine the feed-forward terms for the current references in the dq -axes.

HVDC transmission decouples the offshore grid frequency from the onshore grid frequency. Three different methods have been evaluated here for relaying the onshore grid frequency to the offshore grid, such that the wind power plant can participate in the grid frequency control. One of the schemes does not involve communication, while the other two depend upon communication of onshore frequency signal. Similarly, three different methods have been evaluated and compared for the fault ride through behaviour of this system.

The current control capability of the converters in the offshore wind power plant grid can be utilized to enhance the fault time behaviour of the whole system. A novel approach has been proposed to allow a calculated amount of negative sequence current injection from the VSC-HVDC converters as well as the full scale converters in the wind turbine generators. The proposed approach is demonstrated to have lower power oscillations, and hence, lower dc voltage overshoots in the VSC-HVDC system.

On the protection side, the coordination of over-current relays has been analysed in the new environment. A simple yet reliable scheme utilizing the well-known over-current relay characteristics has been presented for the detection of faults and the determination of faulted feeder in the offshore grid. It is demonstrated that the communication capability of modern relays can help avoid the potential cases of over-reach.

The test system is modelled for real time simulation in RSCAD/RTDS platform, such that the physical relays could be connected to it. The performance of the proposed relay coordination scheme has been tested using an industrial relay. Moreover, since RTDS simulation allows continuous simulation of the system in real time, multiple events can be simulated. Simulation studies have been carried out for the fault detection, circuit breaker tripping, and system recovery after fault clearance.

Acknowledgments

My deepest gratitude goes to my supervisors Prof. Remus Teodorescu and Prof. Pedro Rodriguez for their valuable guidance, inspiration, support, and continuous encouragement. I would like to thank Dr. Philip C. Kjær, Peter W. Christensen and K. H. Sørbrink from Vestas A/S for their valuable discussions and constructive feedbacks during different stages of my research. I would also like to thank the Technical Reference Committee members, especially Dr. T. Jonsson, Prof. W L. Kling and Prof. M. Aredes.

This research is a part of Vestas Power Program. I would acknowledge Vestas Wind Systems A/S and Aalborg University for supporting my research.

I am grateful to Dr. A. M. Gole and Dr. U. Annakkage for the motivating discussions during my stay at University of Manitoba. I am thankful to Udana Gnanarathna, Dr. R. Gokaraju and Dr. Amit Jindal.

I would like to thank Dr. Dharshana Muthumuni, HVDC Research Center, who introduced me the world of PSCAD/EMTDC. I am thankful to Mr. In Kwon Park and Mr. Gregory Jackson from RTDS Technologies for teaching me the fundamentals of real time simulation. Jonas Hansen, ABB Denmark, was very helpful in setting up the relay interface with the RTDS systems.

I express my sincere gratitude to all the colleagues from the Vestas Power Program and the Department of Energy Technology as a whole for their friendship and support in various forms.

Lastly I would like to thank my parents, my sister, my wife, and my sons for their support and encouragement.

Sanjay K Chaudhary
Aalborg, Denmark,
September 2011

Contents

| | |
|--|------------|
| Abstract | i |
| Acknowledgments..... | iii |
| Abbreviations..... | 9 |
| 1 Introduction | 11 |
| 1.1 Background | 11 |
| 1.2 Wind Power Plants | 13 |
| 1.3 State-of-the-Art | 13 |
| 1.4 Motivation and Objectives | 17 |
| 1.4.1 Simulation Tools and Techniques | 18 |
| 1.5 Limitations | 18 |
| 1.6 Thesis Outline | 19 |
| 2 Grid Connection of Wind Power | 21 |
| 2.1 Wind Turbine Generator (WTG)..... | 21 |
| 2.1.1 Wind Turbine Characteristics..... | 21 |
| 2.1.2 Mechanical Control of Wind Turbines..... | 23 |
| 2.2 Wind Turbine Generators..... | 24 |
| 2.2.1 Type A: Fixed Speed..... | 24 |
| 2.2.2 Type B: Limited Variable Speed..... | 24 |
| 2.2.3 Type C: Variable Speed with Partial Scale Frequency Converter | 25 |
| 2.2.4 Type D: Variable Speed with Full Scale Frequency Converter..... | 25 |
| 2.2.5 Permanent Magnet Synchronous Generator (PMSG)..... | 25 |
| 2.3 Wind Turbine Generators with Full Scale Converters | 26 |
| 2.3.1 Permanent Magnet Generator with Machine (Generator) Side Converter (PMSG-MSC)..... | 27 |
| 2.4 Grid Connection of Wind Power Plants | 27 |
| 2.4.1 VSC-based HVDC Transmission | 30 |
| 2.5 Modular Multilevel Converter (MMC) based HVDC..... | 31 |
| 2.6 Summary | 34 |
| 3 System Layout and Main Circuit Parameters | 35 |
| 3.1 Main Circuit Components and Parameters..... | 35 |

| | | |
|--------|---|----|
| 3.2 | Onshore Grid..... | 36 |
| 3.3 | Converter Transformers | 36 |
| 3.4 | Voltage Source Converters | 36 |
| 3.5 | Tuned Filters | 37 |
| 3.6 | Phase Reactors | 40 |
| 3.7 | DC Line Capacitors..... | 41 |
| 3.8 | HVDC Cable..... | 41 |
| 3.9 | Wind Power Plant Layout | 41 |
| 3.10 | Neutral Grounding | 43 |
| 3.11 | Wind Turbine Generator with Full Scale Converter | 44 |
| 3.12 | Control of the Grid Side Converter of WTG-FSC | 46 |
| 3.13 | Separation of Positive and Negative Sequence Components | 47 |
| 3.14 | Positive Sequence Phase Locked Loop (PLL) | 50 |
| 3.15 | Control of VSC-HVDC system..... | 51 |
| 3.15.1 | Onshore Grid Converter..... | 51 |
| 3.15.2 | Offshore Grid Converter..... | 53 |
| 3.16 | Overall Control Structure | 55 |
| 3.17 | Summary | 57 |

4 Operation and Control of WPP with VSC-HVDC Connection 59

| | | |
|-------|--|----|
| 4.1 | Operational Modes | 59 |
| 4.1.1 | Charging of VSC-HVDC Lines | 59 |
| 4.1.2 | Energizing the Offshore Grid..... | 60 |
| 4.1.3 | Synchronization of the WTGs and Power Control | 61 |
| 4.1.4 | Steady State Operation..... | 63 |
| 4.1.5 | WPP Shut Down | 64 |
| 4.2 | Frequency Control through VSC-HVDC Transmission | 64 |
| 4.2.1 | German Grid Requirement on Frequency Regulation | 64 |
| 4.2.2 | Danish Grid Requirement on Frequency Regulation | 65 |
| 4.2.3 | Frequency Regulation through VSC-HVDC Transmission | 66 |
| 4.3 | Fault Ride Through Using VSC-HVDC Transmission..... | 70 |
| 4.3.1 | E.ON Grid Code for Fault Ride Through..... | 71 |
| 4.3.2 | Chopper Resistor for Fault Ride Through..... | 72 |
| 4.3.3 | FRT Using Fast Communication | 73 |
| 4.3.4 | FRT Using Frequency Increase and Voltage Reduction | 75 |
| 4.4 | Discussion | 76 |
| 4.5 | Summary | 77 |

| | | |
|----------|--|------------|
| 5 | Protection System for Offshore WPP Grid with VSC-HVDC Connection..... | 79 |
| 5.1 | Introduction | 79 |
| 5.2 | Overcurrent Relay | 80 |
| 5.3 | Approximate Calculation for the Fault Currents | 82 |
| 5.4 | Simulation Studies and Observations..... | 85 |
| 5.4.1 | Single Line to Ground Fault on a MV Feeder | 85 |
| 5.4.2 | Triple Line to Ground Fault on a MV Feeder | 87 |
| 5.4.3 | SLG and LLLG Faults on a HV Feeder | 89 |
| 5.4.4 | Relay Tripping for Different Types of Faults..... | 89 |
| 5.4.5 | Over-reach of the HV Feeder Relay..... | 92 |
| 5.5 | Discussion and Conclusions | 93 |
| 5.6 | Summary | 94 |
| 6 | Negative Sequence Current Controllers..... | 95 |
| 6.1 | Introduction | 95 |
| 6.2 | Negative Sequence Controller for the VSC-HVDC..... | 96 |
| 6.3 | Negative Sequence Controller for the WTG-GSC | 99 |
| 6.4 | Simulation Results..... | 101 |
| 6.4.1 | Single Line to Ground Fault at 'FA' | 102 |
| 6.4.2 | LLG, LLLG and LL Faults at 'FA' | 108 |
| 6.4.3 | Faults at <i>FB</i> | 110 |
| 6.5 | Discussion | 113 |
| 6.6 | Summary | 116 |
| 7 | RTDS Simulation of the Relay Coordination in the Offshore Grid | 117 |
| 7.1 | Introduction | 117 |
| 7.2 | Experimental Set-up..... | 118 |
| 7.2.1 | WTG with FSC Model..... | 119 |
| 7.2.2 | VSC HVDC Controllers..... | 119 |
| 7.2.3 | Over-current Limit Control in VSC | 120 |
| 7.2.4 | Over-current Protection Functions of the Relay..... | 120 |
| 7.2.5 | Over-current Relay Settings..... | 121 |
| 7.3 | GOOSE Communication Set-up | 122 |
| 7.4 | Simulation and Results..... | 122 |
| 7.4.1 | Steady State RTDS Simulation: | 122 |
| 7.4.2 | Comparison with PSCAD Simulation Results | 124 |

| | | |
|-------|--|-----|
| 7.4.3 | Single Line to Ground Fault on an MV Feeder..... | 126 |
| 7.4.4 | Double Line to Ground (LLG) Fault on an MV Feeder..... | 130 |
| 7.4.5 | Triple Line to Ground (LLLG) Fault on an MV Feeder..... | 132 |
| 7.4.6 | SLG Fault on a HV Feeder | 133 |
| 7.4.7 | Overcurrent Relay Trip Times for the Different Faults..... | 135 |
| 7.5 | Summary | 136 |

8 Conclusions and Future Work..... 137

| | | |
|-------|----------------------------------|-----|
| 8.1 | Conclusions..... | 137 |
| 8.2 | Main Contributions | 138 |
| 8.3 | Future Work | 139 |
| 8.4 | Author's Publication List | 139 |
| 8.4.1 | Paper Published..... | 139 |
| 8.4.2 | Co-authored Publications | 140 |
| 8.4.3 | Poster Publication | 141 |
| 8.4.4 | Paper Submitted to Journals..... | 141 |

References..... 143

Appendix A - Main Circuit Parameters..... 151

Appendix B - Phase Transformations and Sequence Components 157

Appendix C - Design of a PI Controller for the VSC-HVDC Controllers.... 162

Abbreviations

| | |
|-------|--|
| C2L | Cascaded Two Level (converter) |
| CB | Circuit Breaker |
| DFIG | Doubly Fed Induction Generator |
| FRT | Fault Ride Through |
| FSC | Full Scale Converter |
| GCR | Grid Code Requirements |
| GOOSE | Generic Object Oriented Sub-station Event (IEC 61850) |
| GSE | Generic Sub-station Event |
| GTNET | Gigabit Transceiver Network Card (RTDS Hardware) |
| GTAO | Gigabit Transceiver Analogue Output Card (RTDS Hardware) |
| HAWT | Horizontal Axis Wind Turbine |
| HVAC | High Voltage Alternating Current |
| HVDC | High Voltage Direct Current |
| IED | Intelligent Electronic Device |
| IGBT | Insulated Gate Bipolar Junction Transistor |
| IGCT | Insulated gate Commutated Thyristor |
| LVRT | Low Voltage Fault Ride Through |
| MMC | Modular Multilevel Converter |
| NSSC | Negative Sequence Current Controller |
| PLL | Phase Locked Loop |
| PMSM | Permanent Magnet Synchronous Motor |
| PMSG | Permanent Magnet Synchronous Generator |
| PWM | Pulse Width Modulation |
| RTDS® | Real Time Digital Simulator |
| SOGI | Second Order Generalized Integrator |
| VSC | Voltage Source Converter |
| WECS | Wind Energy Conversion System |
| WPP | Wind Power Plant |
| WTG | Wind Turbine Generator |

1 Introduction

1.1 Background

Wind energy is the fastest growing source of renewable energy—globally the average annual growth rate of installed wind power capacity has been around 30% in the last decade. The 2009 EU Renewable Energy Directive aims to produce 20% of the overall energy mix from renewable energy sources by 2020. In order to achieve this, EWEA has set a target to develop 230 GW of wind power; out of which 40 GW will come from offshore wind power plants [1]. In 2010, the global installed wind power capacity increased by 24.1% and reached 197 GW, out of which 86 GW was in Europe. Though a vast majority of these are onshore wind turbines, the offshore wind power plants are growing at even faster rate. In 2010, 883 MW of offshore wind power was added, bringing the total installed offshore wind power capacity to 2946 MW in Europe [2].

Figure 1.1 shows the growth of both onshore and offshore wind power plants from 1990 and it is projected till 2030. By 2030, the total installed wind power capacity will be 400 GW, out of which 150 GW will be offshore wind power installations. However, due to better capacity factor, the offshore wind power will be contributing around approximately half of the total wind energy production, as shown in Figure 1.2. By the year 2050, it is projected that there will be 350 GW onshore and 250 GW offshore wind power installation. Thereby, it will be able to meet 50% of the electricity demand in the European Union [1].

The last decade has seen a tremendous development in electricity generation from wind farms, also known as Wind Power Plants (WPP). In Europe, development of several large off-shore wind power plants has been proposed in the North Sea and the Baltic Sea. Such offshore wind farm sites may be up to 100-200 km far from the shore line; so as to take advantage of a better wind profile, and to avoid any clash of interest like shipping, fishery, recreation, and visual distraction.

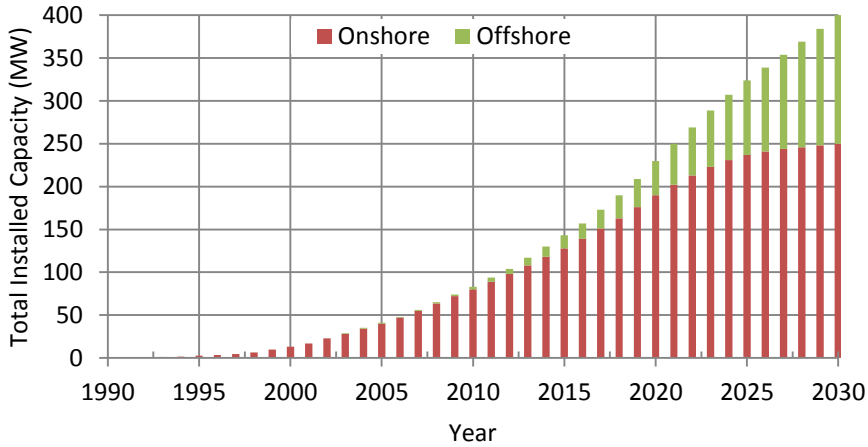


Figure 1.1 Total installed wind power capacity in the EU, projected till 2030 [1].

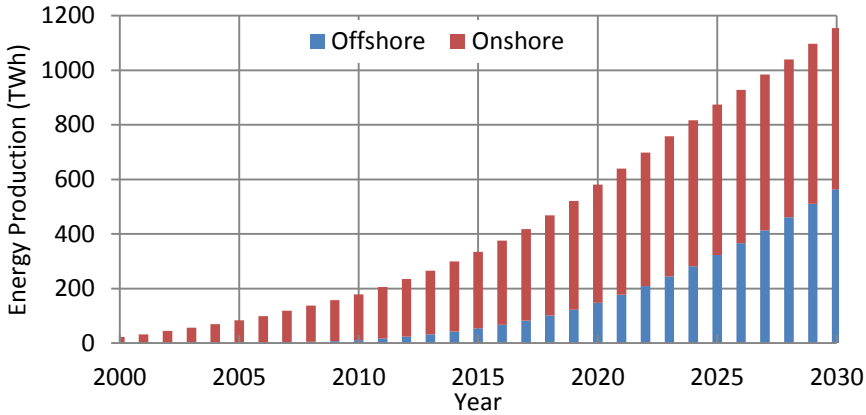


Figure 1.2. Wind power energy production in the EU, projected till 2030 [1].

Voltage source converter (VSC) based HVDC (VSC-HVDC) is the latest transmission technology for connecting distant offshore WPP which need long distance cable connection. Apart from providing an asynchronous link between the offshore WPP grid and the onshore power system grid, VSC-HVDC offers full and independent control of both the active power and the reactive power. VSC-HVDC transmission is, thus, expected to enhance the integration of the WPP in the power system grid. On the other hand, the Wind turbine generators, themselves, are using power electronic converters, thereby increasing their own controllability and flexibility.

1.2 Wind Power Plants

Unlike conventional power plants, a WPP does not have a deterministic and controllable prime mover. Wind is a stochastically varying and uncontrollable source of power for the WPP. Power can be generated only when sufficient wind is available. In absence of any energy storage system, the generated energy has to be distributed and consumed at the same time. Another disadvantage is that mechanical dimensions restrict the size of a wind turbine generator (WTG) to a few MW capacities. Therefore, a large number of WTGs have to be installed and interconnected to build a single offshore WPP. To ensure smooth operation of power system when large amount of wind power is connected, grid operators have imposed grid code requirements for the WPP to comply with.

Power electronic converters are employed in the WTGs to provide them the required flexibility and controllability; either by allowing them to align with the grid frequency as is the case in doubly fed induction generators; or by decoupling them from the grid frequency such as in the case of WTG's with full scale converters. On the transmission side, VSC-HVDC system provides an asynchronous link with independently controllable active and reactive power. Amid such a wide degree of controllability obtained from the power electronic converters and the variable nature of WTG, their control and co-ordination for efficient operation is very important.

1.3 State-of-the-Art

Wind power plants comprise of a large number of wind turbine generators (WTG), each having a unit size of a few MW at the most. In the early 1990s, the wind turbines mostly employed fixed speed squirrel cage induction generators. These were followed by the induction generators with limited range of speed control provided by the introduction of rotor resistance through slip rings. Nowadays doubly fed induction generators are the most popular ones. Recently permanent magnet synchronous generators (PMSG) with full scale converters are gaining popularity for large WTG units.

Grid connection of a large wind power plant is necessary for the transmission and distribution of the generated electric energy. Bresesti et al. [3] present a comparison of ac and dc transmission options for the grid connection

of offshore wind power plants. It is concluded that VSC-HVDC is the cheapest option for the grid connection when the plant size is larger than 100 MW and the distance is longer than 90 km. VSC-HVDC is the latest technology in HVDC transmission. The first commercial VSC-HVDC transmission was installed in Gotland, Sweden in the year 1997. Since then ABB has installed around 12 VSC-HVDC transmission systems. Most of them are for interconnecting weak grids. A couple of them provide electrical power transmission to offshore oil rig platforms in Norway. BorWin-I is the first VSC-HVDC transmission used for the grid connection of a large offshore WPP. It connects the 400 MW BorWin-1 wind farms in the North Sea to the onshore substation in Germany [4], [5].

VSC-HVDC systems use fully controllable switches like IGBT and IGCT. Their turning 'ON' and turning 'OFF' is controlled by the applied gate pulse. These switches are usually assembled in a 3-phase, 2-level or 3-level converter configuration. In VSC based HVDC, the IGBT switches are switched 'ON' and 'OFF' usually at a switching frequency of 1 to 2 kHz. The HVDC side voltage is maintained higher than the grid side peak voltages. Hence, the VSC can produce the desired voltage waveform at fundamental frequency. The output voltage contains high frequency components, which can be filtered away using passive filters. VSC can be controlled to produce the terminal voltage of required magnitude and phase angle such that the desired current can flow through the phase reactors at its terminals. This ability of the VSC to drive the desired current waveform in the grid at power frequency enables fast control and four-quadrant operation on the active-reactive power (PQ) plane [6].

Harnefors describes the control loops for the VSC HVDC transmission connecting two areas in the power grid in [7]. One terminal regulates the dc voltage and the reactive power exchange with the grid at one end, while the other regulates the active and reactive power exchanges at the other end. In [8], Iov *et al* present the control structure of the VSC-HVDC for the grid connection of wind farms with active stall induction generators. The wind farm side converter controls the wind farm grid voltage and frequency so as to enable variable frequency operation of the wind farm while maintaining the volts per Hertz ratio. The grid side VSC controls the dc line voltage and the reactive power flow to the grid. Direct control of the wind farm side voltage and its frequency without any inner current control loop is presented in [9]. In ref [10], an inner current control loop of the VSC controller is used to control

the ac terminal voltage in the offshore grid. This controller is suitable for wind power plant applications. Variable frequency control is described so as to take advantage of the improved efficiency of the WPP. In all these studies, DFIG based wind turbines have been considered.

With the emergence of large wind power plants, the grid operators are concerned about their impact upon the power system. Therefore, the grid operators have come up with the Grid Code Requirements (GCR) to be complied with before the wind power plants can be connected to the grid. The GCR specifies the operational conditions of voltage, frequency, and power factor. In the beginning, the wind power penetration in the power system was small, and they could disconnect during the grid disturbances. However, with increasing penetration of the wind power in the power system and decreasing proportion of the conventional synchronous generators, the grid operators demand that the large wind power plants remain connected to the grid and assist in its recovery. For instance, the German grid code [11] requires that the WPP remain connected and supply the reactive current to the grid during low voltage faults in the power system grid. It also specifies the power ramping rate during the system recovery after the fault has been cleared. Although it asks for $\pm 2\%$ reserve to be made available within 30 seconds for ± 200 mHz change in frequency, the offshore grid code [12] over-rides this requirement by asking for only downward regulation. In the Danish grid code [13], both options have been specified.

Low voltage ride through (LVRT) capability is another challenging requirement for the WPP. Reference [14] describes the different techniques available for fast power reduction of the wind power plant or dissipating the excess power in braking resistors. Feltes *et al.* [15] describe the different ways of achieving the LVRT capability and proposes the demagnetization of the doubly fed induction generator such that the WPP grid voltage can be suppressed rapidly. Thus, fast voltage reduction can be achieved without producing the typical short circuit currents; and the related electro- mechanical stresses can be avoided.

Muyeen *et al.* [16] have described the use of energy capacitor system (ECS) composed of power electronic devices and electric double layer capacitor (EDLC) to enhance the LVRT capability of fixed speed wind turbine generator system during network disturbances. Use of ECS using EDLC to

enhance the transient stability of multi-machine power system including WPPs is presented in [17].

In power systems, the synchronous machines provide the inertial response to sudden variations in frequency due to instantaneous load-generation unbalance. The wind turbine generators with their power electronic converter interface do not automatically respond to grid frequency variations. Therefore, there is a genuine concern that increasing penetration of wind energy in the power system will lead to reduction of inertia. Hence emulation of inertia or virtual inertia is expected from the wind turbine generators. Spanish Grid code has indicated the requirement of inertial response to grid frequency disturbances as a future perspective [18].

Reference [19] describes that the kinetic energy can be extracted from the WTGs using power electronic converter controls to supply the active power proportional to the frequency deviation, and thus inertia can be emulated. In [20], Ullah *et al.* describes that a wind farm can provide a short-term active power support utilizing the rotational energy of the turbine blades which is particularly beneficial in a hydro-dominated power system grid. The contribution from the wind turbines gives extra time for the hydro generators to ramp up their generation. Reference [21] presents the primary frequency regulation capability by maintaining the reserve power generation capability through their de-loaded operation by pitch angle control of wind turbines.

Jensen and Fuchs [22] describe the methods of allocation the generation reserve as well as the different ways to relay the grid frequency to the offshore wind-farm when there is an asynchronous VSC-HVDC connection between them.

Recently, Marquardt has invented the multi-level modular converters [23]. The cascaded two level converters (C2L) from the ABB, multi-level modular converters (MMC) from Siemens, and the hybrid chain link converters from Alstom are the examples of the new converter topologies for application in the VSC-HVDC transmission [24]–[26]. These new topologies of VSC-HVDC claim superior performance in terms of reduced power losses and lower harmonic content.

1.4 Motivation and Objectives

Technical literature and statistics of the wind power growth shows the enthusiasm in the development and grid connection of wind power plants. However, there are very little publications in the field of the faults and transients in the offshore grid, which does not have any directly connected synchronous machinery. There are converters at all the terminals. Their control and the network topology will determine the response to faults. There is a need for investigating the system response to the faults in the offshore grid. This project intends to investigate such faults in the offshore wind power plants connected by VSC-HVDC.

The main objective is to demonstrate control and operation of wind power plant (WPP) with voltage source converter based high voltage DC (HVDC) transmission showing robustness against offshore grid faults using the co-ordinated control of power converters in the wind turbine generators and the HVDC.

The hypotheses are listed below:

- Large wind turbine generators will be equipped with full scale converters to comply with the grid code requirements. Offshore wind power plants far off from the shore may require long submarine cable transmission. When VSC-HVDC transmission is used for the grid connection, the offshore grid may have power electronic converters at all the terminals.
- The output current of the power electronic converters can be controlled. In the event of faults, the fault current can be controlled within safe limits by the current limit control acting in the converters. This will reduce the stresses on the converters as well as other offshore grid components.
- As an extension of the previous point, negative sequence currents may be injected by the power electronic converters. Controllers can, therefore, be designed to control the negative sequence currents during asymmetric faults in the offshore grid, and thus minimize the power oscillations.

- Since a persistent fault in the offshore grid is detrimental to the operation of the whole WPP, a protection scheme would be necessary for its detection and isolation. Further since there are converters at all the terminals, and the offshore grid has mostly radial topology, use of the over-current relays might be possible.

1.4.1 Simulation Tools and Techniques

PSCAD/EMTDC software developed by the HVDC Research Centre, Canada, has been used for the modelling and simulation of the test system. It is a powerful simulation tool for the detailed modelling and time domain simulation of electromagnetic transients in power system. Apart from the standardized models for most of the power system components and control blocks, it allows the users to define the new models of the controllers and components. The controllers for the VSC-HVDC and the wind turbine generators are not available as standard modules, and they have been modelled here so that their detailed control structures could be simulated.

Real Time Digital Simulation (RTDS) has been used as it facilitates the hardware in loop simulation. An industrial overcurrent feeder protection relay, REF615 from ABB, was interfaced with the real time simulation model of the test system. Thus, the relay coordination was experimentally verified as a part of validation exercise.

MATLAB/Simulink has been used for other numerical calculations and frequency domain analysis of the controller and filters.

1.5 Limitations

Two-level converters have been simulated and studied. Recent development of multi-level converters has rendered the two-level converters an obsolete technology for future VSC-HVDC transmission projects. However, it is expected that the concepts and theories developed in this thesis regarding the offshore wind power plants and its grid connection using VSC-HVDC transmission would give useful insights in the understanding and investigation of the new systems.

Only ac collector grid layout has been considered here for the wind power plant. The turbine generators are assumed to be permanent magnet synchronous generators equipped with full scale converters. Moreover, a simplified model has been used for the wind turbine generator and its full scale converter instead of the detailed model. The turbine, generator, and the generator side converter are collectively modelled as a power source with a first order transfer function. The focus here is on the operational behaviour of the grid side converter of the WTG-FSC, the collector grid network and the VSC-HVDC transmission to the grid.

The onshore grid has been modelled here as Thévenin's equivalent voltage source.

WPP and VSC-HVDC have been considered here as a single system. This implies that the VSC-HVDC control is used to facilitate the grid integration of the wind power plant. The onshore grid terminal is assumed to be the point of common coupling where the grid code requirements have to be fulfilled. These assumptions are justified when the WPP and VSC-HVDC are owned and operated by a single entity. When the transmission is provided by the grid operator, the grid operator may impose the grid code requirements to be fulfilled at the offshore terminal as envisaged in [12], or they may continue to operate in tandem to optimize the overall system.

1.6 Thesis Outline

The organization of the thesis is as follows:

Chapter 2 gives a brief introduction of wind turbine generators and the grid connection of wind power plants using VSC-HVDC.

Chapter 3 describes the layout and modelling of the test system being studied. Main circuit parameters for the system components have been derived and discussed. A collector grid layout and the aggregation of wind turbines have been described here. An improved controller for the offshore VSC-HVDC terminal is presented for the wind power applications followed by the overall control structure of the system.

The operation and control of the complete integrated system is described in Chapter 4. Some operational aspects, like the grid frequency control through VSC-HVDC, and the low voltage fault ride through in the event of onshore grid faults, have been described and demonstrated.

Chapter 5 proposes a simplified algorithm for the estimation of fault currents using the scalar current source models of the WTG converters. Transient simulation of faults in the offshore grid using detailed models of the WTG controls and VSC-HVDC is described and the results are compared. The results are used for the coordination of the over-current relays in the offshore grid. The work is later extended in Chapter 7.

Chapter 6 proposes a negative sequence current control algorithm for the control of dc power oscillations, and therefore, the dc voltage oscillation in the VSC-HVDC system. The controller performance is tested using transient simulations in PSCAD/EMTDC.

Chapter 7 describes the hardware in loop simulation of the test system with an industrial over-current relay. Different fault cases have been simulated. The performance of the relay coordination in terms of the detection of fault events and subsequent tripping has been presented. It corroborates the observation for the relay coordination settings.

Finally, chapter 8 summarizes the conclusions of this project and lists some of the areas for future research.

2 Grid Connection of Wind Power

Moving mass of wind possesses kinetic energy. For a long time wind mills and sails have been used for harnessing the wind energy. Nevertheless, conversion to electrical energy is a recent development of the twentieth century. Depleting fossil fuel reserves and the focus on sustainable development through the use of renewable energy sources have been the key motivators for the rapid development of wind energy conversion systems (WECS) in the last couple of decades. Large wind turbine generators of the order of 2–6 MW have been developed and the units of 10 MW sizes are under development [27].

Tens or hundreds of wind turbine generator units are installed and connected together through a network of medium voltage cable systems forming the collector system network, thereby forming a large wind farm. A growing penetration of wind energy into power system demands that the wind farms behave more like a power plant, and they comply with the rules of grid connection, or the grid code requirement (GCR). Hence, these days the wind farms are referred to as wind power plants (WPP).

This chapter presents an introduction of WECS, collector system and the grid connection of WPP.

2.1 Wind Turbine Generator (WTG)

A wind turbine generator comprises of a wind turbine for harnessing the kinetic energy of the wind into the mechanical energy of the rotating shaft which drives the generator. The three-blade, upwind horizontal axis wind turbine (HAWT) is the most popular turbine. It has three air-foils or blades connected to a central hub assembly mounted on the top of a high tower. The drive train, generator and the transformers are usually housed in the nacelle on the tower. A gear box assembly may be used to rotate the generator at a sufficiently high speed for electrical power generation.

2.1.1 Wind Turbine Characteristics

The kinetic energy possessed in wind is given by

$$K.E_{wind} = \frac{1}{2} \rho V v_w^2 \quad (2.1)$$

where, ρ is the density of air ($kg.m^{-3}$), V is the volume of air considered and v_w is the velocity of wind ($m.s^{-1}$).

The volume of wind passing through area A_R swept by the turbine blades in a second is, $V = A_R v_w$. Therefore, the total mechanical power is,

$$P_{wind} = \frac{1}{2} \rho A_R v_w^3 = \frac{1}{2} \rho \pi R_t^2 v_w^3 \quad (2.2)$$

It is impossible to extract all the kinetic energy from the wind. The fraction of power harnessed by the wind turbine is given by its coefficient of performance, C_p .

$$P_{turb} = C_p P_{wind} = \frac{1}{2} C_p \rho \pi R_t^2 v_w^3 \quad (2.3)$$

According to Betz, the theoretical upper limit of C_p is $C_p = \frac{16}{27} = 0.593$. Modern 3-blade wind turbines have an optimal C_p in the range of 0.52 to 0.55 when the power is measured at the rotor hub. After deducting the losses in the drive train and the generator, the optimal value of C_p lies in the range of 0.46 to 0.48 [28]. The value of C_p depends upon the tip speed ratio, λ and the pitch angle of the blade, β and the turbine characteristics. Tip speed ratio is defined as the ratio of rotor blade tip speed and the wind velocity.

$$\text{Tip Speed Ratio } (\lambda) = \frac{\text{Rotor tip speed}}{\text{wind velocity}} = \frac{\omega_t \cdot R_t}{V_w} \quad (2.4)$$

For a given turbine design, the measured data for $C_p(\lambda, \beta)$ can be approximated by a non-linear function of the type [29],

$$C_p(\lambda, \beta) = c_1(c_2 - c_3\beta - c_4\beta^{c_5} - c_6)e^{-\frac{c_7}{\lambda_i}}, \quad (2.5)$$

where, $\lambda_i = \left(\frac{1}{\lambda + c_8\beta} - \frac{c_9}{\beta^3 + 1} \right)^{-1}$

Slootweg *et al.* have presented a table of coefficients for the commercial constant speed and variable speed wind turbines in [29]. The turbine characteristic for the performance coefficient $C_p(\lambda, \beta)$, given in [30], is a special case of (2.5),

$$C_p(\lambda, \beta) = 0.5 \cdot \left(\frac{116}{\lambda_i} - 0.4\beta - 5 \right) e^{-\frac{18.5}{\lambda_i}} \quad (2.6)$$

$$\text{where, } \lambda_i = \frac{1}{\frac{1}{\lambda + 0.08\beta} - \frac{0.035}{\beta^3 + 1}}.$$

Figure 2.1 gives a plot of C_p - λ characteristics using (2.6) with parameters as given in (2.6).

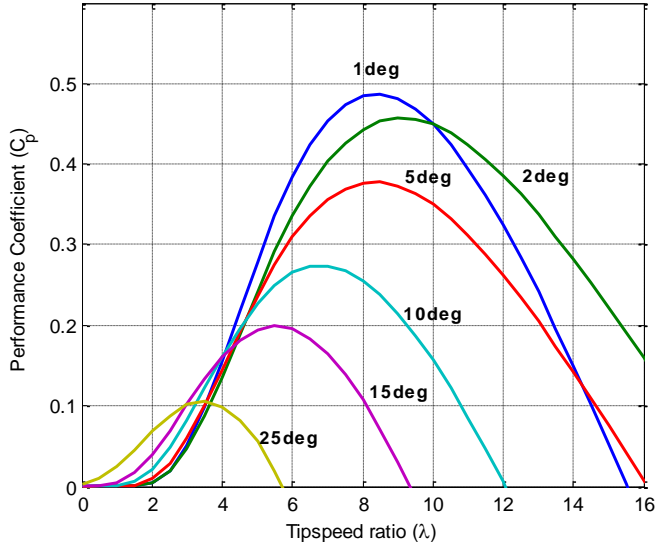


Figure 2.1. C_p - λ characteristics of a typical wind turbine.

2.1.2 Mechanical Control of Wind Turbines

Equations (2.2)–(2.7) reveal that the power absorbed by the wind turbines depends upon the operational speed of the turbine and the blade pitch angle. In a variable speed wind turbine, the turbine speed can be controlled to achieve an optimal tip speed ratio (λ), and therefore maximum efficiency can be achieved over a range of wind speed. When the wind speed varies, the turbine rotor and generator speed vary, while the torque remains fairly constant. Thus, the

mechanical stress is reduced. Maximum power point tracking over a wide speed range enables increased energy capture, improved power quality, and reduced mechanical stress on the wind turbine. Apart from this, the turbine speed should be limited within safe design limits in presence of strong wind conditions. Stall control has been used for fixed speed wind turbines. Fast pitch control mechanism is used to regulate the power in variable speed wind turbines [28]. The blades can be turned out or into the wind as the power output varies. Such a fast control provides good power control, assisted start-up and emergency stop.

2.2 Wind Turbine Generators

Wind turbine generators can be grouped into four categories [28]:

- Type A: Fixed speed
- Type B: Limited variable speed
- Type C: Variable speed with partial scale frequency converter.
- Type D: Variable speed with full scale frequency converter.

2.2.1 Type A: Fixed Speed

Fixed speed wind turbines comprise of squirrel cage induction generator (SCIG) or wound rotor induction generator directly connected to the grid through a step-up transformer. Usually, a soft-starter is used to provide the smooth start-up, and a capacitor bank provides the reactive power compensation. Fixed speed operation implies that any wind fluctuation would result into the fluctuation of the mechanical torque and the electrical power. While the mechanical torque fluctuations cause high mechanical stress, the electrical power fluctuations lead to voltage fluctuation and flicker effects in the case of weak grids. Such wind turbines use stall control, pitch control, or active stall control [28].

2.2.2 Type B: Limited Variable Speed

Variable speed operation over a small range of around 0-10% can be achieved by using wound rotor induction generator with variable rotor resistance connected to the rotor winding through slip rings [30]. The

mechanical power control is achieved by pitch control. Excess energy is dissipated into the rotor resistance.

2.2.3 Type C: Variable Speed with Partial Scale Frequency Converter

A doubly fed induction generator (DFIG) with partial scale converters allows speed control in a range of $\pm 30\%$ around the synchronous speed. The sizes of the converters are approximately 30% of the nominal generator power [31]. The partial scale converter injects voltage in the rotor circuit at the slip frequency to vary the slip, and thus, the variable speed operation is achieved.

2.2.4 Type D: Variable Speed with Full Scale Frequency Converter

The generator is connected to the grid through a back-to-back converter system with a common dc-link. This converter is rated to the full power of the converter and hence it is also known as full scale converter (FSC). Since the generator is decoupled from the grid frequency, synchronous generators as well as induction generators can be used. However, an induction generator usually have a fewer number of pole pairs. Operation of the wind turbine at the normal speed of 20–22 rpm will need a gear ratio of 68 for a four pole machine. On the other hand, synchronous machines can be designed with multiple pole pairs thereby reducing the synchronous speed. Multi-pole structure and frequency decoupling enables these to be operated at very low speeds, and hence, the gear-box can be avoided. Such a drive system is referred to as direct drive. Annular generators from Enercon are of this type. However, the diameter of the machine tends to be very large for large power ratings and low speed operations. Therefore, a single stage gear-box is used, as in the case of ‘Multi-brid’ [31].

2.2.5 Permanent Magnet Synchronous Generator (PMSG)

Synchronous generators are widely used in power generation system. The mechanical speed (ω_m) of a P -pole synchronous machine operating at the frequency, f is given by

$$\omega_m = \frac{120f}{P} \text{ rpm} \quad (2.7)$$

This implies that a multi-pole synchronous machine can be operated at very low mechanical speeds. In a direct drive synchronous generator, the multiple number of poles brings down the synchronous mechanical speed to the nominal speed of the rotor, and hence, there is no need of a gear-box. However, the machine diameters tend to be very big to accommodate a large number of poles. In the Multi-brid concept, a single stage gear-box is used to bring down the size and weight of the generator. Direct drive permanent magnet synchronous generators (PMSG) have 35% lower losses than the DFIG and approximately 32% lower than that of the direct drive synchronous generators with wound rotors. If a single stage gear-box is used, the losses increase, but there is a 75% reduction in weight as the synchronous speed is higher [27].

2.3 Wind Turbine Generators with Full Scale Converters

Variable speed wind turbines may have a wound rotor synchronous generator, permanent magnet synchronous generator or an induction generator. In all the cases, the generator dynamics is controlled by the machine side converter for the optimum or specified power generation. A schematic of wind turbine, gear-box (which is absent in direct-drive topology), PMSG, FSC, L-C-L filter and the unit transformer is shown in Figure 2.2. In this section, the wind model, aerodynamics, shaft model, and permanent magnet synchronous generator with the controlling converter are briefly described.

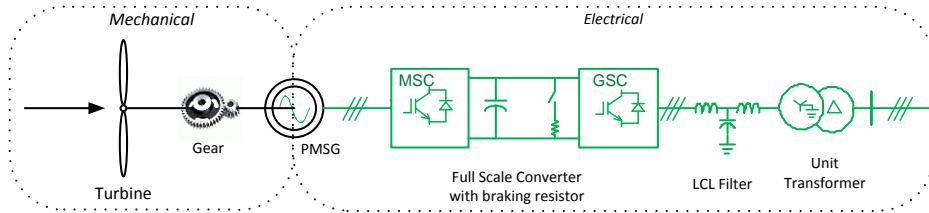


Figure 2.2 Wind Turbine, PMSG, FSC, L-C-L output filter and unit transformer.

Mechanical power available in the wind and the power that can be harnessed depend upon the wind velocity and the operating point of the wind turbine (2.3). For simulation studies, a model of wind can be represented by a sum of average, ramp, gust and noise components as given by,

$$V_w = V_{wb} + V_{wg} + V_{wr} + V_{wn} \quad (2.8)$$

where, $V_w, V_{wb}, V_{wg}, V_{wr}, V_{wn}$ are the average (base), gust, ramp and noise components of the wind speed in m/s [29], [32]. The wind turbine generator shaft dynamics can be modeled in terms of a set of three coupled masses representing the blade, the hub, and the generator. Slootweg *et al.* [29] recommends using two mass representation of the drive train to include the dynamics of the low speed shaft.

2.3.1 Permanent Magnet Generator with Machine (Generator) Side Converter (PMSG-MSC)

Permanent magnet synchronous generator (PMSG) is a synchronous machine, where the field flux is generated by the permanent magnets instead of the field excitation winding. Strachan and Jovicic [33], [34] describe modelling and control of PMSG and the machine side converter in the synchronously rotating reference frame. The generator torque can be precisely controlled by vector control of the stator currents. The direct axis current is controlled to zero value such that the torque becomes proportional to the quadrature-axis current. It is used to drive the machine and hence the turbine at optimal speed. The machine side converter provides the required voltage at the machine terminals so as to achieve the stator current control.

As described in next chapter, the wind turbine, drive train, the generator, and the generator side converter are not modelled in detail, but they are collectively modelled as a power source with first order transfer function.

2.4 Grid Connection of Wind Power Plants

Large wind power plants can be connected to the high voltage power system grid through high voltage ac (HVAC) or high voltage dc (HVDC) connection. Most of the operational wind farms are close to the shore and hence they are connected using HVAC connection. For instance, Horns Rev Wind farm uses 21 km of submarine cable and 36 km of onshore cable for the HVAC transmission of 160 MW at 150 kV [35].

Recently some large wind power plants are being developed in the North Sea, far from the coast. They need long distance cable transmission for grid connection. A high voltage submarine cable has a large shunt capacitance given by [36],

$$C = \frac{2\pi\epsilon_0\epsilon_r}{\ln\left(\frac{D_{eq}}{r}\right)} F/m \quad (2.9)$$

where, C is the cable capacitance, $\epsilon_0\epsilon_r$ is the permittivity of the cable insulation, D_{eq} is the geometric mean distance between the conductor cores, and r is the radius of the conductor core.

Long distance HVAC cable transmission suffers from the excessive reactive current drawn by the cable capacitance. The var generation by submarine cables depends upon the rated voltage and length of the cable. Typically, it is 100–150 kvar/km for 33 kV cross-linked polyethylene (XLPE) cables, 1 Mvar/km for 132 kV XLPE cables, and 6–8 Mvar/km for 400 kV XLPE cables [3]. Such a large amount of var generation increases the cable losses, reduces the power transfer capability, and requires reactive shunt compensation to absorb the excessive reactive power; and thereby avoid over-voltage. Presently ac cables have a maximum cable rating of about 200 MW for a 200-km long three-phase cable, at a voltage level of 150–170 kV. It will require inductive compensation at both ends to absorb the var generated. For a shorter distance of 100 km, voltage ratings may be raised to 245 kV, thereby increasing the power transfer capability to 350 MW [37]. Thus, HVAC transmission is not feasible for large offshore power plants requiring cable transmission over long distances. After a detailed techno-economical evaluation, Bresesti *et al.* concluded in [3] that VSC-HVDC is the cheapest option for connecting a 100 MW (and larger) wind power plants at distances longer than 90 km from the shore.

At present several large VSC-HVDC projects like BorWin-I and II, DolWin-I, HelWin-I are under development for the connection of offshore wind power plants in the North Sea [38] as shown in Figure 2.3. Unlike HVAC transmission systems, there is no reactive power generation or absorption in HVDC transmission systems. Hence, HVDC transmission is very suitable for bulk power transmission over long distances. This has been one of the driving factors for the development of HVDC systems since the first commercial installation in Gotland in the year 1954.



Figure 2.4. Offshore wind power plants with VSC-HVDC connection (Source: TenneT TSO GmbH).

The advantages of HVDC systems are fast and reversible power flow, asynchronous and decoupled connection of two grids, power flow control and power oscillation damping capabilities. Though a large number of large line commutated converter (LCC) based HVDC systems are operational for bulk power transmission and/or asynchronous connection between two grids, none of them is associated with wind farms.

LCC-based HVDC terminals use thyristor-bridge converters, which require a stable ac voltage for commutation. These converters are operated by delaying the phase of current ideally between 0° and 180° with respect to the associated voltage waveform. Hence, the current is always lagging behind the voltage. Such converters always absorb reactive power [36]. The reactive power (var) requirement for the LCC terminals is of the order of 60% of the active power rating; though actual reactive power absorption depends upon the power flow level. Large capacitive filters are used to filter out the low frequency harmonics, and simultaneously provide reactive power to the terminals. Another problem lies in the fact that LCC-based HVDC cannot be connected to weak ac grids due to the risk of commutation failures and voltage instability. The strength of ac grid with respect to the LCC-based HVDC rating is measured in terms of short circuit ratio (SCR), and effective short circuit ratio (ESCR), which accounts for the reactive power compensation provided at the terminals [36].

2.4.1 VSC-based HVDC Transmission

High voltage, high power two-level or three-level voltage source converters (VSC) are used in HVDC applications. It is possible to switch the insulated gate bipolar transistor (IGBT) switches in the VSC at a frequency of a few kHz for pulse width modulation to control the phase of the current with respect to the voltage waveform. Both active and reactive power exchange can be independently controlled. This enables the four quadrant operation of the converter as shown in Figure 2.5.

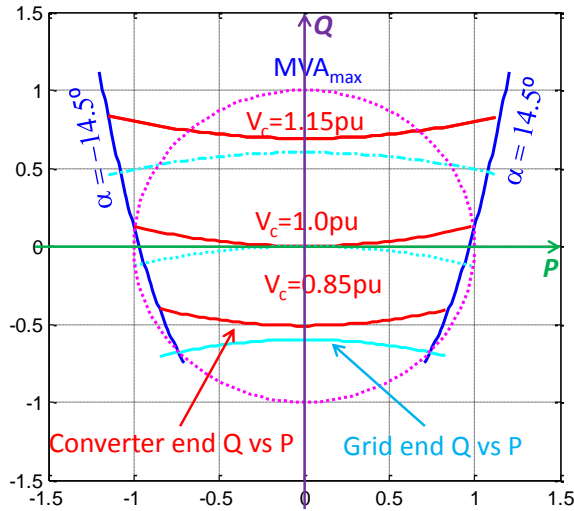


Figure 2.5. Four quadrant operational capability of a VSC.

The advantages of VSC-HVDC over the LCC-HVDC are listed below [39]:

- I. VSC-HVDC occupies around 4-6 times less footprint area as it does not require additional reactive power compensation, and passive harmonic filters tuned at high frequencies can be used. In the case of LCC, the filters are bulky as they are tuned at relatively lower frequencies of 11th and 13th harmonic and they have to provide reactive power compensation to the HVDC converters. Moreover, multiple numbers of such filters are used, such that they can be switched as per the load levels.

- II. VSC-HVDC allows continuous control of reactive power independent of the active power flow. LCC-HVDC has a limited and discrete control over reactive power flow, as the capacitive banks have to be switched 'ON' or 'OFF' for reactive power control. Therefore, VSC-HVDC can support voltage regulation like a STATCOM while the LCC-HVDC has a limited voltage regulation control.
- III. VSC-HVDC can provide fault ride-through and black start capabilities.
- IV. VSC-HVDC can be connected to weak ac grids as well as passive grids. LCC-HVDC requires a strong ac grid with a minimum short circuit ratio of 2.0.
- V. Power reversal in LCC-HVDC involves current interruption as the voltage polarity has to be reversed. In case of VSC-HVDC, no such interruption is encountered as the current direction is reversed for power reversal.
- VI. LCC-HVDC operates on current source converter topology. Hence, at least 5-10% of dc power flow is required for their operation. There is no such constraint on VSC-HVDC.
- VII. VSC-HVDC allows power reversal by the reversal of current direction. Therefore, it is more amenable to multi-terminal operation in comparison to LCC-HVDC, where the current direction cannot be changed.

Due to these advantages VSC-HVDC is suitable for the grid connection of the offshore wind power plants to the onshore grids. BorWin-I HVDC is the first HVDC connection to an offshore wind farm. It connects the 400-MW Borkum-2 wind farms to the German Grid. The wind turbine generators, of 5-MW unit size, are connected to a 33-kV collector grid. The voltage is first stepped up to 170 kV ac voltage and then the offshore HVDC converter converts it to ± 150 kV dc voltage. The transmission link comprises of 128 km of submarine cable and 75 km of underground cable before connecting to the 380 kV ac grid at Diele.

2.5 Modular Multilevel Converter (MMC) based HVDC

Recently modular multi-level converters (MMC) have been developed for HVDC applications [41], [42]. The MMC comprises of a large number of half-

bridge converters, usually referred to as sub-modules, with isolated capacitors in cascade connection. Such a multi-level configuration provides modularity, scalability, and the ac output voltage has very low harmonic content [23]. The switching frequency can be reduced, and hence, the switching losses get reduced as well. Due to these benefits, the new topology has rendered the two-level or three-level VSC topologies obsolete for the new VSC-HVDC installations. After the first VSC-HVDC connection to the Borkum-2 wind power plant, which is now known as BorWin-I, all the new VSC-HVDCs, *viz.* BorWin-II, HelWin-I, DolWin-I, SylWin-I, connecting the wind farms in the North Sea are of the MMC-HVDC type (Figure 2.4).

A multi-level converter comprises of a number of unit sub-modules of a low unit voltage ratings connected in series to attain the required high voltage level as shown in Figure 2.6. Each sub-module comprises of a pair of complimentary IGBT switches connected in series across the sub-module capacitor. When the switch T_1 is *ON*, the capacitor voltage, the sub-module is referred to as turned *ON*, and the voltage V_c appears across the sub-module terminals. In the *ON* state of the sub-module, its capacitor gets charged or discharged depending upon the direction of its current, I_{sm} . When the switch T_2 is turned *ON*, and the switch T_1 is *OFF*, the sub-module capacitor is by-passed and the sub-module output voltage is 0. Thus by controlling the complimentary switches T_1 and T_2 , the output voltage of a sub-module can be controlled. Since, there are a large number of sub-module units connected in series; a multi-level output ac voltage waveform can be generated by controlling the *ON* or *OFF* state of the sub-modules between the ac voltage terminal and the dc pole. At any instant, the ac terminal voltage for phase-A is given by,

$$\begin{aligned} V_a &= \frac{V_{dc}}{2} - n_{up}V_c + L_c \frac{d}{dt} i_{a,up} \\ V_a &= -\frac{V_{dc}}{2} + n_{lo}V_c + L_c \frac{d}{dt} i_{a,lo} \end{aligned} \quad (2.10)$$

where, n_{up} , n_{lo} are the number of sub-modules in *ON* state in the upper and lower multi-valves of the same phase. Similarly, other phase voltages can be obtained. From (2.10) it is obvious that when the voltage drop across the reactors are ignored, the total number of sub-modules in a phase is related to the dc pole voltage by the relation,

$$N_{np} = N_{nn} = \frac{V_{dc}}{V_c} = n_{up} + n_{lo} \quad (2.11)$$

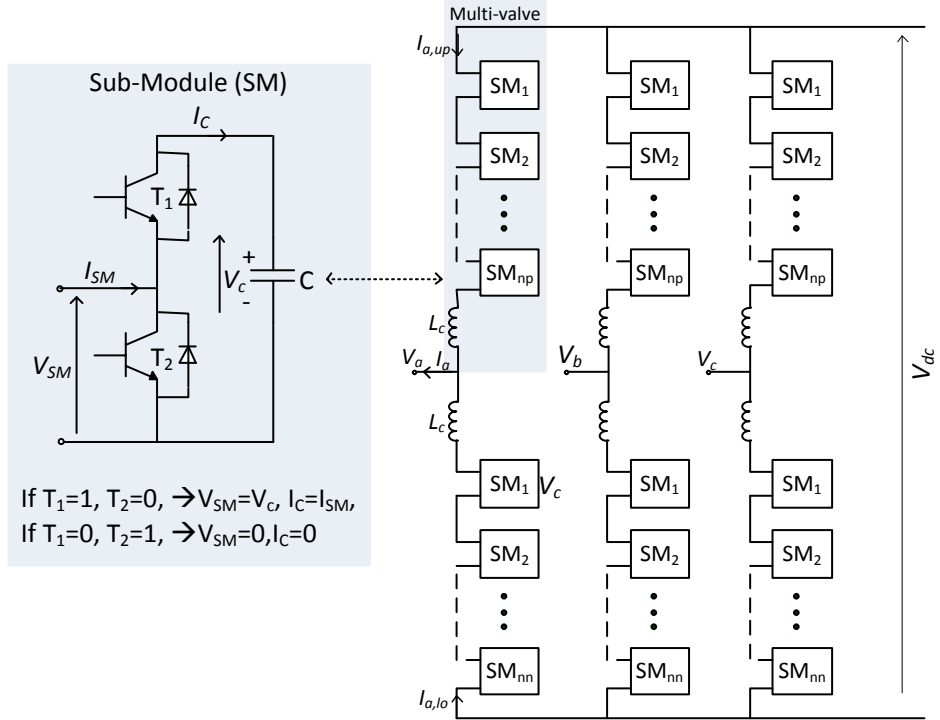


Figure 2.6. Modular multi-level voltage source converter.

Since the multi-level output ac voltage has a lower harmonic content, hence the tuned filters, which are mandatory in a two-level or three-level converters, are not required in an MMC. The converter sub-modules are switched at a low frequency, but the effective frequency turns out to be very high due to the large number of sub-modules connected in series. Due to low frequency switching, the overall losses are lower [43]. On the flip side, the number of IGBT switches required for a given converter is double of that required in a two-level converter.

The multi-level output ac voltage has a lower harmonic content and hence the tuned filters, which are mandatory in a two-level or three-level converters are not required. The converter sub-modules are switched at a low frequency, but the effective frequency turns out to be very high due to the number of sub-

modules connected in series. Due to low frequency switching, the overall losses are lower [43]. On the flip side, the number of IGBT switches required for a given converter is doubled.

An application of MMC-HVDC for the connection of wind power plants was presented in [41]. Nevertheless, the two-level VSC-HVDC system has been considered in this project. The project deals with the analysis of the operation and control of the WPP with VSC-HVDC connection to the grid with respect to the normal as well as the faulted conditions. Most of the findings of this project can be extended to the MMC-HVDC systems as well with necessary modifications.

2.6 Summary

Wind power plants have been briefly introduced in this chapter. VSC-HVDC transmission has several advantages over the high voltage ac transmission, especially for the grid integration of large and remote offshore wind power plants. Consequently, all such plants have been proposed to have the VSC-HVDC connection. MMC-HVDC is the latest development in VSC-HVDC transmission. However, this project does not involve the actual converter design, and the two-level VSC-HVDC will be used in this project.

3 System Layout and Main Circuit Parameters

A 400 MW offshore wind power plant with VSC-HVDC connection to the onshore grid was considered as the test system. A single line drawing is given in Figure 3.1. In this chapter, the different components of the system are described. Some of the main circuit parameters were assumed on the basis of system ratings, while others were determined.

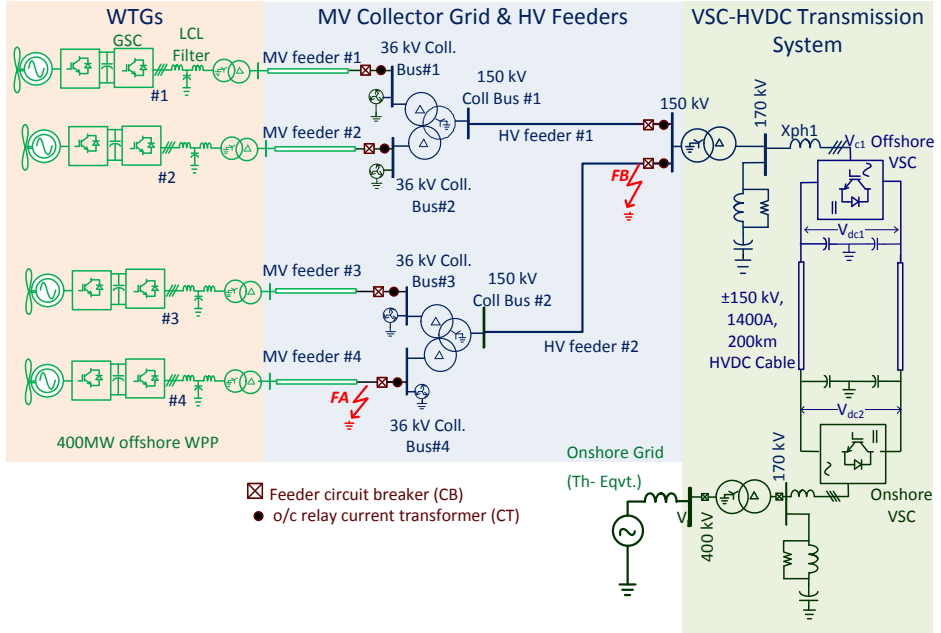


Figure 3.1. Single line diagram (SLD) of the test system (a 400 MW WPP with VSC-HVDC connection to the grid).

3.1 Main Circuit Components and Parameters

The test system comprises of the following main components:

- i. Onshore grid
- ii. Converter transformers
- iii. Tuned filters
- iv. Phase reactors
- v. Voltage source converters
- vi. HVDC capacitors
- vii. HVDC cables
- viii. 150-kV submarine cables

- ix. Three-winding transformers
- x. Zig-zag grounding transformers
- xi. Wind turbine generators with L-C-L filters

3.2 Onshore Grid

The onshore grid is represented by a Thevenin's equivalent of a 400-kV voltage source with series impedance. The grid impedance is estimated on the basis of the WPP short circuit ratio at the point of grid connection. The resistive and inductive parts of the impedance are determined from the grid angle. For simulating the plant behaviour, the Danish grid code specifies the ratio of wind power plant capacity to the grid short circuit MVA, which is also referred to as the short circuit ratio. It should be considered as 10, and the grid angle should be considered as 84.3° which means that the reactance to resistance ratio (X/R ratio) should be 10 [13].

3.3 Converter Transformers

Converter transformers are required to interface the VSC output voltage to the grid voltage. The onshore converter transformer has the nominal voltage ratio of 400/170-kV as it interfaces the 170-kV VSC with the 400-kV onshore grid. The offshore converter transformer has the nominal voltage ratio of 170/150 kV to connect with the offshore collector grid at 150 kV. The transformer is sized at 450 MVA in line with the system base of 445 MVA for 400-MW WPP. Tap changers are provided to bring down the grid side nominal voltage -15% in 12 steps of 1.25% . The leakage reactance is assumed to be 14% , and the losses are 0.5% no load loss and 0.5% full load copper loss.

3.4 Voltage Source Converters

Two-level voltage source converters have been considered here for the VSC-HVDC transmission system. Sine-triangle modulation at the 39^{th} harmonic (i.e. 1950 Hz for 50-Hz ac system) switching frequency has been assumed, which represents the first generation of the VSC-HVDC converter.

Sinusoidal pulse-width modulation (SPWM) of two level converters generates odd harmonics at the switching frequency and its multiples along

with the sidebands around them. The harmonic components in the output is given by the expression [44],

$$v_{an}(t) = \frac{V_{dc}}{2} M \cos(\omega_0 t + \theta_0) + \frac{2V_{dc}}{\pi} \sum_{m=1}^{\infty} \frac{1}{m} J_0\left(\frac{m\pi}{2} M\right) \sin\left(\frac{m\pi}{2}\right) \cos\{m(\omega_c t + \theta_c)\} \\ + \frac{2V_{dc}}{\pi} \sum_{m=1}^{\infty} \sum_{\substack{n=-\infty \\ n \neq 0}}^{\infty} \frac{1}{m} J_n\left(\frac{m\pi}{2} M\right) \sin\left(\frac{(m+n)\pi}{2}\right) \cos\{m(\omega_c t + \theta_c) + n(\omega_0 t + \theta_0)\} \quad (3.1)$$

where, $V_{an}(t)$ = instantaneous line to ground voltage,

V_{dc} = pole to pole dc voltage,

M = modulation index

ω_0, ω_c = fundamental and carrier frequencies

θ_0, θ_c = phase angles of the fundamental and the carrier frequency at time, $(t = 0)$.

$J_i(\beta)$ = i -th order Bessel function of the first kind with the argument, β .

The amplitudes of the harmonic components decrease with the reciprocal of the multiple number m of the switching frequency. Hence, the harmonics around the first and second multiples of the switching frequency (i.e. the 37th, 39th, 41st, 77th, and the 79th harmonics) have relatively higher amplitudes. A plot of the harmonic spectrum of a two-level converter is given in Figure 3.2.

The triplen harmonic voltage components constitute the zero sequence and hence they do not appear in the expression for the line-to-line voltage. The harmonic currents can, however flow at these frequencies, as the grounded filters provide the path for the zero sequence currents.

3.5 Tuned Filters

The high frequency harmonics generated by the PWM can be filtered by using passive tuned filters. Such a filter is usually characterized by the tuned resonant frequency, quality factor and shunt reactive power injected at the power frequency.

The admittance function of the filter shown in Figure 3.3 is given by (3.2).

$$Y_f(s) = \frac{s^2 LC + sCR}{s^2 LCR + sL + R} \quad (3.2)$$

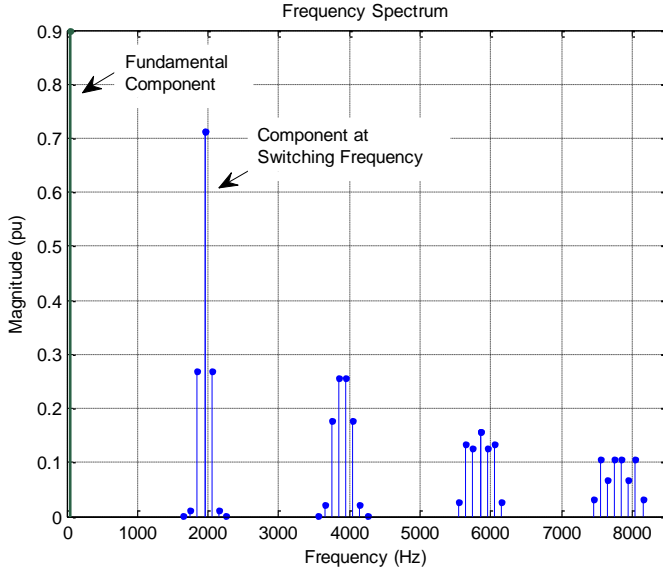


Figure 3.2 Frequency spectrum of a two level voltage source converter (Modulation index=0.9).

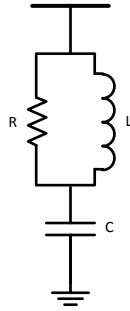


Figure 3.3. Tuned filter circuit.

Two such filters, tuned at the 39th and 78th harmonic frequencies, are used at each of the two VSC-HVDC terminals in this test system. They have the quality factors of 25 and 6 respectively, and they inject 0.06 pu and 0.03 pu of reactive power respectively. From these data, the resistance, inductance and capacitance are calculated as described in Appendix A. The admittance versus frequency characteristics of these filters are shown in Figure 3.4 and Figure 3.5.

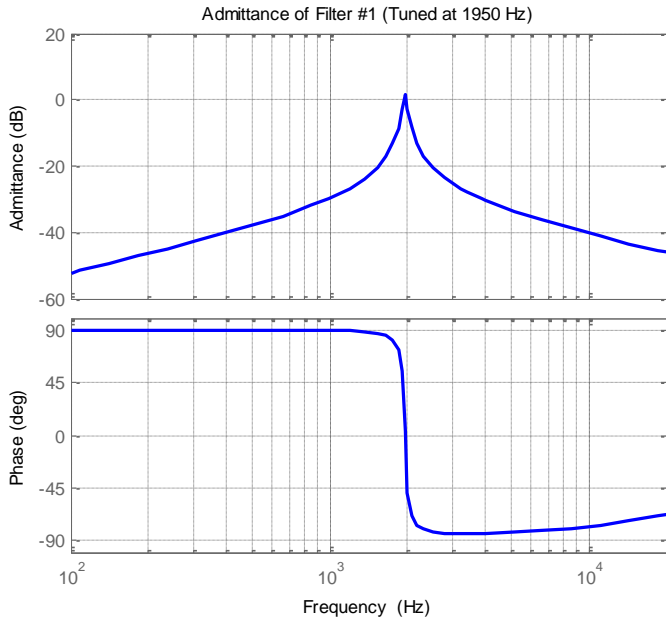


Figure 3.4. Bode plot of 39th harmonic filter admittance.

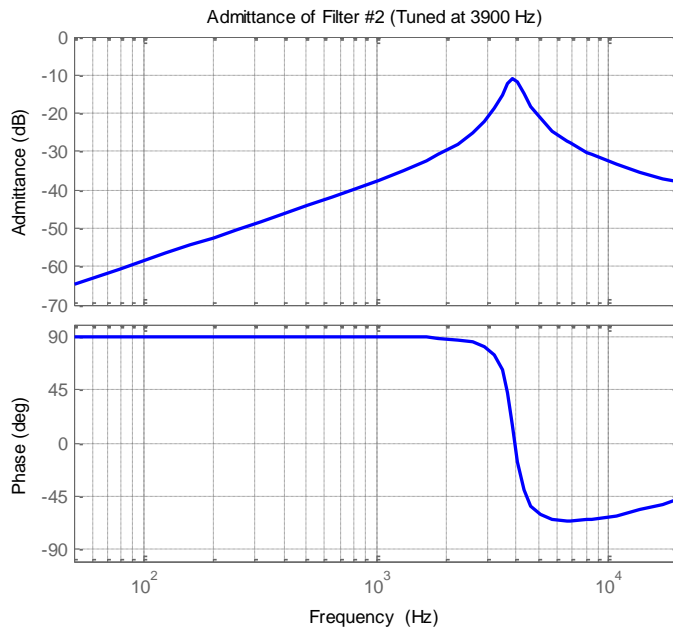


Figure 3.5 Bode plot of 78th harmonic filter admittance.

3.6 Phase Reactors

Phase reactors are required to interface the PWM converter with the grid. It provides the attenuation of current ripples, as the maximum peak-to-peak ripple current is given by,

$$i_{ripple} = \left(\frac{V_{dc}}{2L} \right) \left(\frac{1}{2f_{sw}} \right) \quad (3.3)$$

where, V_{dc} = pole to pole dc voltage, L = phase reactor inductance and f_{sw} = switching frequency.

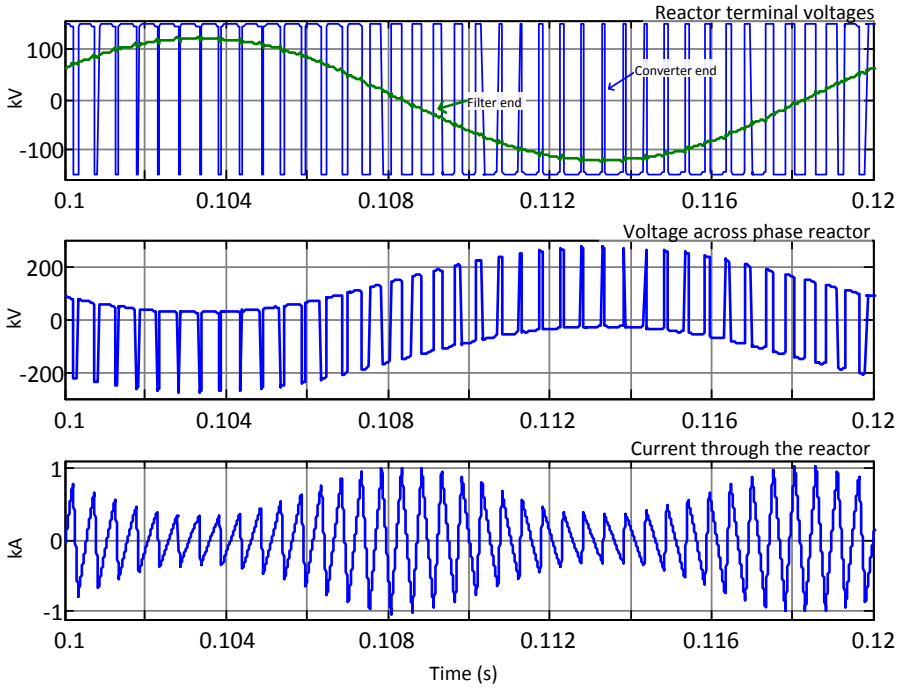


Figure 3.6. Phase reactor voltage and current waveforms

Figure 3.6 shows the ripple currents through a 19.3 mH phase reactor driven by a VSC with 300 kV dc link voltage at the switching frequency of 1950 Hz. A large phase reactor would mean a higher impedance to the ripple current, and hence, lower current ripples. However, too high value would slow down the dynamics of the converter. In this project a phase reactor of 0.12 pu size has been used.

3.7 DC Line Capacitors

DC line capacitors provide the filtering of current ripples on the dc side as well as maintain the dc voltage for the operation of the VSC. These are sized on the basis of the dc link voltage and power handling capacities of the converter [45]. Typically, the size is given in terms of time constant, τ defined as,

$$\tau = \frac{\text{Energy stored}}{\text{Nominal power rating}} = \frac{CV_{dc}^2}{2P_n} \quad (3.4)$$

In other words τ is the time taken to charge the capacitors to the nominal dc voltage level, when they are charged by the rated current. For the VSC-HVDC system in this project, a time constant of 2 ms has been used [45], [46]. This gives the capacitor size of 35.5 μF from each of the dc lines to the ground.

3.8 HVDC Cable

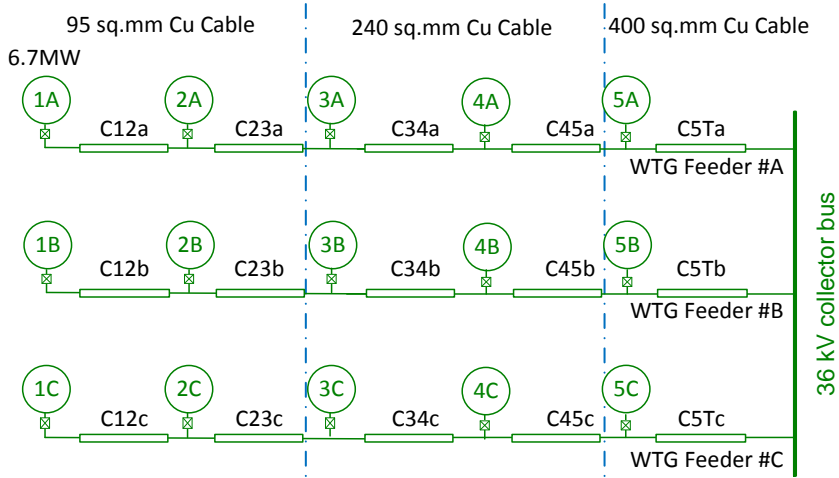
Cross-linked polyethylene (XLPE) cables are used in VSC-HVDC transmission. Nominal power rating of 400 MW at ± 150 kV dc voltage requires a current flow of 1.33 kA. Assuming a current density of 1.2 A/mm², the required copper cross section area is 1111 mm². In BorWin 1 HVDC of similar ratings, XLPE insulated copper cables of 1200 mm² conductor cross section were used. The calculations are given in Appendix A. An insulation thickness of 12 mm is assumed.

3.9 Wind Power Plant Layout

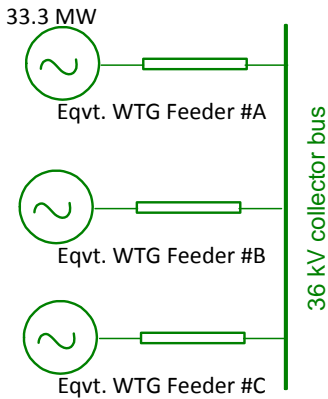
The 400-MW wind power plant is divided into four clusters. Each cluster has fifteen WTGs installed on three radial feeders as shown in Figure 3.7(a). There are five 6.7 MW turbines on each feeder, referred to as a string. Thus, the total capacity of feeder becomes 33.5MW. The IEEE Working Group Report [47] states that the underground feeder strings are generally rated for around 25 to 30 MW due to soil thermal conditions and practical cable sizes. Three WTG feeder strings are connected to the same collector bus in parallel combination.

Under rated power generation conditions, the radial feeder current will increase as the number of turbine connections increase along the cable length

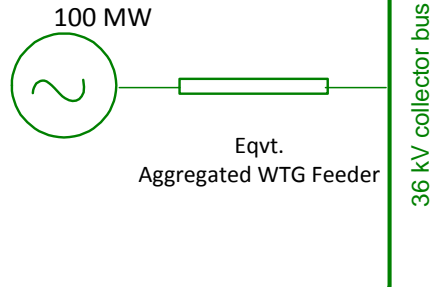
towards the collector bus. Hence, the cable cross-section near the collector bus should be larger than the cable cross-section at the remote end. Here three different cable cross sections, viz. 95 mm², 240 sq. mm², and 400 mm² have been used as shown in Figure 3.7(a).



(a) WTG layout in the test WPP layout



(b) Equivalent WTG cable strings



(c) Equivalent aggregated WTG cable feeder

Figure 3.7. Layout of a wind power plant and its aggregate model.

The equivalent parameters for the equivalent WTG feeder string #A in Figure 3.7(b) can be calculated on the basis of active and reactive power loss in the feeder for the rated current flow from each of the WTGs [48]. It is given by,

$$Z_{eq} = \frac{\sum_{m=1}^n m^2 Z_m}{n^2}, \quad B_{tot} = \sum_{m=1}^n B_m \quad (3.5)$$

where, Z_m is the series impedance and B_m is the shunt susceptance of the m^{th} section. Z_{eq} is the equivalent series impedance, and B_{tot} is the total shunt susceptance of the equivalent feeder.

Equation (3.5) is based upon the assumption that there are m WTGs connected to the cable section m , and each of them contribute the same nominal current to the cable. As the three feeder strings appear in parallel at the collector bus, the equivalent feeder impedance, $Z_{eq,fr}$ and susceptance, $B_{eq,fr}$ as shown in Figure 3.7(c) are given by their parallel combination [48]. These are given by,

$$Z_{eq,fr} = \frac{Z_{eq}}{3}, \quad B_{eq,fr} = 3B_{tot} \quad (3.6)$$

The WTG feeders are connected to the 36-kV terminals of the three-winding step-up transformer as shown in Figure 3.1. Such a connection is inspired from [49]. The collector grid voltage was selected as 36 kV, instead of the more popular 33-kV systems, in order to optimize the cable size for the adopted power ratings. The 150-kV terminals of the three-winding transformer are connected to the converter transformer through 150-kV high voltage (HV) cable feeders.

3.10 Neutral Grounding

The WTG end of the 36-kV medium voltage (MV) cable feeders are connected to the delta winding terminals of the unit transformer, which has the YnD_5 winding configuration. Even the other end of the MV feeder is connected to the delta winding terminals of the plant step-up transformer at the collector bus. Thus, both the ends of the MV feeders in the WPP collector grid are terminated to the delta winding terminals of the transformers, which pose high impedance to the flow of the zeros-sequence currents. Therefore, the MV feeders remain ungrounded. When there is a single line to ground fault, zero-sequence currents are produced which cannot flow in an ungrounded system. Consequently, the fault current is low but over-voltages of the order of 1.73 pu or even higher in the case of arcing faults are produced [50].

An ungrounded system or the system with high resistance grounding (HRG) system enables uninterrupted system operation even in the event of a single line to ground fault. Due to high impedance of the zero sequence network, the fault current is very small, and fault detection is difficult. The system need not be interrupted as such. However, it results in over-voltages on the healthy phases, and oscillating neutral conditions appears in the presence of unbalanced operations. Moreover, the overvoltage raises the probability of another fault, thereby, leading to a line-line fault. Therefore, HRG is not favoured for high voltage applications. HRG systems can be applied on 2.4-kV and 4.16-kV systems, though they are mostly used on power systems of voltages up to 600V ac [51].

The system grounding can be provided by the addition of a star-delta transformer with the grounded neutral and the delta winding terminals in open circuit, a zig-zag grounding transformer, or a T-connected grounding transformer. Zig-zag transformer is commonly employed as grounding transformer in power systems as it is less expensive, and relatively smaller in size [52].

Figure 3.8 shows the winding configuration of a zig-zag grounding transformer and its phasor diagram for the positive sequence components. Each of the three limbs has two sets of windings denoted by letters (A_1 , B_1 , or C_1) and (a_1, b_1 , or c_1). Series connection of the two windings of different phases ensures that they carry the same current; and since the two windings on the same limb are wound in opposite direction, the net flux due to the zero sequence current is zero. Therefore, it has low impedance for the zero sequence currents, which is effectively the leakage reactance of the transformer. At the same time, it offers very high impedance, which is effectively the magnetizing reactance of the transformer core, for the positive and negative sequence components [52].

3.11 Wind Turbine Generator with Full Scale Converter

The wind model, aerodynamics, gear system, the synchronous generator and the generator side converter are collectively modelled as a first order low-pass transfer function with an assumed time constant of 20 ms. Mechanical power from the wind is provided as an input to the transfer function. Its output

is an equivalent dc current source connected to the dc link of the full scale converter as shown in Figure 3.9.

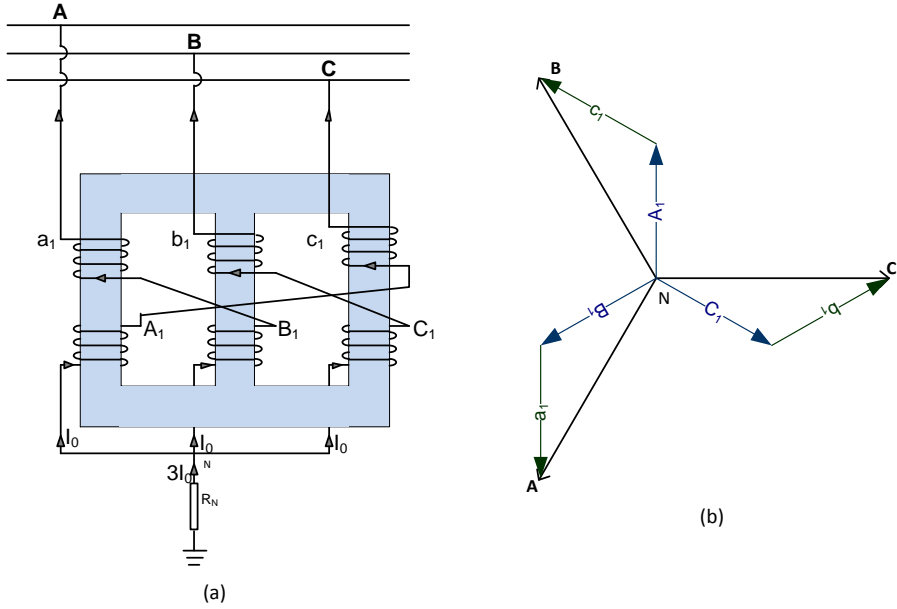


Figure 3.8. Neutral grounding zig-zag transformer. (a) Winding configuration; (b) Phasor diagram.

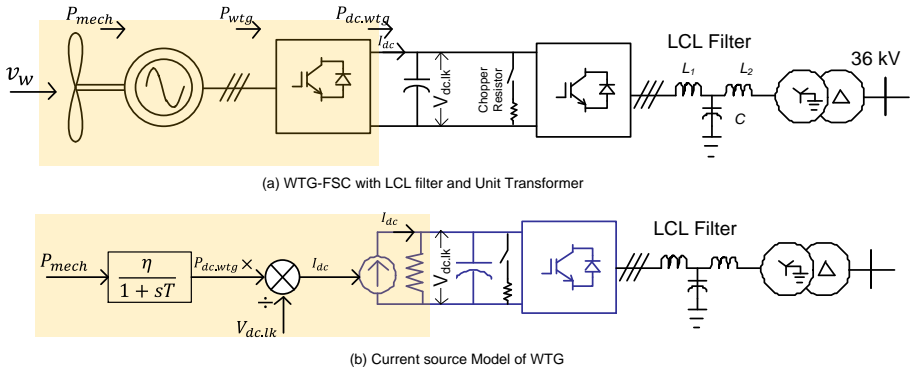


Figure 3.9 Model of an aggregated WTG with its LCL filter and step-up transformer.

The grid side converter (GSC) is controlled to maintain the dc link voltage balance by evacuating the excess power to the offshore grid. It is equipped with an L-C-L filter, and the unit transformer in grounded wye-delta connection. The grounded wye is on the low voltage (LV) side towards the GSC, and the delta connection is on the medium voltage (MV) side. Such a connection

isolates the zero sequence impedance of the MV grid from the individual WTG LV circuit and provides a solid ground reference for the WTG [47]. There is a load-break switch to disconnect the WTG when required.

3.12 Control of the Grid Side Converter of WTG-FSC

Positive sequence current control approach has been considered here for the grid side converter (GSC) of the WTG-FSC system. Accordingly, for a given transfer of active power, P_{av} and reactive power, Q_{av} the positive sequence current references of WTG-GSC are given by,

$$\left. \begin{aligned} i_{\alpha}^* &= \left(\frac{v_{\alpha p} P_{av} + v_{\beta p} Q_{av}}{v_{\alpha p}^2 + v_{\beta p}^2} \right) \\ i_{\beta}^* &= \left(\frac{-v_{\alpha p} Q_{av} + v_{\beta p} P_{av}}{v_{\alpha p}^2 + v_{\beta p}^2} \right) \end{aligned} \right\} \quad (3.7)$$

where, $v_{\alpha p}$ and $v_{\beta p}$ are the positive sequence voltage components across the capacitor of the LCL filter of the WTG. The terms, i_{α}^* and i_{β}^* are the positive sequence current references along the $\alpha\beta$ -axes in the stationary reference frame. Proportional resonant controllers are used to implement the current control, as shown in Figure 3.10.

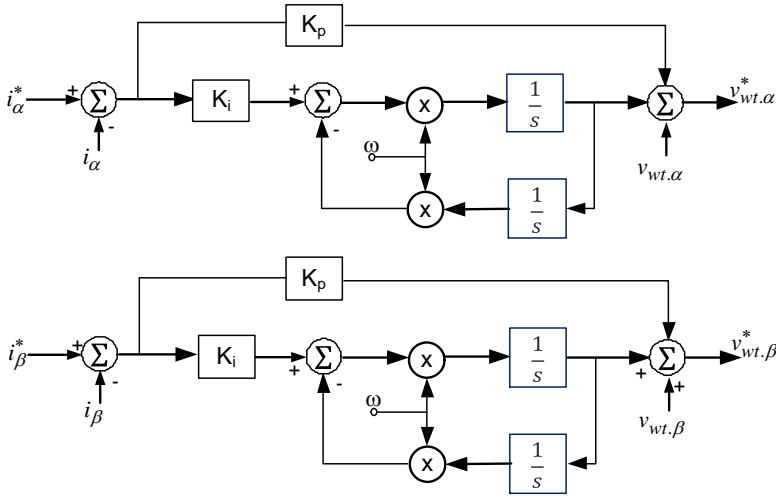


Figure 3.10. Proportional resonant current controllers for the WTG GSC.

The overall control structure along with the schematics of a WTG-GSC is shown in Figure 3.11. The current control equations are given below:

$$v_{wt,\alpha}^* = (i_{\alpha}^* - i_{\alpha}) \left(k_p + \frac{k_i \omega s}{s^2 + \omega^2} \right) + v_{wt,\alpha} \quad (3.8)$$

$$v_{wt,\beta}^* = (i_{\beta}^* - i_{\beta}) \left(k_p + \frac{k_i \omega s}{s^2 + \omega^2} \right) + v_{wt,\beta} \quad (3.9)$$

Equation (3.7) requires the estimation of the positive sequence components from the three phase measured voltage variables. The next section describes the extraction of the positive sequence components and the positive sequence component based phase locked loop (PLL).

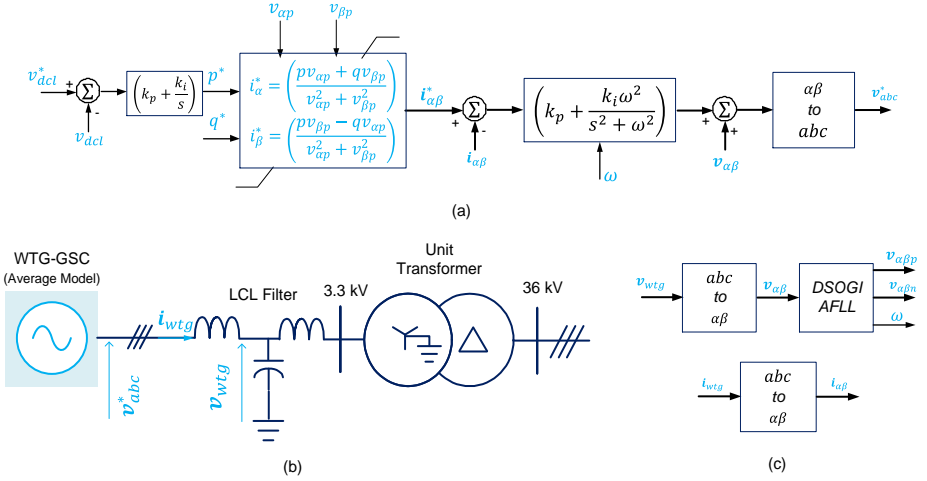


Figure 3.11. WTG GSC (a) controller, (b) schematics and (c) WTG current and voltage signal transformations.

3.13 Separation of Positive and Negative Sequence Components

The sequence components of a three-phase voltage or current can be obtained using Clarke's transformation and the second order generalized integrator (SOGI) based filters. The extraction of positive and negative sequence components is described here with respect to the three-phase voltage. The same process is applied to extract the sequence components of the current as well.

The measured three-phase voltage quantities can be converted into two-phase equivalent along the α - β axes using the Clarke's transformation as follows,

$$\begin{bmatrix} v_\alpha \\ v_\beta \end{bmatrix} = \frac{2}{3} \begin{bmatrix} 1 & -\frac{1}{2} & -\frac{1}{2} \\ 0 & \frac{\sqrt{3}}{2} & -\frac{\sqrt{3}}{2} \end{bmatrix} \begin{bmatrix} v_a \\ v_b \\ v_c \end{bmatrix} \quad (3.10)$$

The α -axis is aligned with the axis of phase A, while the β -axis leads the α -axis by 90° . For a set of balanced three-phase positive sequence voltages v_{ap} , v_{bp} , and v_{cp} ; the positive sequence components $v_{\alpha p}$ and $v_{\beta p}$ have the same magnitude as that of v_{ap} . The component $v_{\alpha p}$ is in phase with the phase A voltage v_{ap} , and $v_{\beta p}$ lags $v_{\alpha p}$ by 90° . Likewise, for a set of balanced three-phase negative sequence voltages, v_{an} , v_{bn} , and v_{cn} ; the negative sequence components $v_{\alpha n}$ and $v_{\beta n}$ have the same magnitude as that of v_{an} . The component $v_{\alpha n}$ is in phase with the phase A voltage v_{an} ; while the component $v_{\beta n}$ leads $v_{\alpha n}$ by 90° .

A set of unbalanced voltages can be decomposed into balanced positive, negative and zero sequence components. In absence of the zero-sequence components, the positive sequence components, $(v_{\alpha p}, v_{\beta p})$ and the negative sequence components $(v_{\alpha n}, v_{\beta n})$ in the α - β axes are given by the transformations [53],

$$\begin{bmatrix} v_{\alpha p} \\ v_{\beta p} \end{bmatrix} = \frac{1}{2} \begin{bmatrix} 1 & -q \\ q & 1 \end{bmatrix} \begin{bmatrix} v_\alpha \\ v_\beta \end{bmatrix} \quad (3.11)$$

$$\begin{bmatrix} v_{\alpha n} \\ v_{\beta n} \end{bmatrix} = \frac{1}{2} \begin{bmatrix} 1 & q \\ -q & 1 \end{bmatrix} \begin{bmatrix} v_\alpha \\ v_\beta \end{bmatrix} \quad (3.12)$$

Here, the multiplication of a vector by $= e^{-\frac{j\pi}{2}}$, introduces a phase lag of 90° without changing its magnitude. This implies that the phase shifted components of the components v_α and v_β are required. A derivation of these equations is given in Appendix B. It is obvious from (3.9) and (3.10) that,

$$\begin{bmatrix} v_\alpha \\ v_\beta \end{bmatrix} = \begin{bmatrix} v_{\alpha p} \\ v_{\beta p} \end{bmatrix} + \begin{bmatrix} v_{\alpha n} \\ v_{\beta n} \end{bmatrix} \quad (3.13)$$

In-phase and quadrature components of the input voltage signal are required in (3.11), (3.12). These are obtained using the second order generalized integrator (SOGI), which is tuned at the nominal power frequency. Hence, it is also referred to as SOGI quadrature signal generator (QSG). Figure 3.12 gives a block diagram of SOGI-QSGs for the voltage components along the α - β axes.

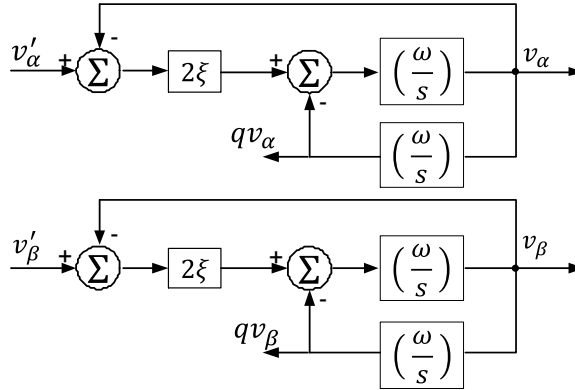


Figure 3.12. Block Diagram of SOGI quadrature signal generator (QSG)

By Mason's loop gain formula, the transfer functions of the SOGI-QSG for the in-phase component v_α along the α -axis, and its quadrature component, qv_α are given by,

$$\frac{v_\alpha(s)}{v'_\alpha(s)} = \frac{2\xi\omega s}{s^2 + 2\xi\omega s + \omega^2} \quad (3.14)$$

$$\frac{qv_\alpha(s)}{v'_\alpha(s)} = \frac{2\xi\omega^2}{s^2 + 2\xi\omega s + \omega^2} \quad (3.15)$$

At, the tuned frequency, ω , the gains are unity.

$$\left. \frac{v_\alpha(s)}{v'_\alpha(s)} \right|_{s=j\omega} = 1 \quad \text{and} \quad \left. \frac{qv_\alpha(s)}{v'_\alpha(s)} \right|_{s=j\omega} = -j \quad (3.16)$$

The parameter ' ξ ' determines the bandwidth. At the resonant frequency, the in-phase signal v_α is extracted from the input signal v'_α with unity gain; while the components at all other frequencies get attenuated as shown by curve #1 in Figure 3.16. A quadrature signal qv_α which lags the in-phase signal by 90° , is generated with unity gain at the resonant frequency as given by (3.16). Similar analysis is applicable for the components, v_β and qv_β .

Once the instantaneous voltage components along the $\alpha\beta$ -axes, and their 90° phase-shifted components are available, the positive and negative sequence components can be calculated using (3.11) and (3.12). The curve #3 represents the frequency response of the positive sequence component along the α -axis in Figure 3.13

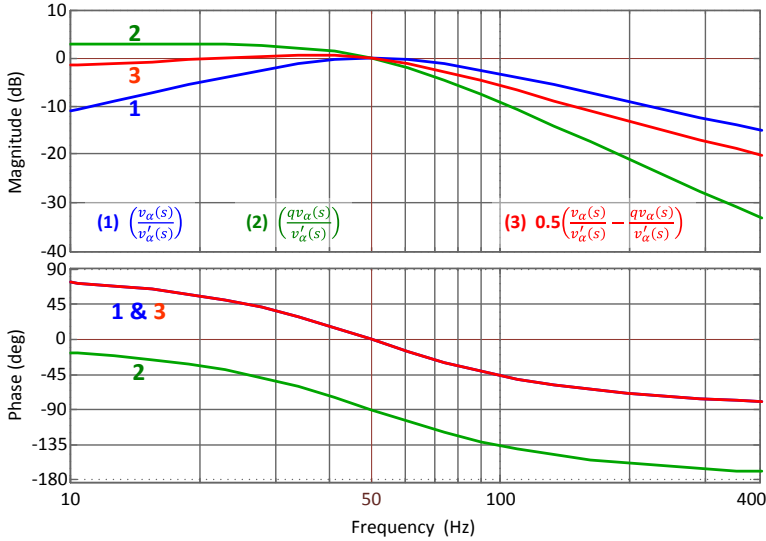


Figure 3.13. Bode plot of SOGI-QSG (Curve #3 is for the positive sequence components).

3.14 Positive Sequence Phase Locked Loop (PLL)

A positive sequence PLL has been developed using the positive sequence voltage components along the $\alpha\beta$ -axes. Since the voltage vector is aligned along the d -axis, the q -axis component is applied to the proportional integral (PI) controller to get the frequency (ω) and the phase angle (θ) as shown in Figure 3.14.

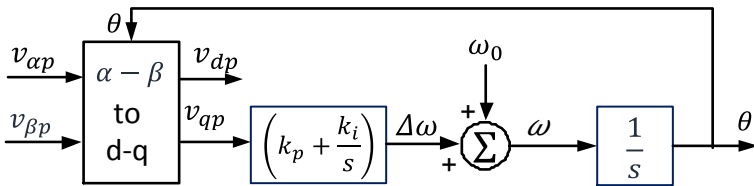


Figure 3.14. Positive sequence phase locked loop.

3.15 Control of VSC-HVDC system

The VSC-HVDC transmission system has two converters: the onshore converter, VSC#1, and the offshore converter, VSC#2. The basic control scheme of these converters is described here.

3.15.1 Onshore Grid Converter

The onshore VSC controller (VSCC#2) regulates the HVDC voltage and the reactive power (or ac terminal voltage) exchanged with the onshore grid. Its block diagram along with the terminal schematic is shown in Figure 3.15. Conventional vector control of currents in the dq - axes in the rotating reference frame has been applied here. The converter terminal voltage ($v_d + jv_q$) are related to the grid voltage ($u_d + ju_q$) at the filter bus by Kirchhoff's Voltage Law (KVL) in the rotating reference frame by,

$$v_d = u_d - i_d R_{pr} + \omega L_{pr} i_q - L_{pr} \frac{d}{dt} i_d \quad (3.17)$$

$$v_q = u_q - i_q R_{pr} - \omega L_{pr} i_d - L_{pr} \frac{d}{dt} i_q \quad (3.18)$$

where, ω is the frequency, R_{pr} and L_{pr} are the resistance and inductance of the phase reactor. The grid voltage ($u_d + ju_q$) is measured at the filter bus. It is shown by the vector symbol, $\mathbf{v}_f = (u_d + ju_q)$ in Figure 3.15(b). The phase reactor current ($i_d + ji_q$) flows into the converter, as shown by the three phase symbol, \mathbf{i}_{abc} .

The proportional-integral (PI) controller acts upon the current deviation from the reference current signals ($i_d^* + ji_q^*$) to produce the voltage references for the converter ($v_d^* + jv_q^*$) as given below,

$$v_d^* = u_d - i_d R_{pr} + \omega L_{pr} i_q - k_{p1}(i_d^* - i_d) - k_{i1} \int (i_d^* - i_d) \quad (3.19)$$

$$v_q^* = u_q - i_q R_{pr} - \omega L_{pr} i_d - k_{p1}(i_q^* - i_q) - k_{i1} \int (i_q^* - i_q) \quad (3.20)$$

The outer loops regulate the dc line voltage, V_{dc} of the VSC-HVDC transmission on the onshore terminals and the reactive power flow, Q_{ac} to the grid. Since the PLL is aligned such that the grid voltage appears along the d -axis in the synchronous rotating reference frame, the reference for d -axis current control will regulate the active power flow, and hence, the dc voltage. Similarly, the q -axis current control will control the reactive power exchange with the grid as given by,

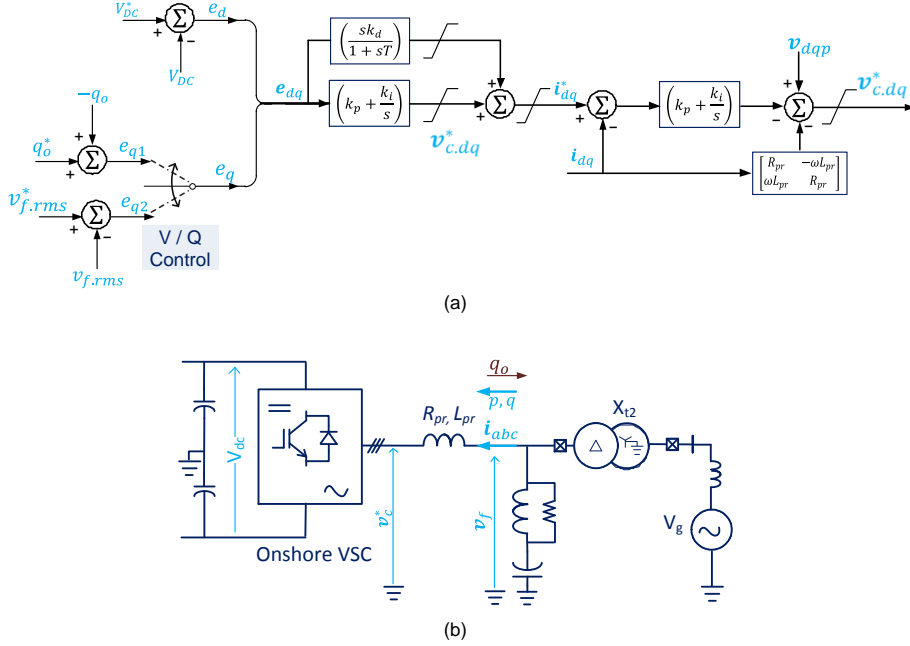


Figure 3.15. Onshore VSC-HVDC; (a) Controller block diagram; (b) Circuit schematic

$$i_d^* = -k_{p2}(V_{DC}^* - V_{dc}) - k_{i2} \int (V_{DC}^* - V_{dc}) \quad (3.21)$$

$$i_q^* = k_{p3}(Q_{ac}^* - Q_{ac}) + k_{i3} \int (Q_{ac}^* - Q_{ac}) \quad (3.22)$$

where, the superscript ‘*’ indicates the reference quantities.

The parameters of these three PI-controllers were tuned using pole cancellation technique. It is described in the Appendix B. A kind of derivative

controller has been added in the d -axis current controller in order to improve the transient performance.

3.15.2 Offshore Grid Converter

The basic function of the offshore VSC controller is to maintain the voltage and the frequency in the offshore WPP grid. Since the frequency is predefined as external reference to this converter, a PLL is not required [8], [10]. Likewise the onshore VSC controller, this controller, too, can be modelled in the synchronously rotating reference frame (or the dq frame given by the Park's transformation) and then the PI controllers can be used. However, separate controllers are required when the positive and negative sequence current controllers have to be implemented. The positive sequence PI controller is described here as the basic controller; and the negative sequence current controller will be described in Chapter 6.

The block diagram of the controller in synchronously rotating reference frame is given in Figure 3.16. The governing equations of the inner current control loop of the controller are similar to (3.19)-(3.20) except that the voltage feed-forward terms are removed. They are as follows:

$$v_d^* = -i_d R_{pr} + \omega L_{pr} i_q - k_{p4}(i_d^* - i_d) - k_{i4} \int (i_d^* - i_d) \quad (3.23)$$

$$v_q^* = i_q R_{pr} - \omega L_{pr} i_d - k_{p4}(i_q^* - i_q) - k_{i4} \int (i_q^* - i_q) \quad (3.24)$$

The outer voltage control loop is basically a positive sequence voltage controller. It generates the intermediate current references, $(i_{d0}^* + j i_{q0}^*)$ from the error between the reference voltage, $(u_d^* + j u_q^*)$ and the positive sequence voltage $(u_{dp} + u_{qp})$ offshore grid voltage measured at the filter bus. The equations are given below,

$$i_{d0}^* = k_{p5}(u_d^* - u_{dp}) + k_{i5} \int (u_d^* - u_{dp}) \quad (3.25)$$

$$i_{q0}^* = k_{p5}(u_q^* - u_{qp}) + k_{i5} \int (u_q^* - u_{qp}) \quad (3.26)$$

When the WPP is operating, it injects the active and reactive power to the offshore VSC-HVDC terminal. The corresponding current can be measured and added to the current reference as feed-forward terms as explained in [10]. When the currents were directly measured and applied as feed-forward terms,

the transient performance of the controller is not good as the feed-forward current terms are much dominant than the reference generated by the outer loop controller. Therefore instead of measuring the current, active and reactive power is measured and the current feed-forward terms due to WPP injection are calculated using the measured positive sequence voltage u_{dp} (u_{qp} is 0), as follows,

$$\begin{bmatrix} i_{wpp,d} \\ i_{wpp,q} \end{bmatrix} = \frac{2}{3u_{dp}} \begin{bmatrix} P_{wpp} \\ -Q_{wpp} \end{bmatrix} \quad (3.27)$$

This ensures that the advantage that the voltage is always aligned along the d-axis in the positive sequence; thereby leading to improved performance during transients and recovery from faults.

The power frequency current drawn by the tuned filters can be calculated by,

$$\begin{bmatrix} i_{f,d} \\ i_{f,q} \end{bmatrix} = \begin{bmatrix} 0 & -\omega C_f \\ \omega C_f & 0 \end{bmatrix} \begin{bmatrix} u_d \\ u_q \end{bmatrix} \quad (3.28)$$

where, C_f is the effective capacitance of the filter at power frequency.

Finally, the overall current reference ($i_d^* + ji_q^*$) is given by,

$$\begin{bmatrix} i_d^* \\ i_q^* \end{bmatrix} = - \begin{bmatrix} i_{d0}^* \\ i_{q0}^* \end{bmatrix} + \begin{bmatrix} i_{wpp,d} \\ i_{wpp,q} \end{bmatrix} - \begin{bmatrix} i_{f,d} \\ i_{f,q} \end{bmatrix} \quad (3.29)$$

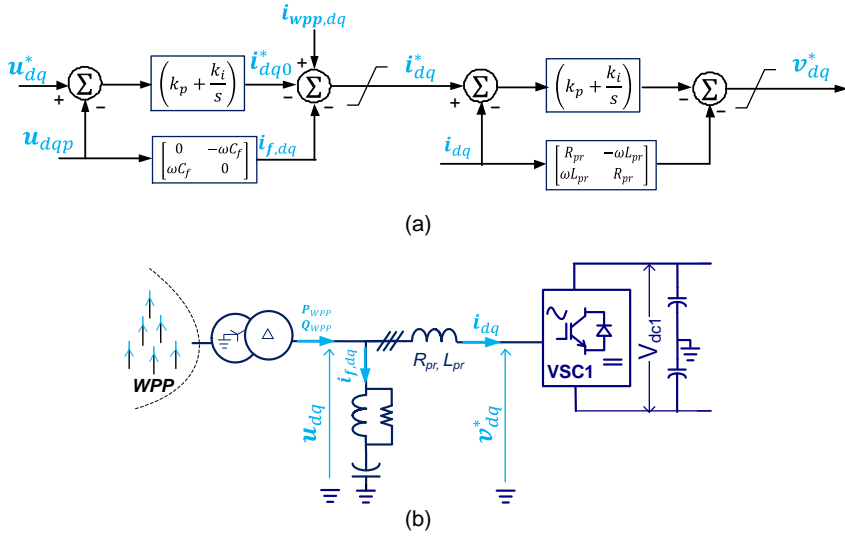


Figure 3.16. Offshore VSC controller.

3.16 Overall Control Structure

Additional controllers can be added on top of the individual converter or turbine controllers as shown in Figure 3.17 for specific purposes.

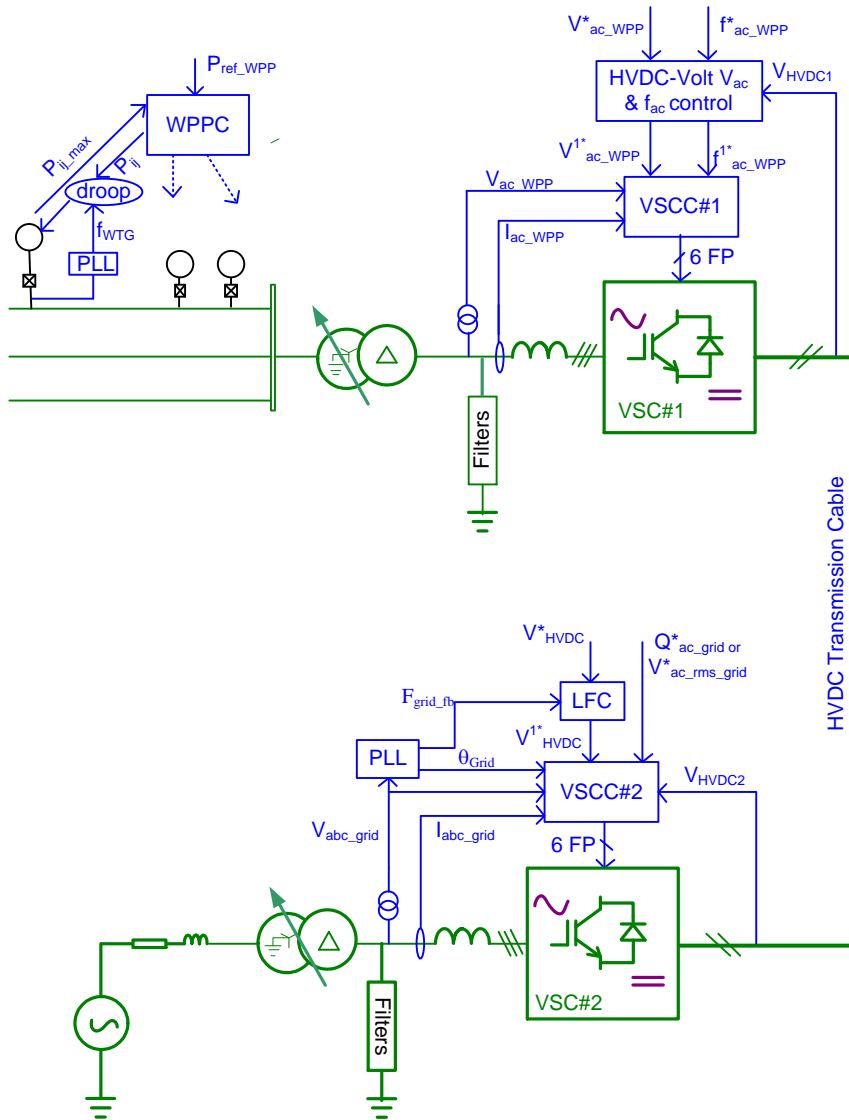


Figure 3.17. Overall control structure of the WPP with VSC-HVDC connection.

This figure shows the overall control scheme for the participation of the offshore wind power plant in the onshore grid frequency control as well as low voltage ride through. No communication is envisaged here. The dc reference voltage of the HVDC system is varied as a function of the measured grid frequency. The dc voltage rise is sensed by the offshore grid converter, which responds by changing the offshore grid frequency. Thus, the onshore grid frequency can be conveyed to the offshore grid through a point to point VSC-HVDC link. The scheme is described in detail in the next chapter.

Similarly additional control functions can be provided for the purpose of fault ride through control.

3.17 Summary

A test system comprising of a large wind power plant with VSC-HVDC connection to the onshore grid has been presented here. Main circuit parameters have been determined (by assumption, by reference or by computation). The WTG and the VSC-HVDC controllers have been described as well. It is considered as a benchmark test system for this project.

4 Operation and Control of WPP with VSC-HVDC Connection

This chapter demonstrates the simulation results of different operational modes—the energization of the VSC-HVDC and the WPP, ramping up of the power, followed by ramping down and the subsequent shut-down of the whole system. A single line to ground fault is simulated to show the robustness of the control structure. Finally the frequency regulation and fault ride through cases have been demonstrated.

4.1 Operational Modes

A sequence of events was simulated to demonstrate the normal operation of the WPP with VSC-HVDC connection to the onshore grid. The WPP and VSC-HVDC is started from completely de-energized state, and the power is ramped up to the rated values. Afterwards the power is ramped down, and the whole system is de-energized in the end. The sequence of events is listed in Table 4.1.

4.1.1 Charging of VSC-HVDC Lines

In the beginning, the VSC-HVDC, as well as the offshore WPP grid, was in de-energized state. When the circuit breaker (CB) is closed, the onshore VSC-HVDC terminal got connected to the grid through the converter transformer. Though the VSC was blocked, the anti-parallel diodes in the VSC conducted, and a large inrush current flowed in to charge the HVDC capacitors. The cable capacitance and the dc capacitors on the dc side of the rectifier were charged to the peak line to ground voltage levels, i.e. ± 138.8 kV or 277.6 kV pole-pole voltage when the ac side was connected to the 170 kV (line–line, rms) grid as shown in Figure 4.1.

The initial magnitude of inrush current was limited by the impedance of the grid, converter transformers and the phase reactors. Even then, pre-insertion resistors were required to avoid the sudden current surge flowing to the VSC. In this simulation, pre-insertion resistors of 1 k Ω was used for a period of 70 ms. Then the onshore VSC was de-blocked so that the dc line voltages got regulated to the nominal dc voltage level of 300 kV.

Table 4.1. Event list for the demonstration of the normal operating modes of the WPP with VSC-HVDC connection

| Time | Event |
|--------|---|
| 0.00s | All CBs are open. All controllers are disabled |
| 0.05s | Onshore grid CB is closed. Pre-insertion resistance is 1 k Ω . By pass resistance remains in circuit for 70 ms. |
| 0.20s | The onshore VSC is de-blocked. Its controller is enabled. |
| 0.40s | The offshore VSC is de-blocked and its controller is enabled. The offshore converter transformer is connected by the circuit breaker. |
| 0.50s | The WTG controllers are enabled. |
| 0.60s | The WTG #1 breaker is closed. Other WTG breakers get closed sequentially. |
| 1.40s | Power reference is set to 400MW. This power order gets divided to the four aggregated WTGs. Maximum rate of change of power is 250MW/sec. |
| 4.5s | <i>A single line to ground fault is applied at the point 'FA' on the feeder connecting WTG 4. (The fault is not a part of normal operation. It is included here just to show that the complete control system can withstand a transient fault).</i> |
| 5.40s | Power order is set to 0. Power order falls at the rate of 250 MW/sec. |
| 8.40s | The WTG1 circuit breaker is opened. |
| 9.60s | The WTG voltages are set to 0. WPP circuit breaker is opened. |
| 9.80s | The offshore VSC is blocked. |
| 10.40s | Onshore VSC voltage reference is set to 0. |
| 10.90s | Onshore VSC is blocked and the onshore grid transformer is opened. |

4.1.2 Energizing the Offshore Grid

After the VSC-HVDC voltage was stabilized, the offshore VSC was de-blocked. Its controller ramped up the ac reference voltage and the offshore voltage gradually built up. After the nominal voltage level had been attained in the offshore-grid, the WTG cable strings were sequentially connected to the collector bus in order to avoid undue oscillations. At this point of time, the WPP was fully energized, and the WTGs were ready for synchronization. Figure 4.2 shows the voltage and current waveforms under these conditions. A

small power flowed from the onshore grid to meet the no load losses of the system.

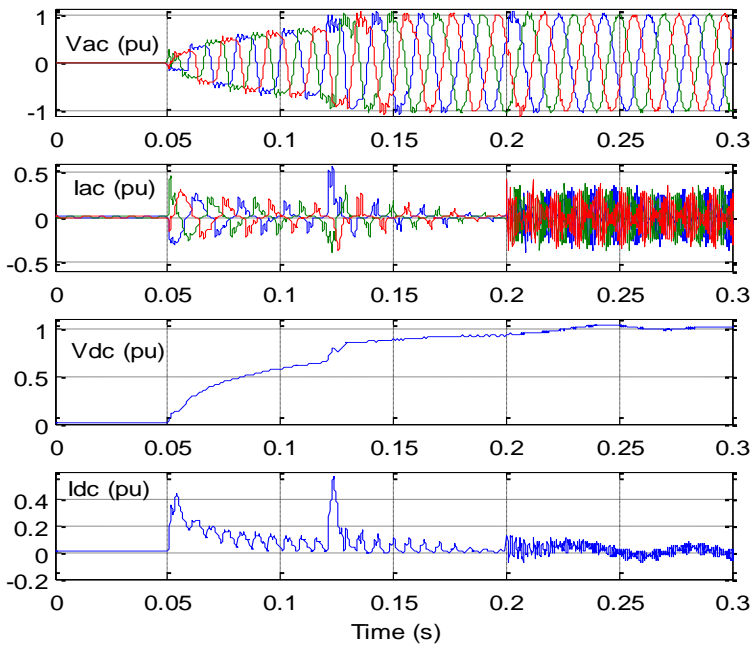


Figure 4.1. Energization of the VSC HVDC system. V_{ac} is the filter bus voltage of the onshore VSC-HVDC terminal, I_{ac} is the current through the onshore phase reactors, V_{dc} is the dc link voltage, and I_{dc} is the dc line current.

4.1.3 Synchronization of the WTGs and Power Control

In this case, the WTGs were running at rated voltage but with no load generation. First they had to get synchronized to the offshore grid voltage. The positive sequence voltage was estimated from the terminal voltage using dual second order generalized integrator (DSOGI) filters, and synchronization was achieved using the frequency locked loop (FLL) [53], [54]. When the power generation picked up, the dc-link voltage regulation set the power reference for the WTG-GSC. However, the actual power control lied with the WTG, and machine side converter controls. The reactive power reference might have been set by an auxiliary terminal voltage regulation loop or it could be externally set. In the simulated case, it was set to zero. Positive sequence current references were generated from the estimated positive sequence voltage, and the active and reactive power orders as per (3.7). Then, they were controlled using the

proportional resonant controllers in the stationary reference frame as described in the previous chapter.

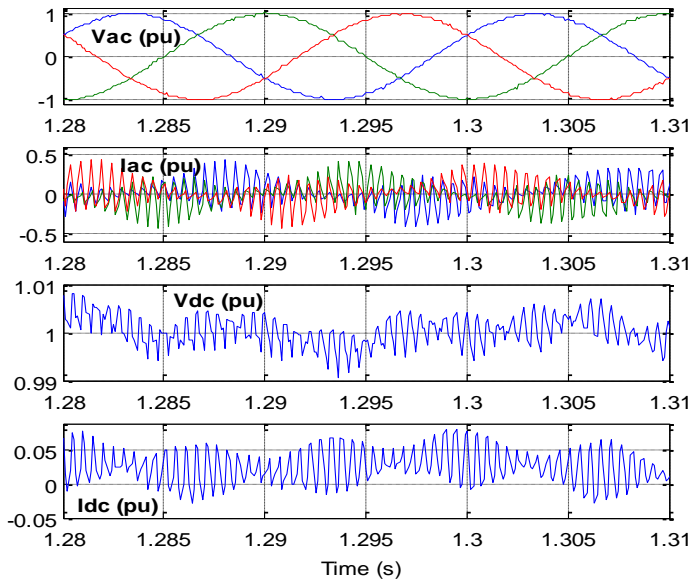


Figure 4.2. Waveforms when the offshore collector grid was energized and the WTG units were connected. V_{ac} – the filter bus voltage of the onshore VSC-HVDC terminal; I_{ac} – the current through the onshore phase reactors; V_{dc} – the dc link voltage; and I_{dc} – the dc line current.

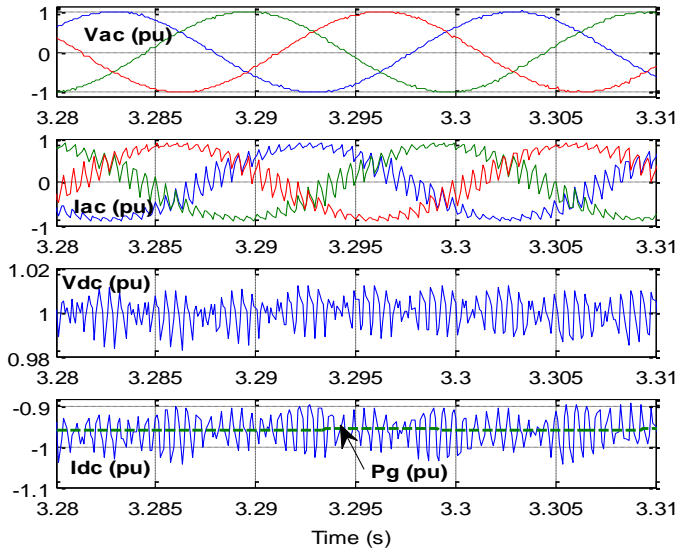


Figure 4.3. Steady state operation at full load. V_{ac} – the filter bus voltage of the onshore VSC-HVDC terminal. I_{ac} – the current through the onshore phase reactors; V_{dc} – the dc link voltage; and I_{dc} – the dc line current.

4.1.4 Steady State Operation

Figure 4.3 shows the ac voltage and current waveform at the onshore VSC-HVDC terminal when the WPP was generating nominal 1 pu power. The dc link voltage ripple was less than 1%, while there was significant ripple in the dc current even at nominal power ratings. The dc current was measured between the HVDC cable and the dc capacitors.

Figure 4.4 shows that the WTGs had to absorb the reactive power throughout the operating range as the collector grid is capacitive in nature. It also shows the impact of a transient single line to ground fault of 150 ms duration at a 36 kV collector bus (for WTG#4).

During the single line to ground fault, power flow got disturbed for some time and power output from WTG #1 also got affected. High ripples were observed on the HVDC system during the fault, but they settled down to nominal levels soon after the fault was cleared.

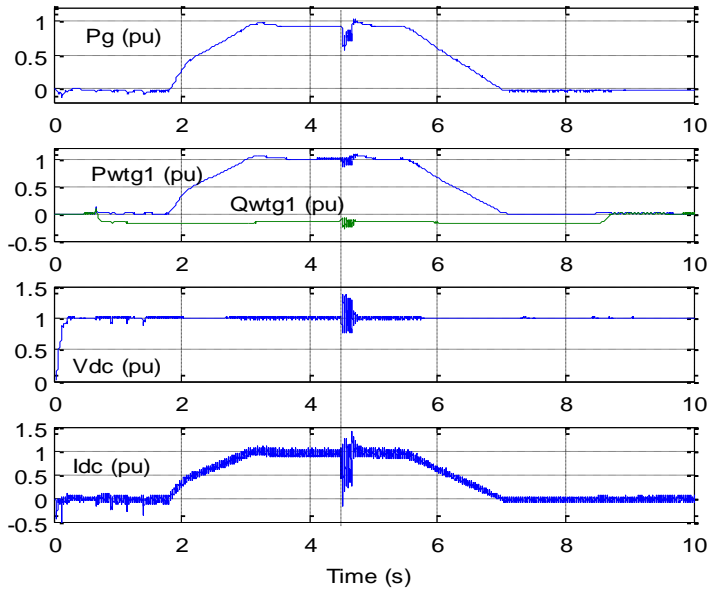


Figure 4.4. Full operating range (with a single line to ground fault at 4.5 s).

4.1.5 WPP Shut Down

In this step the reference power to the WTGs was set to zero and the power generation was ramped down as shown in Figure 4.4. Then the whole plant was shut down in a controlled way. First the WTGs were shut down, and then the offshore VSC-HVDC terminal was blocked. Then the onshore VSC was blocked. The dc system had trapped dc voltage which would take a long time to discharge by itself. Discharge resistors had to be connected to ensure a quicker discharge.

4.2 Frequency Control through VSC-HVDC Transmission

Traditionally the conventional power plants have been providing the grid frequency support in terms of inertial response, primary, secondary and tertiary frequency regulation in the event of power unbalances. With the increase in the penetration of wind power in the power system, grid operators are putting regulations for the participation of wind power plants in frequency regulation. The German and Danish grid codes are briefly discussed here and then a simulation study of grid frequency control in the wind power plant with VSC-HVDC connection is presented.

4.2.1 German Grid Requirement on Frequency Regulation

Grid codes specify the frequency control capabilities of the power generation plants for grid connection. The German Grid code [11] states that all generating plants should be capable of reducing their output power at the rate of 1% of the rated power per minute across the entire range of operation. Large generating plants of 100 MW or larger plant sizes must be able to contribute to the primary frequency regulation with a control band of at least 2% of the rated power and adjustable frequency power droop characteristics. The total primary control power must be activated within 30s for a quasi-stationary frequency deviation of ± 200 mHz, and it must be supplied for at least 15-minute duration. This gives a droop characteristic of 20% regulation i.e. the active power generation changes by 100% for 20% change in frequency. The insensitivity range must be less than ± 10 mHz.

An over-frequency in the grid implies that there is excess of generation than the load demand and hence the power plants are required to cut down the

generation. Wind power plant generation can be brought down by varying the operating point through the control of pitch angle, β and tip speed ratio, λ . There are problems when there is under-frequency and the power generation has to be ramped up. Since wind energy is not a controllable source of power, power cannot be ramped up if it is already operating under maximum power point tracking regime. De-rated operation (i.e. less than maximum available wind power) has been proposed to provide margin for eventual frequency support [22]. Deviations and amendments were provided in the Grid code for offshore wind [12], whereby offshore wind power plant has to reduce power generation during over-frequency conditions in the grid as shown in Figure 4.5. When the grid frequency exceeds 50.1 Hz, power has to be reduced at the rate of 98% per Hz drop in the grid frequency, and 25% per second of the active power available at the moment. The unit should be disconnected after 10 seconds if the frequency remains at or above 51.5 Hz.

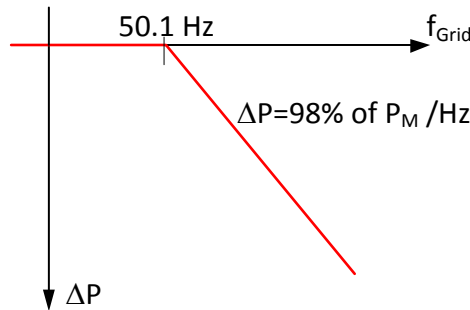


Figure 4.5. Active power reduction at over-frequency.

4.2.2 Danish Grid Requirement on Frequency Regulation

The Danish grid requirement for frequency regulation is shown in Figure 4.6 [13]. There are two regulation curves: the first one provides only the downward regulation during over-frequency, while the second has a provision for both upward and downward regulations. If the wind power plant is generating the maximum available power, then it can provide only downward regulation when there is over-frequency. It cannot participate in the upward regulation required during under-frequency. On the other hand, if it is generating a de-rated amount of power as given by the set-point value at downward regulation, it can participate in both the upward and downward

regulation. A de-rated operation would imply an undue loss of energy and revenue by virtue of reduced generation under normal frequency conditions.

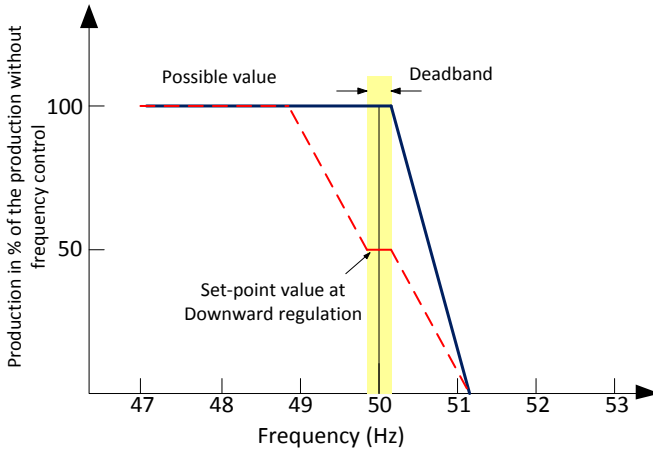


Figure 4.6. Frequency regulation with and without previous downward regulation (Denmark grid code [13])

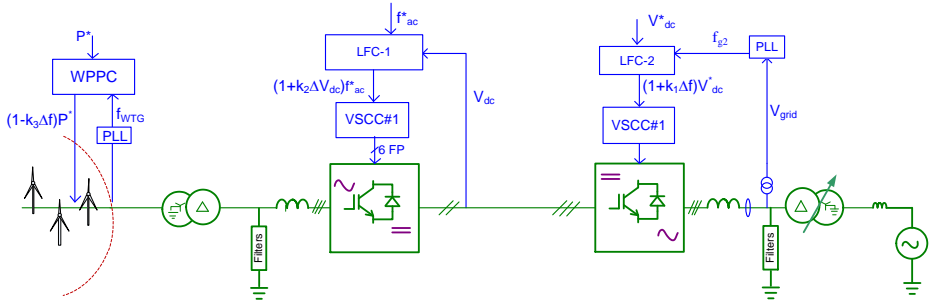
4.2.3 Frequency Regulation through VSC-HVDC Transmission

VSC-HVDC transmission provides an asynchronous connection between the offshore and the onshore grids. The offshore grid frequency is completely decoupled from the onshore grid frequency. Therefore, for the participation of the offshore WPPs in frequency regulation, either the grid frequency has to be relayed to the offshore grid or the power order to the offshore wind power plant should be continuously updated and communicated as per the grid frequency conditions. As described in [22], there can be three different ways of relaying or communicating the onshore grid frequency to the offshore wind power plant (Figure 4.7):

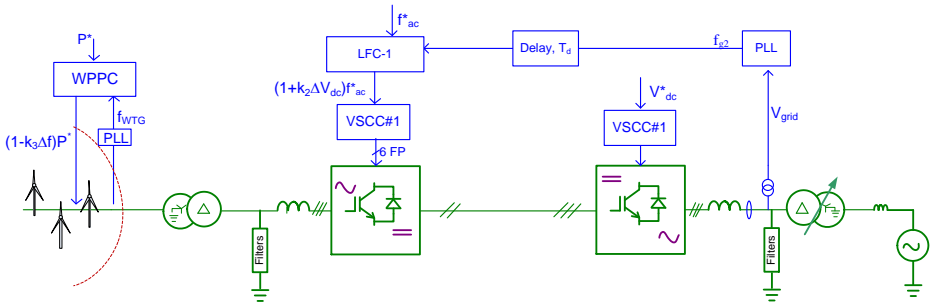
4.2.3.1 Using the dc voltage and offshore grid frequency

The onshore VSC-HVDC reference voltage is changed in proportion to the onshore grid frequency. If the frequency is increasing the dc voltage reference is increased. Consequently, the dc voltage at the offshore VSC-HVDC terminal increases too. The offshore VSC terminal voltage is measured and compensated for the voltage drop across the HVDC line impedance to estimate the nominal dc voltage. A deviation in the estimated dc voltage from the nominal is used to

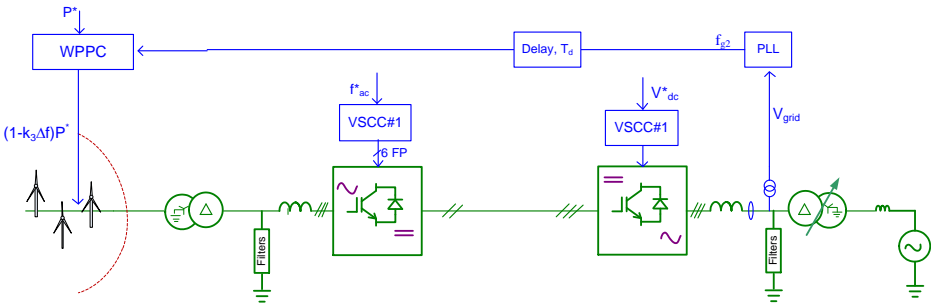
modify the frequency reference for the offshore grid. Therefore, if there is an increase in the onshore grid frequency, the dc voltage is raised and eventually the offshore grid frequency is raised. The grid converters in the WTGs sense the frequency increase, and therefore, decrease their generation as per the pre-set droop characteristics. This is shown in Figure 4.7(a).



(a) No Communication used



(b) Communication of onshore grid frequency to the offshore VSC-terminal



(c) Communication of onshore grid frequency to the WTGs

Figure 4.7. Frequency regulation by WPP through VSC-HVDC connection.

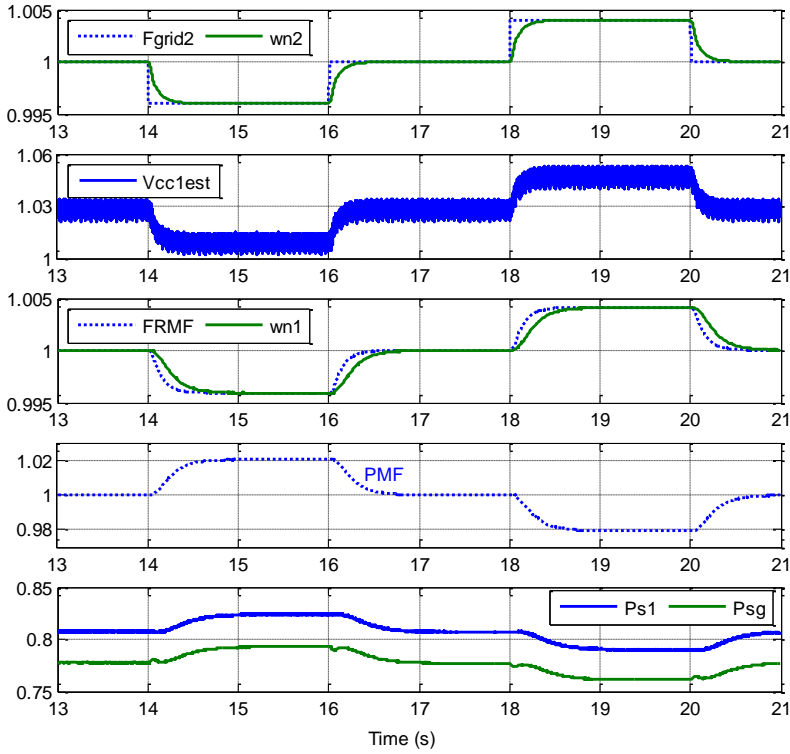


Figure 4.8. Frequency regulation through VSC-HVDC using the dc voltage and offshore frequency for relaying – change of dc voltage, offshore frequency and the power flows.

Figure 4.8 and Figure 4.9. show the simulation results for this case. A frequency change was simulated by introducing the step changes in the frequency (F_{grid2}) voltage source model for the onshore grid. The onshore grid PLL measured the grid frequency ($wn2$). It was used to change the dc reference voltage of the onshore VSC-terminal using a multiplication factor ($DCVMF$). Consequently the HVDC voltage on the onshore terminal changed (V_{dc2}). The offshore HVDC terminal voltage (V_{dc1}) changed as well. It was compared with the nominal offshore voltage estimated (V_{dc1est}) for the measured load current and the offshore frequency ($wn1$) was changed. The WTG-FSC then changed the power reference to the WTG-FSC as per the pre-set droop and frequency regulation was achieved.

The power generated, ($Ps1$) and hence injected (Psg) to the grid, changes are shown in the Figure 4.8. It is represented by the curve $FR1$ in Figure 4.10.

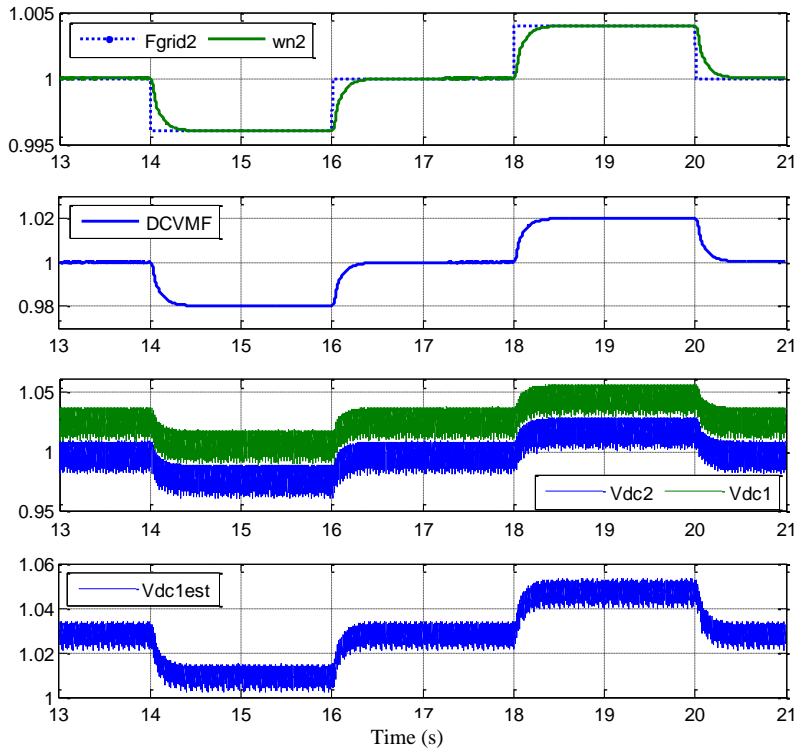


Figure 4.9. Frequency regulation through VSC-HVDC using the dc voltage and offshore frequency for relaying – change of dc voltage, and estimation of the voltage change.

4.2.3.2 *Communicating the onshore grid frequency to the offshore grid VSC-terminal and then varying the offshore grid frequency*

The onshore grid frequency is directly communicated to the offshore grid VSC-converter using communication channels. The offshore VSC-HVDC changes the offshore grid frequency such that the onshore grid frequency is replicated. The advantage is that the dc voltage need not be changed in this method.

In the simulation study, a filter with 100 ms time constant was used at the onshore frequency measurement. It was assumed to account for both the filtering delay and the communication delay. The resultant power flow for frequency regulation is shown by the curve $FRC2$ in Figure 4.10. .

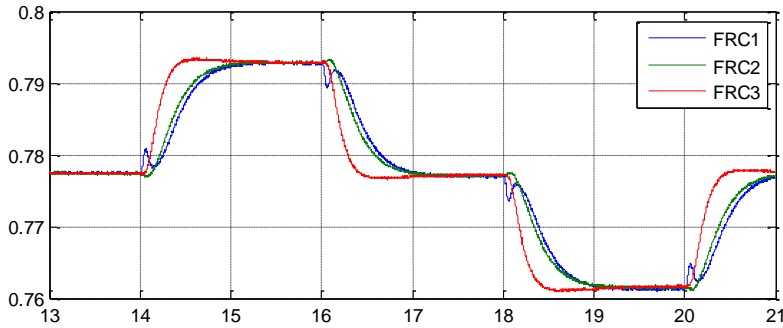


Figure 4.10. Comparison of the power flow change as a result of frequency regulation using the three methods.

4.2.3.3 *Communicating the onshore grid frequency to the offshore WPP*

If reliable communication is available, this is the most suitable method as the only delay is due to communication delay. No disturbance in the HVDC voltage or the onshore grid frequency is introduced as such. The power curve *FRC3* shows this kind of regulation with an assumed time delay of 100 ms which is modelled here as a first order transfer function.

Since frequency control involves relatively slow variation of power and the full response has to be achieved in a period of 30s, all three methods are equally suitable.

4.3 Fault Ride Through Using VSC-HVDC Transmission

When there is a fault on the onshore ac grid, the ac grid voltage at the point of common coupling (PCC) dips, thereby reducing the power transfer capability from the onshore VSC-HVDC terminal. Power flow to the VSC-HVDC can be rapidly controlled by the other terminal when it is connected to two strong power system grids. However, when it is connected to a wind power plant, it is not so convenient. The rating of the VSC-HVDC is almost the same as that of the wind power plant rating. Since the WPP power generation cannot be brought down instantaneously, the excess power gets accumulated in the VSC-HVDC system capacitance, thereby, leading to over-voltage in the dc system.

4.3.1 E.ON Grid Code for Fault Ride Through

According to the E.ON Netz Grid Code [11], large generating stations of sizes 100 MW or larger must stay connected and provide voltage support to the grid in the event of nearby faults for a period of up to 150 ms as shown in Figure 4.11. The generating unit must remain connected as long as the operating point (voltage and duration) remains above the limit Line 2. A conditional disconnection is allowed if the operating point lies between Line 1 and Line 2. Further the generating plant should be capable of providing voltage support during grid disturbances.

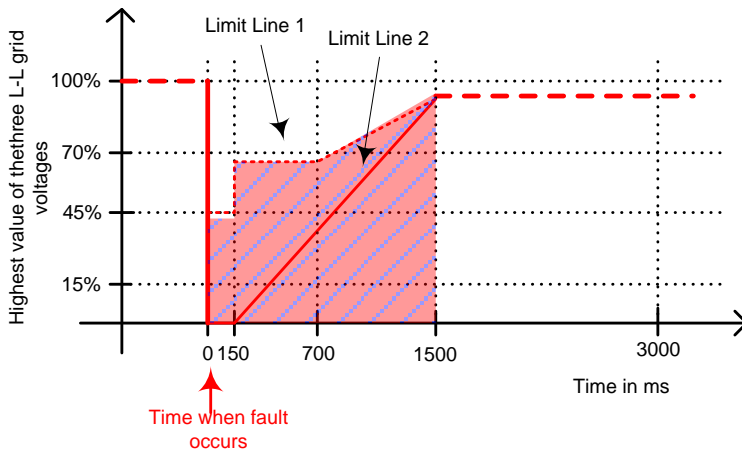


Figure 4.11. Fault Ride Through (FRT) requirement of E.ON Netz Grid Code [11].

A reactive current of the order of 2 pu per pu voltage drop should be injected when the voltage drops below the $\pm 10\%$ dead-band [11] and absorbed at the same slope for voltage rises as shown in Figure 4.12.. As per the grid codes for the offshore generation plants [12], the dead-band is $\pm 5\%$ at the point of common connection which is considered the offshore point. In this project, the VSC-HVDC is a dedicated transmission for the wind power plant, and the point of common coupling is assumed to be at the onshore inverter station.

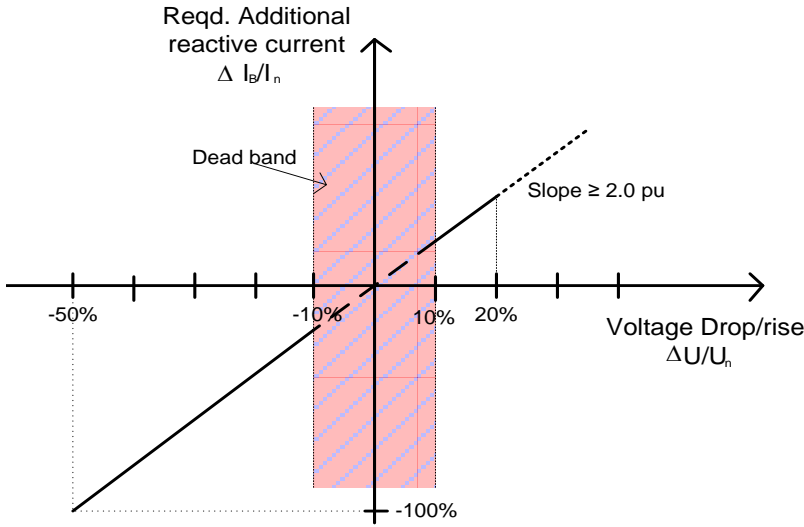


Figure 4.12. Reactive current injection requirement for voltage support during grid disturbances.

4.3.2 Chopper Resistor for Fault Ride Through

Chopper controlled resistor is used to dissipate the excess power, and thus limit DC voltage rise within safe levels; while the WTGs are signaled to reduce their generation as quickly as possible [46]. It is installed in HVDC Nord E.ON 1 (now referred to as BorWin 1) to prevent dc over-voltages by temporarily dissipating the excess power [55]. In variable frequency drives, it is referred to as braking resistor and is used to dissipate the braking energy [56]. A similar arrangement is provided in the WTG-FSC to limit the dc link over-voltages [57]. In this section the performance of the chopper resistor in the FSC is evaluated for controlling the HVDC system over-voltage during low voltage faults in the onshore grid.

Mathematically, the power transferred between the converter terminals and the PCC bus is given by the power transfer relationship

$$P_{cg} = \frac{V_c V_g}{X_{ph}} \sin(\delta_c - \delta_g) \quad (4.1)$$

where, P_{cg} is the power transferred from the converter to the grid and X_{ph} is the reactance between the converter and the grid. V and δ indicate the voltage and the voltage phase angle at the converter and the grid terminals, which are

identified by the subscripts c and g respectively. According to (4.1), the power transferred from the converter to the grid will decrease to zero as the grid voltage magnitude dips to zero due to the fault in the onshore grid. If P_{wpp} is the wind power plant production being injected to the VSC-HVDC transmission, and C_{eq} is the equivalent capacitance of the dc lines and the capacitors in the VSC-HVDC system, the dc voltage rise will be given by,

$$V_{dc} = \sqrt{\frac{2}{C_{eq}} \int (P_{wpp} - P_{cg}) \cdot dt} \quad (4.2)$$

The dc overvoltage can be avoided if the surplus power, i.e. $(P_{wpp} - P_{cg})$ can be dissipated by a chopper controlled resistor in the HVDC system. If we assume that the steady overvoltage in the dc system has to be restricted to 10% of the nominal value, the value of the chopper resistor is given by,

$$R_{chopper} = \frac{(1.1V_{dc,n})^2}{P_{rated}} \quad (4.3)$$

The operation of chopper controlled resistor is similar in the case of the full scale converters of the WTGs and the VSC-HVDC. Hence the equations (4.2) – (4.4) are applicable to all of them, with their respective ratings and limits.

Since every WTG-FSC is equipped with a chopper controlled resistor for dissipation of excess power, the chopper controlled resistor in the VSC-HVDC system can be eliminated by controlling the power injected onto the VSC-HVDC system. Ref. [58] mentions three approaches of fast power reduction for fault ride through. Fault conditions can be relayed to the offshore grid by the variation of the offshore grid frequency and reduction of offshore grid voltage. Both of these can be combined together to increase the efficacy. Communicating the fault to the WTG is given a low ranking in this paper as the perceived communication delay is of the order of 10–100 ms.

4.3.3 FRT Using Fast Communication

A simulation study was carried out on the test system to observe the overvoltage during a severe fault in the onshore grid. The onshore grid voltage drop to 0.01 pu was simulated. Due to the transformer impedance between the

fault point and the filter bus and the reactive current injection from the VSC-HVDC, the filter bus voltage showed a higher residual value.

The rms voltage profile at the VSC-HVDC terminal filter bus is shown in Figure 4.13(a).

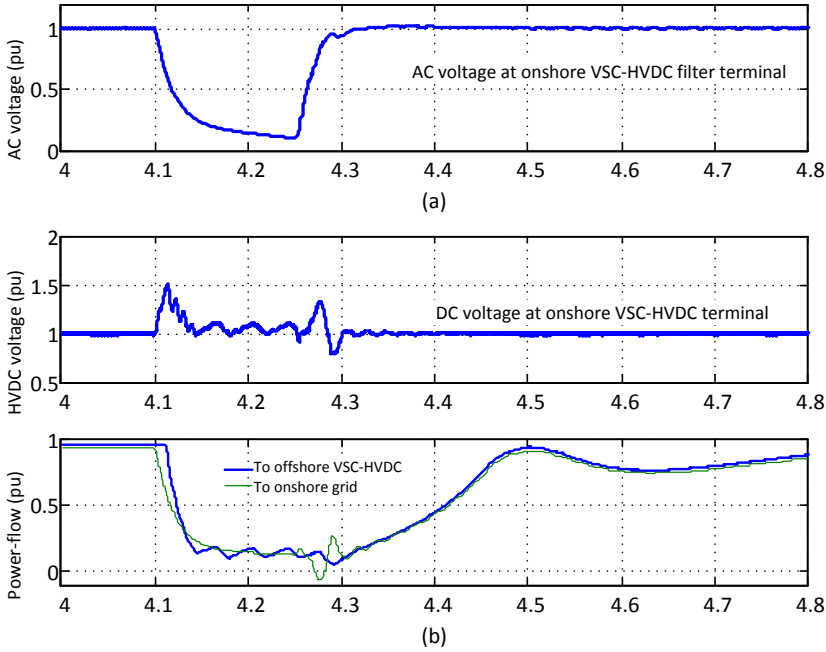


Figure 4.13. FRT using fast communication to block the WTG-FSCs during the fault in the onshore grid. (a) AC voltage at the HVDC filter bus; (b) DC voltage rise and power flow during the fault.

Because of the fault, there was a rapid increase in the dc voltage. The dc overvoltage was detected and a power ramp down command was communicated to the WTG-GSCs. A discrete delay of 8 ms was assumed for communication delay in this study. Therefore, the power injection from the offshore grid could not be stopped immediately, but only after the communication delay, as shown in Figure 4.13 (b). As a result of this, the peak transient dc voltage was 1.51 pu. When the communication time delay was increased to 10 ms, the overvoltage was 1.55 pu.

From these observations, it is obvious that this method is highly sensitive to the speed of communication between the VSC-HVDC and the WTG-GSCs.

4.3.4 FRT Using Frequency Increase and Voltage Reduction

Apart from the FRT using fast communication, two additional methods have been described in literature. In one of them, the offshore grid frequency is raised fast and the power reduction by the WTGs depend upon their controls similar to the droop control to reduce the power output as the terminal frequency increases. The WTGs have to sense the frequency rise, and accordingly, ramp down the power reference to the WTG-GSCs. Thus, this depends very much upon the times taken by the PLLs in the WTG-GSCs to note the changed frequency, and then the time taken by the WTG-GSC controllers to reduce the output power. The WTG-GSC is assumed to be capable of fast power reduction, by virtue of chopper resistors on their dc link. In the long term, the turbine operating point is changed to reduce the generation.

As shown in Figure 4.14, there was a large over-voltage of 1.86 pu during the fault ride through using the offshore grid frequency increase. Moreover, the over voltage was persistent as there was no other means to evacuate the power and thus decrease the dc voltage unless the onshore grid was restored. Even the recovery of the offshore wind power generation was found to be slow.

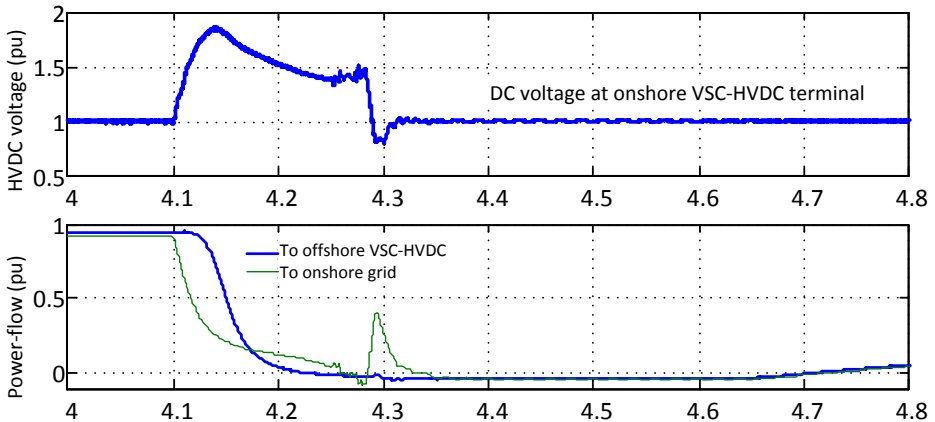


Figure 4.14. FRT of WPP with VSC-HVDC connection using offshore grid frequency increase.

In the other method, the offshore grid voltage is ramped down fast such that the power-flow in the offshore grid is impaired and the WTG-FSCs cannot inject power into the offshore grid.

In the simulation for this case, the offshore grid voltage was rapidly ramped down when the offshore VSC recorded the voltage rise. Power-flow to the HVDC terminal decreased rapidly and the maximum dc over-voltage was limited to be 1.26 pu as shown in Figure 4.15. Even the power recovery after the onshore grid voltage recovered was fast in comparison to the previous two cases.

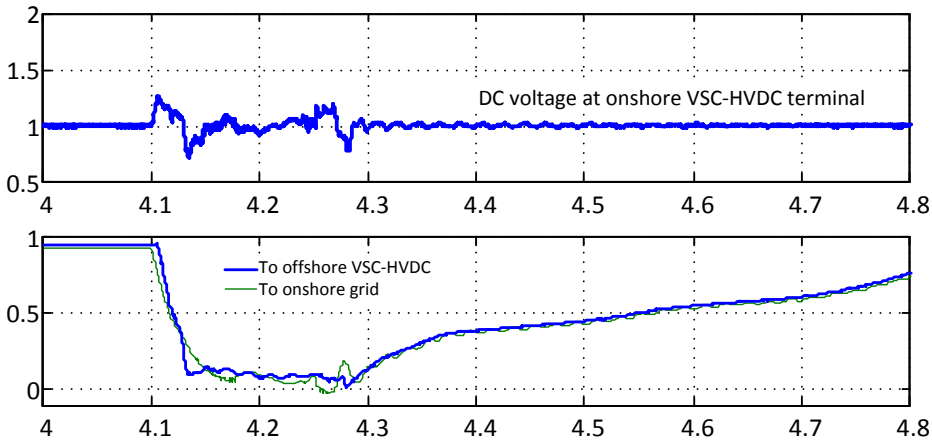


Figure 4.15. FRT of WPP with VSC-HVDC connection using offshore grid voltage reduction.

4.4 Discussion

Elimination of the chopper controlled resistors was proposed as the dc over-voltage could be limited using the fault ride through techniques. However, large transient over-voltages may appear during the onshore grid faults. The severity of such transients depends on both the extent of the voltage dips as well as the adopted control method. Based on the simulations results, the rapid reduction of voltage gives the minimum overvoltage. In this case, the low voltage conditions of the onshore grid is replicated in the offshore grid, and then the power flow to the HVDC system gets reduced in a way similar to the reduced power evacuation to the onshore grid. The WTG-GSCs do not need depend upon the PLL dynamics, like in the case when frequency rise is used for FRT.

In all these cases, it was presumed that the WTG-FSC had some means, like the chopper resistors or energy storage, which could absorb the excess energy that could not get evacuated by the WTG-GSC.

4.5 Summary

This chapter described the different operating modes of the WPP with VSC-HVDC connection under normal conditions. Later the control modes for providing frequency regulation support to the grid and the fault ride through during low voltage faults in the grid are demonstrated.

Enabling frequency control through the VSC-HVDC link was demonstrated using the three methods described in literature. Since frequency regulation is a slow phenomenon acting over a period of 30s, all three methods were found to be equally acceptable .

For fault ride through conditions, rapid reduction of voltage is found to be the best method to limit the dc link overvoltage transient. It was demonstrated that the rapid voltage reduction method could limit the dc overvoltage to 1.26 pu even for the severe faults in the onshore grid. This method of FRT could be used, and the chopper resistors can be eliminated completely.

5 Protection System for Offshore WPP Grid with VSC-HVDC Connection

This chapter analyses faults in the offshore collector system grid. First a simple numerical method is proposed to get approximate values of the fault current levels under different operating conditions. Then the EMT simulation is run to ascertain the actual fault currents and test the coordination of the over-current relays at the strategic locations in the collector system.

5.1 Introduction

Commercial wind turbine generators are of few MW unit size. Therefore, a wind power plant of a few hundred MW capacity deploys a few hundred wind turbine generators (WTG). Large offshore wind power plants (WPP) are spread over a large area (e.g. 35 sq. km for the 300 MW Thanet Offshore Wind Farm in the UK [59]). Since offshore maintenance work is expensive and time consuming [27]; the protection system should be secure and reliable. Any fault in the collector system will adversely affect power generation of the whole WPP. Therefore, fault detection and isolation of the faulted sections is very important in order to facilitate the operation of the healthy sections of the offshore WPP.

Protection of a radial feeder is a well-understood topic. In a conventional radial feeder network, the coordination of over-current relays is conducted with the knowledge of the short circuit current contribution from the rotating machines. However, the offshore wind power plant collection grid is different as rotating machines are connected to the grid through full-scale power electronic converter interfaces. Such converters have limited short-circuit current capability [60] in the range of 1.1 to 1.5 pu. Moreover, they tend to generate more harmonic components during faults and transients. Coordination of over-current relays in such a radial collector system needs to be studied and validated. Further, since an offshore grid is composed of a large number of closely laid short cable sections, conventional distance protection logic is not applicable.

Most of the studies on WPP protection are focused on their response to grid disturbances and low voltage fault ride through requirements imposed by the

grid operators [15], [60]–[62]. Several other studies address the impact of distributed generation on the protection and relay coordination in the distribution system [63], [64]. Reference [65] describes a protection scheme using IEC-61850 process bus communication for the adaptive setting and coordination of protective devices in smart grids with inverter connected distributed power generation. An integrated protection and control system for wind farms is presented in [66] using the IEC-61850 communication and a centralized relaying unit with parallel-processing ability.

Apart from the limited short circuit current capability of the inverters, their dependence upon the controller, PLL, and terminal voltage for synchronization affect their response to short circuit faults. If the converter current exceeds permissible limits the converter switching gate pulses are momentarily blocked. The harmonic levels in the terminal voltage and current waveforms increase due to the transients and disturbances as well as the non-linear response from the converters.

This chapter presents a simplified approach for the estimation of fault currents, and then a coordination strategy for the protection scheme using over current relays has been proposed. It is verified through electromagnetic transient (EMT) simulation. In Chapter 7, an experimental verification using a physical relay in a real time simulation with RTDS is presented.

5.2 Overcurrent Relay

Over-current relays with very inverse time characteristics can be coordinated to detect and discriminate faults in the cable feeders connected to the collector bus of the offshore WPP. Since several WTGs are connected to a common cable feeder, they may be provided with a common circuit breaker, as in the Horns Rev I layout [67].

When there is a short circuit fault in a feeder, the over-current relay should trip the circuit breaker and isolate the faulted section. The following points are particularly helpful in the relay coordination procedure:

- I. Each WTG-GSC is protected by its own current limit controller.
- II. The VSC-HVDC (VSC1 in Figure 3.1) is the largest converter in the wind power plant grid in terms of absolute ratings. Therefore; it has the maximum contribution to the fault currents; though other WTG-GSC's also contribute to the fault current.

- III. All the power electronic converters are capable of limiting their current output to their over-current limits, which is assumed here to be 1.10 pu for the WTG-GSC's and 1.15 for the VSC-HVDC converter.

Relay co-ordination studies are done to set the pick-up current ($I_{pick-up}$) and time dial setting such that proper discrimination is attained for the different types and strengths of faults. As per, IEEE Std. C37-112 [68], the over-current relay trip time, $t(I)$, for the relay current transformer (CT) current ' I ' is given by (5.1),

$$t(I) = \left(\frac{A}{M^p - 1} + B \right) \quad (5.1)$$

$$M = \left(\frac{I}{I_{pick-up}} \right)$$

where, $A = 19.61s$, $B = 0.491s$, $p = 2$, for very inverse characteristics and $I_{pick-up}$ is the relay pick up current setting. The characteristic curve is shown in Figure 5.1. The trip time given by (5.1) can be modified by the time dial setting to obtain the actual trip time of the relay.

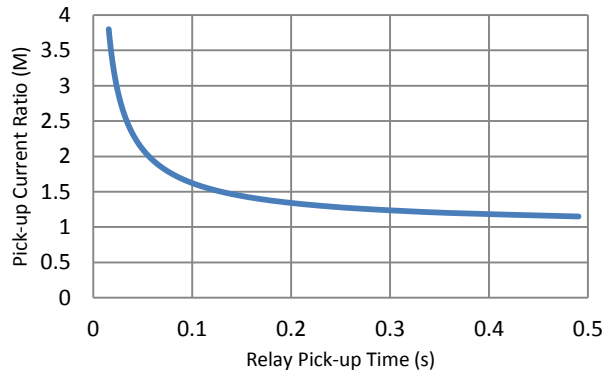


Figure 5.1. Very inverse characteristics of the over-current relay (IEEE Std. C37-112) [69].

In a conventional relay coordination study, the pick-up current is set-up on the basis of short circuit analyses. High short circuit currents are observed in conventional power systems and the relays are coordinated with other relays such that they trip for the faults in their own zone. The trip time is adjusted by using their time multiplier settings.

5.3 Approximate Calculation for the Fault Currents

The following assumptions are made in the calculation of fault currents:

1. The grid side converter of WTG-FSC tends to act as current source, to evacuate the generated power. The WTG with their converters are treated as current sources, operating at their maximum current limits [69].
2. The VSC-HVDC behaves as a current source when the fault current tends to exceed the maximum current limit.
3. Shunt capacitances of the filters and the cables are neglected.
4. Pre-fault load conditions have been ignored.
5. All the current sources are assumed to be in phase, thereby giving the worst case results as the fault currents get added up.
6. Symmetrical and steady state fault conditions have been assumed.

With these assumptions, the equivalent positive sequence circuit of the offshore collector grid is shown in Figure 5.2. Fault currents are computed for the three-phase short-circuit faults at locations *FA* and *FB* for six different cases as follows:

- C1. ALL WTG feeders are operational.
- C2. WTG feeder #1 (or #2) is switched off.
- C3. WTG feeder #3 is switched off.
- C4. WTG feeders # 1 and 2 are switched off
- C5. WTG feeders # 1 and 3 are switched off
- C6. WTG feeders # 1, 2 and 3 are switched off.

The results for these six cases are summarized in Table 5.1 and Figure 5.3. Fault currents are given in per unit values with the base current defined corresponding to the MVAs of their respective sections, as shown in Figure 5.2. Therefore, 1-pu current in the converter transformer section will be equivalent to 2-pu current in the high voltage (HV) feeder section and 4-pu current in the medium voltage (MV) feeder section. Consequently, the per unit fault current appears to be higher for the faults in the MV feeder, compared to those for the faults in the HV feeder.

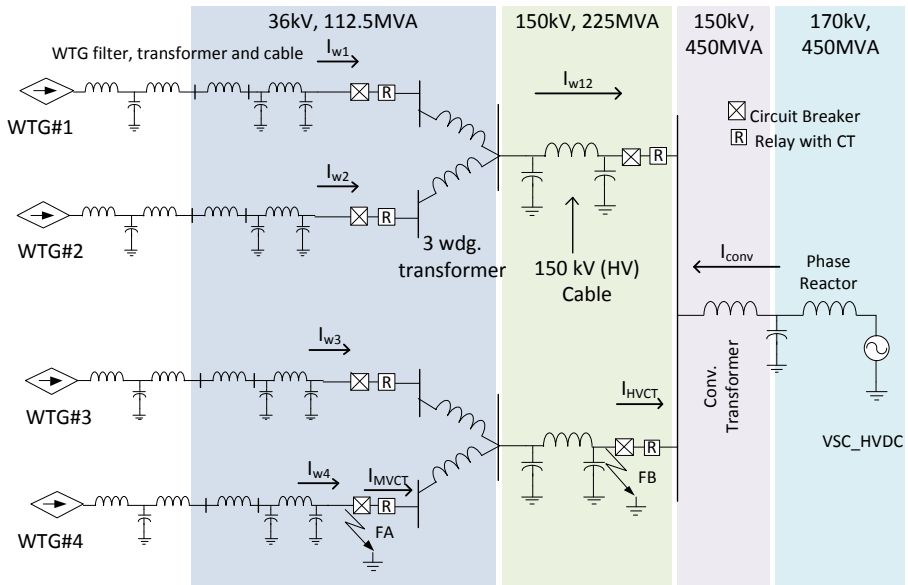


Figure 5.2. Equivalent positive sequence schematic of the offshore WPP.

Table 5.1. Fault Current and its components through different sources and CTs.

| | Case-I | Case-II | Case-III | Case-IV | Case-V | Case-VI |
|--------------------|--------|---------|----------|---------|--------|---------|
| Sources | | | | | | |
| I_HVDC | 1.15 | 1.15 | 1.15 | 1.15 | 1.15 | 1.15 |
| Iwtg #1 | 1.10 | 1.10 | 1.10 | x | x | x |
| Iwtg #2 | 1.10 | x | 1.10 | x | 1.10 | x |
| Iwtg #3 | 1.10 | 1.10 | x | 1.10 | x | x |
| Iwtg #4 | 1.10 | 1.10 | 1.10 | 1.10 | 1.10 | 1.10 |
| Fault at FA | | | | | | |
| Fault current | 9.00 | 7.90 | 7.90 | 6.80 | 6.80 | 5.70 |
| HV_CT | 3.40 | 2.85 | 3.40 | 2.30 | 2.85 | 2.30 |
| MV_CT | 7.90 | 6.80 | 6.80 | 5.70 | 5.70 | 4.60 |
| Fault at FB | | | | | | |
| Fault current | 4.50 | 3.95 | 3.95 | 3.40 | 3.40 | 2.85 |
| HV_CT | 3.40 | 2.85 | 3.40 | 2.30 | 2.85 | 2.30 |
| MV_CT | 1.1 | 1.1 | 1.1 | 1.1 | 1.1 | 1.15 |

It gives a preliminary estimate of the fault current levels that may be expected in an offshore grid with power electronic converters on all terminals. Further, it highlights that the faults on the MV WTG feeders can be easily detected by conventional over-current relays. The output of the MV WTG feeder CTs are higher than 4 pu when the fault is on the MV feeder; whereas it is limited 1.1 pu when the fault is on the HV cable feeder.

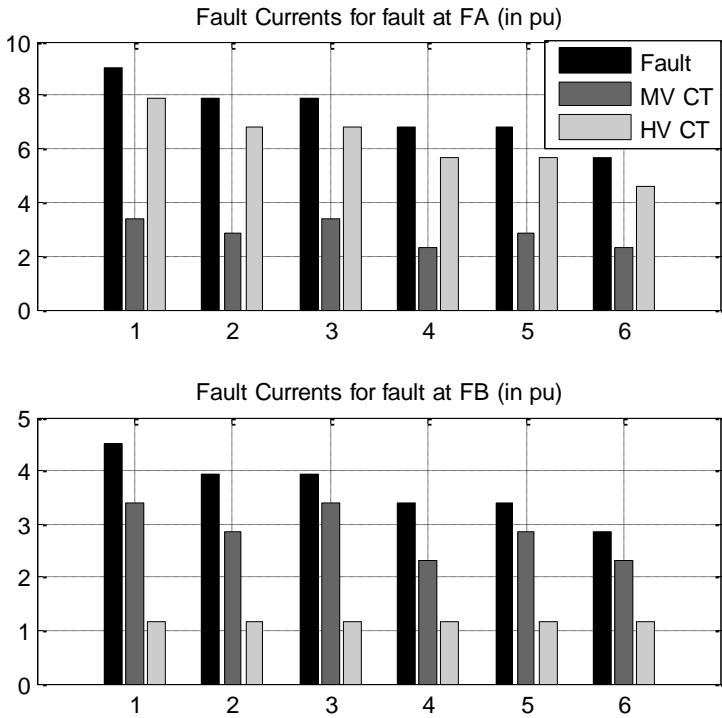


Figure 5.3. Estimated fault and CT currents for the short-circuit faults at *FA* and *FB*.

Theoretically, the HV feeder will carry the same fault currents for both the fault locations. Though the fault currents are more than twice the nominal currents, there is no discrimination between the three-phase faults on the MV feeder and those on the HV feeder. Therefore, additional information like the pick-up of the MV feeder relay might be used to block the tripping of HV feeder relay for the faults detected on the MV feeder. In absence of such information, time grading of the HV and MV feeder relays might be used. The HV feeder might be set with higher time multiplier setting such that it trips in a longer duration, with a margin long enough to ensure that the MV feeder relay would have tripped its circuit breaker and the fault would have been isolated if it were on the MV feeder. However, it would be a slow relay for the faults on the HV feeder.

In the fault simulation studies for the relay coordination, the over-current relay pick-up current was heuristically set at 1.25-pu levels for both the MV and HV feeder sections. The trip time was multiplied by 50 ms.

5.4 Simulation Studies and Observations

The system layout described in Chapter 3 was modelled and simulated using the electromagnetic transient (EMT) simulation software PSCAD. Simulation studies were carried out for all the six cases listed in the previous section, and for the different types of faults listed below:

- I. Single line to ground (SLG),
- II. Double line to ground (LLG),
- III. Triple line to ground (LLLG),
- IV. Line-to-line (LL), and
- V. Triple Line (LLL)

Out of these, the triple line to ground (LLLG) fault and triple line (LLL) fault are the symmetrical faults. They would be identical in the cases where the zero sequence components are completely absent.

The studies were carried out with fault resistance of 0.01 pu (1%) and 0.20 pu (20%). The faults were separately applied at the points *FA* on the MV feeder for WTG #4, and at the point *FB* on the HV feeder #2. Since the objective was to demonstrate the relay performance, breaker tripping operation was not simulated.

5.4.1 Single Line to Ground Fault on a MV Feeder

A single line to ground (SLG) fault was applied for 150 ms at *FA* on the MV feeder. The fault current waveforms along with the pick-up and trip of the relays are shown in Figure 5.4. The MV relay picked up (i.e. its internal output is greater than 0.95) at 4ms, and the HV feeder relay picked up at 27ms. In the simulated period of 150 ms, it reached a maximum of 0.308. This implied that it would have tripped in 487 ms, if the fault had been persistent.

The peak fault current was 11.59 pu, while the MV feeder relay observed a peak fault current of 10.55 pu. However, Fourier analysis shows that the fundamental component was only 8.77 pu for the fault current, and 7.93 pu for the current through the MV feeder relay CT. The peak fault current in the HV feeder relay was 3.61 pu, and its fundamental component was 2.39 pu.

A comparison of these fault current with the estimated values is given in Table 5.2. The low value of fundamental component indicates the high harmonic content in the current waveforms.

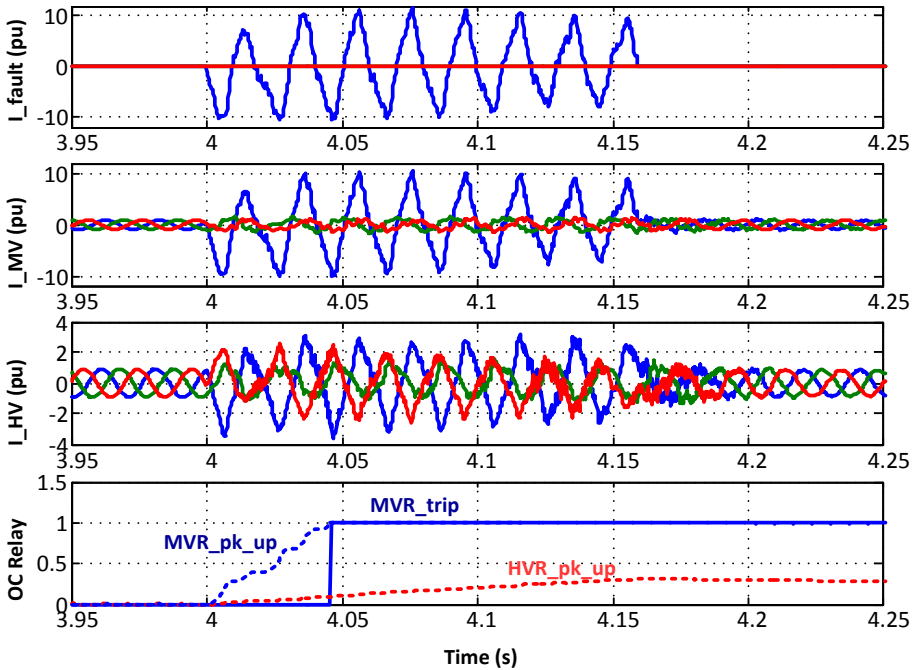


Figure 5.4. Fault current and relay trip signal corresponding to a SLG fault at *FA* for 150 ms.

Table 5.2. Comparison of estimated* and simulated fault currents for LLLG Faults

| | Fault Current | Base (kA, rms) | Estimated (pu) | SLG Fault, Simulated peak (pu) | | LLLG Fault, Simulated peak (pu) | |
|---------------------------------------|---------------|----------------|----------------|--------------------------------|-------------|---------------------------------|-------------|
| | | | | total | fundamental | total | fundamental |
| (SLG Fault at <i>FA</i> on MV Feeder) | Total | 1.80 | 9.0 | 11.59 | 8.77 | 8.4 | 2.56 |
| | MV CT#4 | 1.80 | 6.8 | 10.55 | 7.93 | 6.8 | 2.41 |
| | HV CT#2 | 0.87 | 2.85 | 3.61 | 2.39 | 3.3 | 1.36 |
| (Fault at <i>FB</i> on HV Feeder) | Total | 0.87 | 4.5 | 8.6 | 2.14 | 7.1 | 1.80 |
| | MV CT#4 | 1.80 | 1.1 | 2.1 | 0.52 | 1.9 | 0.11 |
| | HV CT#2 | 0.87 | 3.4 | 7.5 | 1.87 | 6.2 | 1.71 |

* The fault currents were estimated for a symmetric (LLL) fault.

Figure 5.5 shows the HVDC voltage and power oscillations during the SLG fault. The peak voltage is recorded at 1.49 pu, and the minimum power at 0.37 pu during the fault. The power outputs from the four WTGs are shown as well. Even though the fault is on the feeder containing WTG #4, all other WTGs get adversely affected. The system recovered only after the fault had been cleared.

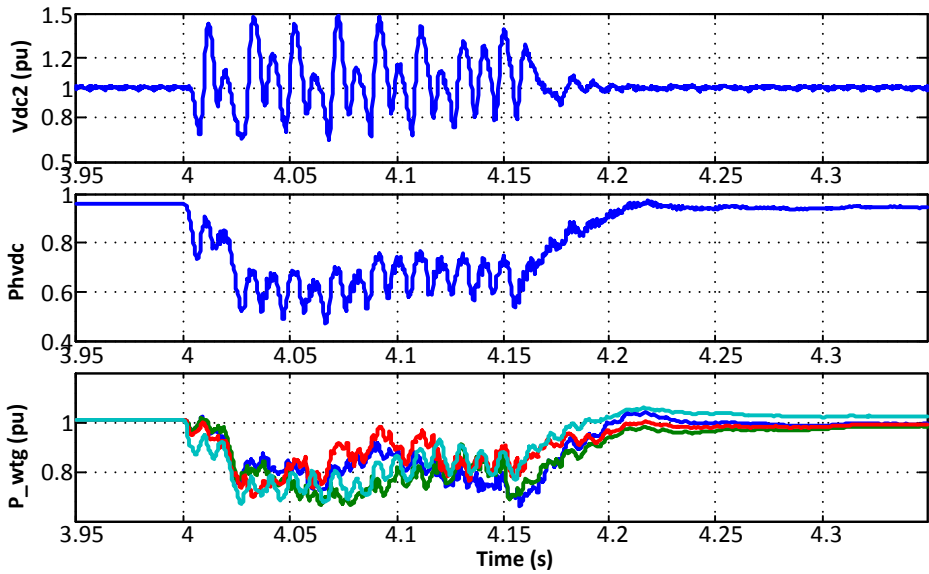


Figure 5.5. HVDC voltage, power and WTG power generation during the SLG fault at *FA*.

5.4.2 Triple Line to Ground Fault on a MV Feeder

The fault current and the current through the MV feeder CT for a three-phase to ground fault at *FA* on the MV feeder #4 are shown in Figure 5.6.

The LLLG fault was applied for 300 ms. The peak fault current was 8.4 pu, while the MV feeder relay observed a peak fault current of 6.8 pu. The peak fault current in the HV feeder relay was 3.3 pu as shown in Figure 5.7. The maximum dc overvoltage was recorded at 1.22 pu, which is much lower than 1.48 pu in the case of SLG fault. The power flow however dropped down to 0. Even the WTG power generation recovery was found to be slower than that in the case of the SLG fault described earlier.

In spite of the high peak currents, the fundamental components were significantly low as shown in Table 5.2. The fundamental component of the fault current was 2.56 pu and the current through the MV feeder relay CT was 2.41 pu. The MV relay picked up (i.e. its internal output was greater than 0.05 units) after 6 ms, and it tripped after 278 ms. The pick-up of HV feeder relay would have taken a very long time (estimated to be 2.8s) to trip.

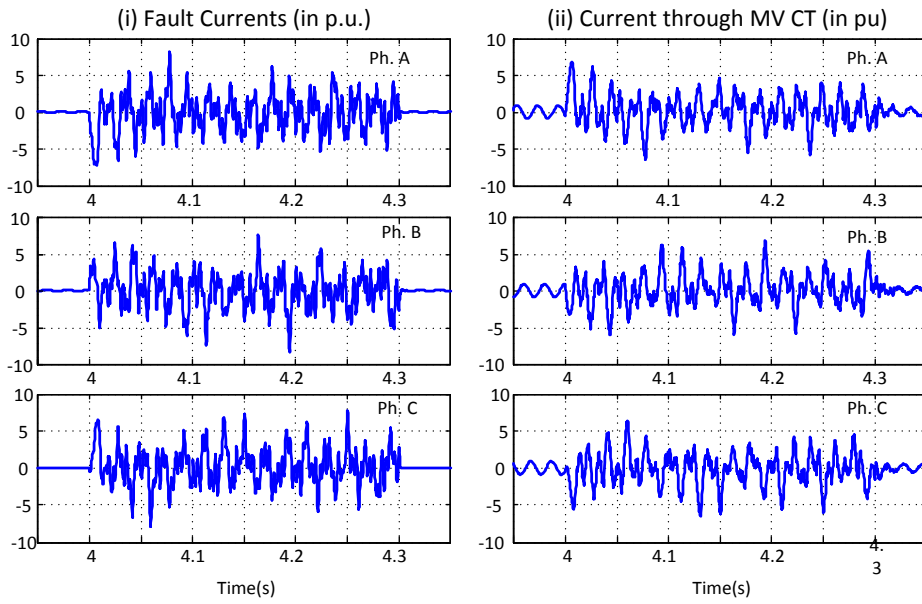


Figure 5.6. LLLG fault at *FA*. (i) Fault currents; (ii) Fault current through the MV CT.

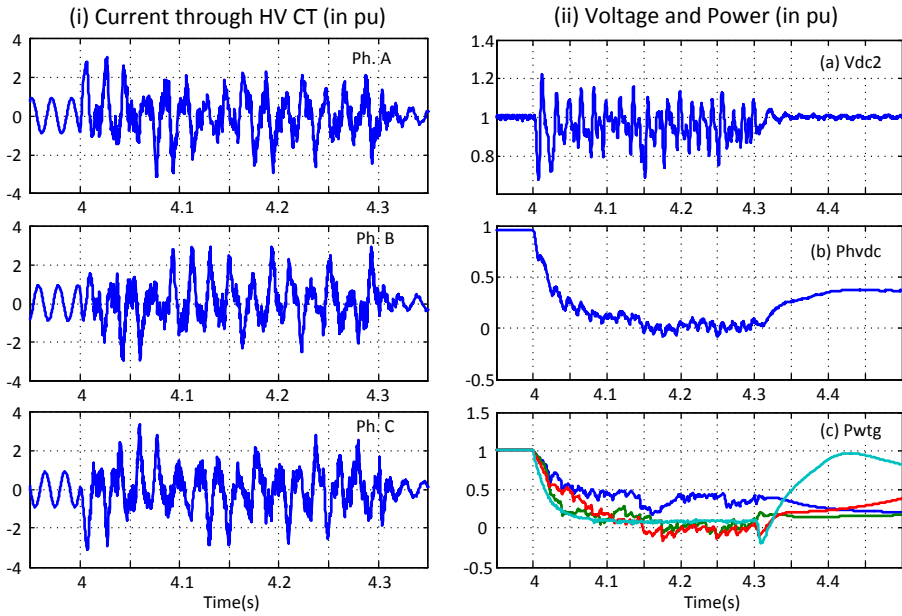


Figure 5.7. LLLG fault at *FA*. (i) Fault currents through the HV CT; (ii) HVDC voltage; power and WTG power generation curves.

5.4.3 SLG and LLLG Faults on a HV Feeder

The fault and CT current waveforms during the SLG fault and the LLLG fault separately applied at *FB* on the HV feeder #2 are shown in Figure 5.8. Their peak amplitudes during the fault and the corresponding fundamental component values have been compiled in Table 5.2.

Even though the peak amplitudes of the fault current were of the order of 8.6 pu for the SLG fault and 7.1 pu for the LLLG fault, the low fundamental component content implied the high amount of harmonic components, which was also obvious from the waveforms in Figure 5.8. The low fundamental component affected the fault detection and the relay trip times were observed as 273 ms, and 343 ms after the fault incidence for the SLG and LLLG faults respectively.

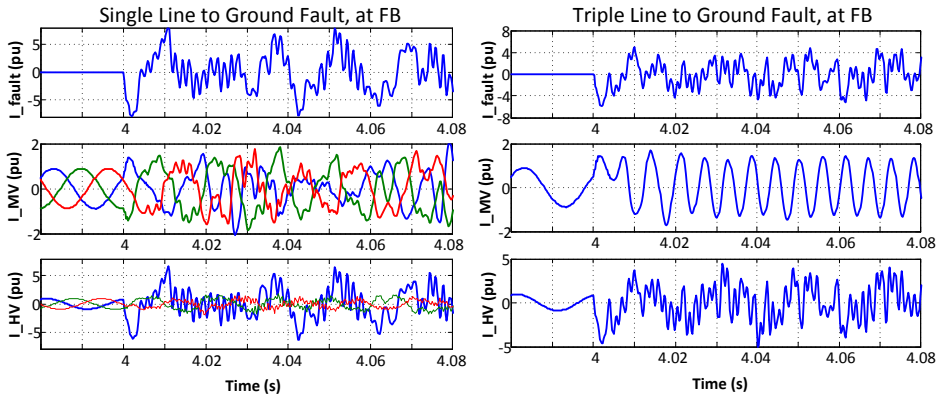


Figure 5.8. Fault and CT current waveforms for the SLG and LLLG faults at *FB*. Only Phase A waveform is shown for the LLLG fault.

5.4.4 Relay Tripping for Different Types of Faults

All different types of faults at *FA* and *FB* were simulated for the different cases. The trip time response of the relays were recorded and plotted as shown in Figure 5.9 for the fault resistance of 1% (i.e. 0.01 pu) and in Figure 5.10 for the fault resistance of 20% (i.e. 0.20 pu). In both the cases, the SLG faults, which are the most common faults in the power system, got detected fastest of all. The timings for the different faults are tabulated in Tables 5.3 and 5.4.

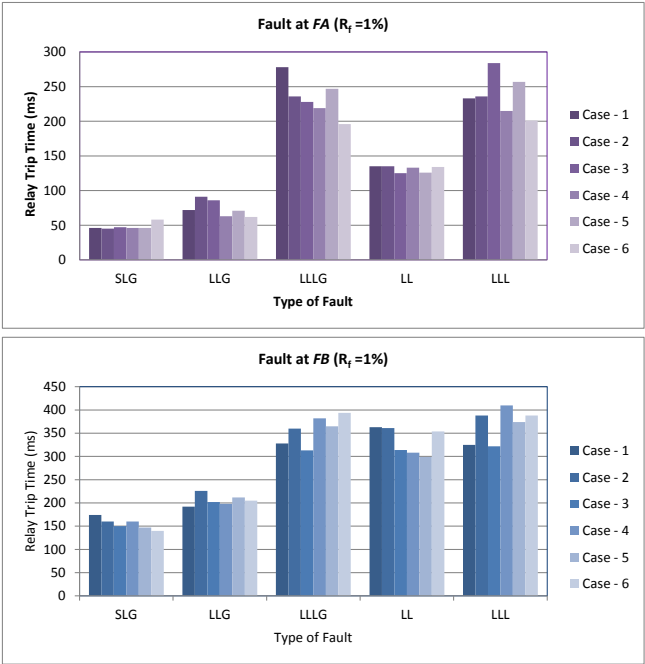


Figure 5.9. Relay trip times for the different faults at *FA* and *FB* in different cases when the fault resistance was 1%.

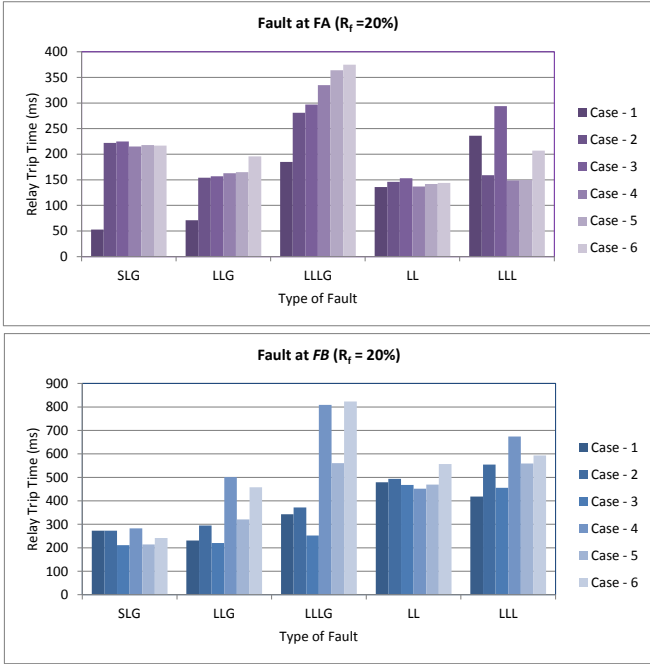


Figure 5.10. Relay trip times for the different faults at *FA* and *FB* in different cases when the fault resistance was 20%.

Table 5.3 Over-current relay trip time (in ms) for different faults in different cases with 1% fault resistance.

| Fault | Relay | Case #1 | Case #2 | Case #3 | Case #4 | Case #5 | Case #6 |
|---|-------|---------|---------|---------|---------|---------|---------|
| SLG | MV | 46 | 45 | 47 | 46 | 46 | 58 |
| | HV | 174 | 160 | 150 | 160 | 147 | 140 |
| LLG | MV | 72 | 91 | 86 | 63 | 71 | 62 |
| | HV | 192 | 226 | 202 | 198 | 212 | 205 |
| LLLG | MV | 278 | 236 | 228 | 219 | 247 | 196 |
| | HV | 328 | 360 | 313 | 382 | 365 | 394 |
| LL | MV | 135 | 135 | 125 | 133 | 126 | 134 |
| | HV | 363 | 361 | 314 | 308 | 299 | 354 |
| LLL | MV | 233 | 236 | 284 | 215 | 257 | 201 |
| | HV | 325 | 388 | 322 | 410 | 374 | 388 |
| HV Relay Over-reach (Times greater than 500 ms are projected values) | | | | | | | |
| SLG | HVx | 467 | 386 | 648 | 397 | 739 | 1134 |
| LL | HVx | 486 | 1250 | 367 | 663 | 666 | 759 |

Table 5.4 Over-current relay trip time (in ms) for different faults in different cases with 20% fault resistance.

| Fault | Relay | Case #1 | Case #2 | Case #3 | Case #4 | Case #5 | Case #6 |
|---|-------|---------|---------|---------|---------|---------|---------|
| SLG | MV | 53 | 222 | 225 | 215 | 218 | 217 |
| | HV | 273 | 273 | 211 | 283 | 214 | 242 |
| LLG | MV | 71 | 154 | 157 | 163 | 165 | 196 |
| | HV | 231 | 295 | 220 | 501 | 321 | 458 |
| LLLG | MV | 185 | 281 | 297 | 335 | 364 | 375 |
| | HV | 343 | 372 | 252 | 809 | 561 | 824 |
| LL | MV | 136 | 146 | 153 | 137 | 142 | 144 |
| | HV | 479 | 494 | 468 | 452 | 469 | 557 |
| LLL | MV | 236 | 159 | 294 | 149 | 150 | 207 |
| | HV | 418 | 554 | 456 | 674 | 559 | 594 |
| HV Relay Over-reach (Times greater than 500 ms are projected values) | | | | | | | |
| SLG | HVx | 467 | x | x | x | x | x |
| LL | HVx | 486 | 1022 | 712 | 929 | 704 | 728 |

Table 5.5 Mean trip time of the over-current relay (in ms) and the corresponding standard deviation as a percentage of mean for the different faults in different cases.

| | Fault at FA, Rf=1% | | Fault at FB, Rf=1% | | Fault at FA, Rf=20% | | Fault at FB, Rf=20% | |
|------|--------------------|----------|--------------------|----------|---------------------|----------|---------------------|----------|
| | Mean (ms) | Std Dev. | Mean | Std Dev. | Mean | Std Dev. | Mean | Std Dev. |
| SLG | 48 | 9% | 155 | 7% | 192 | 32% | 249 | 12% |
| LLG | 74 | 15% | 206 | 5% | 151 | 25% | 338 | 32% |
| LLLG | 234 | 11% | 357 | 8% | 306 | 21% | 527 | 43% |
| LL | 131 | 3% | 333 | 8% | 143 | 4% | 486 | 7% |
| LLL | 238 | 11% | 368 | 9% | 199 | 27% | 543 | 16% |

Table 5.5 shows the mean and the standard deviation of the trip times for the faults in different cases. The low standard deviation indicates that the relay trip times do not vary much in the different cases. Moreover, the trip times are longer in the symmetrical fault cases due to low magnitude of the fundamental component as was observed in the previous cases.

5.4.5 Over-reach of the HV Feeder Relay

Table 5.3 and 5.4 reveal some of the cases when the HV feeder relay tripped unduely. SLG and LL faults are listed here, as these two faults had a strong influence on the HV feeder relay getting excited. When the fault resistance was 0.01 pu, the HV feeder relay tripped within 367 ms for an LL fault in case #3. Though the the over-reach tendency of the HV feeder relay was reduced when the fault resistance was 0.2 pu, it picked up within 467 ms for an SLG fault in case #1.

The tabulated results show the HV feeder relay trip times for the cases when they were tripping within the fault simulation time of 500 ms. For other cases, the internal output of the relay has been projected to estimate the probable trip time of the relay if the fault had been persistent.

Such over-reach of the HV feeder relay can be avoided by changing the relay pick-up current settings or time multiplier settings. However, the relay characteristic will change for all the fault instances. Its speed and sensitivity will decrease if the pick-up current level is increased. If the pick-up current setting is raised, the relay will lose sensitivity to high fault impedance faults, as well as the trip will be delayed for all other faults.

The relay may also be made slower by increasing the time multiplier setting. However, such changes will increase the relay trip time for all the fault cases.

Since modern communication relays are equipped with communication capabilities, the pick-up signal from the relays on the MV feeder can be relayed to block the HV feeder relay, at least for a period of time taken by the MV feeder relay and the circuit breaker to operate. Thus, the latter would be delayed from undue tripping for the faults on the MV feeder which is outside its main zone of protection.

5.5 Discussion and Conclusions

The algebraic addition of the current contribution from all the converters gave an approximate estimate of the fault current levels. Table 5.2 compares the estimated and simulated results. There were significant differences between them. Moreover, the fundamental components of the fault currents were significantly lower than their peak components, due to the presence of harmonics. For instance, in the case of an SLG fault at *FA*, the fundamental components were approximately matching the estimated values, with a maximum error of 17%. The maximum instantaneous values were following the trend, but they were on the higher side by an error of up to 55%.

On the other hand, for the symmetrical LLLG fault case, the maximum instantaneous values were matching with the maximum error being 16%. The fundamental component was much lower as the error varied in the range of 52-72%. Further analysis revealed that the fundamental component of the current from the VSC-HVDC converter was in the range of 0.58 to 0.69 pu against the 1.15 pu as assumed in the simplified calculations. This error itself would introduce an error of about 1 pu in the HV feeder CT and 2 pu in the MV feeder CT as the current bases change.

The comparison was worse for the faults on at *FB* the HV feeder. On one hand, the maximum instantaneous peak values of the fault currents were higher by 91-121% for the SLG fault, and by 58-82% for the LLLG fault. On the other hand the maximum fundamental components were lower by 45-53% for the SLG faults. For the LLLG fault at *FB*, the fundamental component of the fault current and the HV feeder CT current were lower by 60% and 50% respectively, while that of the MV feeder CT was lower by 90%. Moreover, in this case, the fundamental component was very low at only 0.11 pu while the peak was on the higher side at 1.9 pu against the estimated value of 1.1 pu for the MV feeder CT

Such observations indicate the highly non-linear behaviour of the converters in the converter connected grid. The non-linearity resulted from the current limit controls in the VSC-HVDC converters and the saturation of the converters in the WTG-GSC models. Further, the presence of huge amount of capacitance and the inductors at the VSC filters would also aggravate the

situation. The harmonic analysis of the currents during the fault and the role of the VSCs as well as other components were not investigated further.

The results were, thus, very much different from those of the synchronous machines. The latter are typically characterized by the sub-transient and transient time constants, which indicate their response to short circuit conditions. Simulation results, thus, emphasize that conventional fault analysis techniques would not be applicable as the converter current response was very different from those of the rotating machines. Therefore, a detailed EMT simulation analysis with proper representation of the converter PLL and controller dynamics is necessary for the thorough analysis of fault currents and relay co-ordination.

5.6 Summary

This chapter investigates the over-current relay coordination in offshore WPP grid, which is connected to power electronic converters at all the terminals. A simplified numerical approach to estimate the symmetrical fault currents by using the current source representation of the WTG-FSC has been proposed and compared against the results from the EMT simulations. Though some correlation can be drawn between the two, the large differences warrant EMT simulation with the detailed model of the power electronic converter controllers to obtain the actual fault currents under different operating conditions.

The relay coordination in this study was achieved on the basis of nominal current levels as the offshore grid had a radial network topology. The relay trip times were quite long in some cases, which could be improved on the basis of the EMT simulation results. The low standard deviation of the relay trip times in different operating cases indicate the critical role of the VSC-HVDC converter in the relay coordination.

6 Negative Sequence Current Controllers

This chapter presents the use of the power electronic converters to control the injection of negative sequence currents in the offshore grid such that the power oscillations can be minimized. The WTG-FSCs are controlled to inject a constant active power using both the current sequences depending upon the terminal voltage. The VSC-HVDC converters control the negative sequence currents to minimize the power oscillations in the HVDC system, thereby minimizing the dc voltage oscillations.

6.1 Introduction

There are plenty of power electronic voltage source converters (VSCs) in a WPP—right from the FSCs in the WTGs to the VSC-HVDC. The current control capability of these converters can be utilized to control the negative sequence current injection in the offshore WPP grid during the unbalanced operating conditions arising out of asymmetric faults.

Reference [70] presents the control of WTG-GSC during unbalanced grid conditions. Rotating reference frame has been used for the implementation of the current controller. This requires two separate controllers. The need for power reduction during unbalanced grid conditions has been highlighted. Four different control alternatives for the control of grid connected converters under unbalanced voltage conditions have been described in [71]. In these articles, a three phase voltage source has been considered as the grid model which produces sinusoidal waveforms even under unbalanced voltage conditions. The control of the grid side converter (GSC) of a WTG-FSC using the sequence components of currents is presented in [72], [73].

Analysis and control of VSC-HVDC system connecting two power system grids was presented in [45], [74]. Negative sequence currents were injected to achieve the predetermined power flow under the given unbalanced terminal voltage conditions. Both these methods assumed that the power flow was known in advance. However, in a VSC-HVDC connection to the wind power plant, the power level depends upon the prevalent wind conditions, and it is not precisely known beforehand. Hence, the VSC-HVDC terminal is controlled to

maintain the voltage reference like an infinite bus, such that the generated power can be collected [75].

An offshore grid with WTG-FSC units and VSC-HVDC transmission is different from the case when at least one terminal is connected to the conventional grid. Here all the terminals are connected to the VSCs. The VSC-HVDC converter sets up the reference voltage. During faults and unbalanced operating conditions, they themselves may go in current limiting mode. Any injection of the negative sequence current will also affect the offshore grid voltage profile.

This chapter presents a novel method of estimating the negative sequence current injections by the VSC-HVDC to eliminate the power oscillations. Prior information of active power flow is not required in this method. Though the control approach have been described here with reference to the VSC-HVDC with two level converters, it is also applicable to the multi-level converters as their interaction with the grid remains similar as far as current injection control is concerned [41].

6.2 Negative Sequence Controller for the VSC-HVDC

Extraction of positive and negative sequence components from the three phase measurements of the voltage has been described in Chapter 3, Section 3.13. The equations (3.11-3.12) give the positive and negative sequence components of the voltage in the stationary reference frame. These can be converted to the positive and negative sequence components in the rotating reference frame as follows,

$$\begin{aligned} \begin{bmatrix} v_{dp} \\ v_{qp} \end{bmatrix} &= \begin{bmatrix} \cos \omega t & -\sin \omega t \\ \sin \omega t & \cos \omega t \end{bmatrix} \begin{bmatrix} v_{\alpha p} \\ v_{\beta p} \end{bmatrix}, \\ \text{or, } (v_{dp} + jv_{qp}) &= (v_{\alpha p} + jv_{\beta p})e^{-j\omega t} \end{aligned} \quad (6.1)$$

$$\begin{aligned} \begin{bmatrix} v_{dn} \\ v_{qn} \end{bmatrix} &= \frac{1}{2} \begin{bmatrix} 1 & q \\ -q & 1 \end{bmatrix} \begin{bmatrix} v_{\alpha} \\ v_{\beta} \end{bmatrix} \\ \text{or, } (v_{dn} + jv_{qn}) &= (v_{\alpha n} + jv_{\beta n})e^{j\omega t} \end{aligned} \quad (6.2)$$

where, ωt is the phase angle of the positive sequence voltage vector determined by the PLL.

Similarly, the positive and negative sequence current components can be written as,

$$(i_{dp} + ji_{qp}) = (i_{ap} + ji_{\beta p})e^{-j\omega t} \quad (6.3)$$

and,

$$(i_{dn} + ji_{qn}) = (i_{an} + ji_{\beta n})e^{j\omega t} \quad (6.4)$$

Then, in terms of the sequence components of the voltage and the current, the expression for the instantaneous active and reactive power $S = (P + jQ)$ can be written as,

$$S = \frac{3}{2}(v_{an} + jv_{\beta n} + v_{an} + jv_{\beta n})(i_{an} + ji_{\beta n} + i_{an} + ji_{\beta n})' \quad (6.5)$$

Using (6.1) – (6.4) in (6.5), we get, as described in [73] and [74],

$$S = \frac{3}{2} \left((v_{dp} + jv_{qp})e^{j\omega t} + (v_{dn} + jv_{qn})e^{-j\omega t} \right) \left((i_{dp} + ji_{qp})e^{j\omega t} + (i_{dn} + ji_{qn})e^{-j\omega t} \right)'$$

or,
$$S = \frac{3}{2} \left[(v_{dp} + jv_{qp})(i_{dp} - ji_{qp}) + (v_{dn} + jv_{qn})(i_{dn} - ji_{qn}) + (v_{dp} + jv_{qp})(i_{dn} - ji_{qn})e^{j2\omega t} + (v_{dn} + jv_{qn})(i_{dp} - ji_{qp})e^{-j2\omega t} \right] \quad (6.6)$$

Thus, under unbalanced operating conditions when both the positive and negative sequence voltages and currents are present, the expression for the active power, which is the real part of (6.6), comprises of an average power p_{av} , and oscillatory cosine and sine terms (p_{c2} and p_{s2}) as given below,

$$p_{inst} = p_{av} + p_{c2} \cos(2\omega t) + p_{s2} \sin(2\omega t) \quad (6.7)$$

where,

$$p_{av} = \frac{3}{2}(v_{dp}i_{dp} + v_{qp}i_{qp} + v_{dn}i_{dn} + v_{qn}i_{qn})$$

$$p_{c2} = \frac{3}{2}(v_{dn}i_{dp} + v_{qn}i_{qp} + v_{dp}i_{dn} + v_{qp}i_{qn})$$

$$p_{s2} = \frac{3}{2}(v_{qn}i_{dp} - v_{dn}i_{qp} - v_{qp}i_{dn} + v_{dp}i_{qn})$$

Power oscillations can be eliminated if the coefficients of both of the oscillatory terms p_{c2} and p_{s2} are equated to 0, as follows:

$$\begin{bmatrix} p_{c2} \\ p_{s2} \end{bmatrix} = \begin{bmatrix} 0 \\ 0 \end{bmatrix} = \begin{bmatrix} v_{dn} & v_{qn} & v_{dp} & v_{qp} \\ v_{qn} & -v_{dn} & -v_{qp} & v_{dp} \end{bmatrix} \begin{bmatrix} i_{dp} \\ i_{qp} \\ i_{dn} \\ i_{qn} \end{bmatrix} \quad (6.8)$$

Equation (6.8) gives the values of negative sequence current components (i_{dn}, i_{qn}) in terms of the positive and negative sequence components of the voltage at the filter bus and the positive sequence component of the current in the phase reactors of the offshore VSC-HVDC. Thus, the references, (i_{dn}^*, i_{qn}^*) for the negative sequence current components can be calculated using (6.8) and are given by,

$$\begin{bmatrix} i_{dn}^* \\ i_{qn}^* \end{bmatrix} = - \begin{bmatrix} v_{dp} & v_{qp} \\ -v_{qp} & v_{dp} \end{bmatrix}^{-1} \begin{bmatrix} v_{dn} & v_{qn} \\ v_{qn} & -v_{dn} \end{bmatrix} \begin{bmatrix} i_{dp} \\ i_{qp} \end{bmatrix}$$

Or,

$$\begin{bmatrix} i_{dn}^* \\ i_{qn}^* \end{bmatrix} = \frac{-1}{v_{dp}^2 + v_{qp}^2} \begin{bmatrix} (v_{dp}v_{dn} + v_{dp}v_{dn}) & (v_{dp}v_{qn} + v_{qp}v_{dn}) \\ (v_{qp}v_{dn} + v_{dp}v_{dn}) & -(v_{dp}v_{dn} + v_{dp}v_{dn}) \end{bmatrix} \begin{bmatrix} i_{dp} \\ i_{qp} \end{bmatrix} \quad (6.9)$$

Thus, the active and reactive power references are not required in this formulation. It is an advantage as the offshore VSC-HVDC does not have information about instantaneous active and reactive power at the point of common coupling (PCC). This converter is merely controlled to maintain the positive sequence voltage at the specified nominal value at the PCC, under normal operating conditions, irrespective of the power-flow levels.

Moreover, it is obvious from (6.9) that the negative sequence current references are 0 under balanced operating conditions, when there are no negative sequence voltage components in the offshore grid voltage.

When the negative sequence controllers are enabled, the negative sequence current references are generated as per (6.9). A separate negative sequence current control loop is written (in the rotating reference frame) as follows,

$$v_{dn}^* = -i_{dn}R_{pr} - \omega L_{pr}i_{qn} - k_{p4n}(i_d^* - i_d) - k_{i4n} \int (i_{dn}^* - i_{dn}) \quad (6.10)$$

$$v_{qn}^* = -i_{qn}R_{pr} + \omega L_{pr}i_{qn} - k_{p4n}(i_q^* - i_q) - k_{i4n} \int (i_{qn}^* - i_{qn}) \quad (6.11)$$

The terms for the voltage drop across phase reactor ($-\omega L_{pr}$) are negative in (6.10)–(6.11) as compared to those in (3.20)–(3.21) for the positive sequence current control. This is due to the fact that negative angle ($-\omega t$) is used in the Park's transformation and the negative sequence current has apparently negative frequency. The phase angle (ωt) is the one obtained from the positive sequence PLL.

Separate current controller loops are employed for the positive and negative sequence current control in the rotating reference frame (dq - axes) used for the VSC-HVDC converter control as shown in Figure 6.1. The positive sequence controller is essentially the same as the one in Figure 3.16, as only positive sequence is being controlled in the normal operating mode. When the negative sequence controller is enabled, the negative sequence current references are generated, and they are added to the positive sequence current references. The positive and negative sequence voltage references for the converter cannot be added directly as the two reference frames are rotating in opposite directions. Hence, the two sets of voltage references are converted into the phase variables by using inverse Park's transformation and then added together.

6.3 Negative Sequence Controller for the WTG-GSC

It was described in Chapter 3, Section 3.12 that the WTG-GSC regulates the dc link voltage of the WTG-FSC. Such a voltage regulation controller gives a reference active power to be evacuated by the WTG-GSC. The reactive power reference Q_{av} may be provided by a reactive power controller or specified externally. In this study, the reactive power is assumed to be 0. For the evacuation of the active power, P_{av} under unbalanced operating voltage conditions the positive and negative sequence current references, $i_{\alpha p}^*$, $i_{\beta p}^*$, $i_{\alpha n}^*$, and $i_{\beta n}^*$ in the $\alpha\beta$ -axes are given by [77],

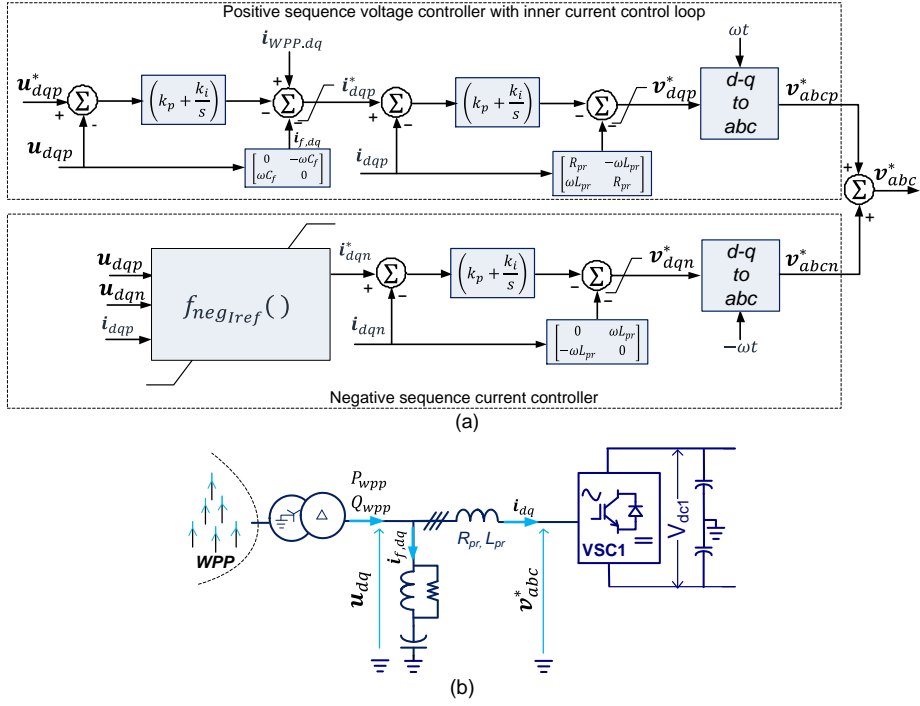


Figure 6.1. Offshore VSC-HVDC controller with negative sequence current (a) Controller block diagram; (b) Schematic.

$$i_{\alpha p}^* + ji_{\beta p}^* = \left(\frac{v_{\alpha p} + jv_{\beta p}}{v_{\alpha p}^2 + v_{\beta p}^2 - v_{\alpha n}^2 - v_{\beta n}^2} \right) P_{av} \quad (6.12)$$

$$i_{\alpha n}^* + ji_{\beta n}^* = - \left(\frac{v_{\alpha n} + jv_{\beta n}}{v_{\alpha p}^2 + v_{\beta p}^2 - v_{\alpha n}^2 - v_{\beta n}^2} \right) P_{av} \quad (6.13)$$

where, $(v_{\alpha p}, v_{\beta p})$ and $(v_{\alpha n}, v_{\beta n})$ are the positive and negative sequence components of the voltage measured at the WTG terminals.

The overall current references are given by:

$$i_{\alpha}^* = i_{\alpha p}^* + i_{\alpha n}^* \quad (6.14)$$

$$i_{\beta}^* = i_{\beta p}^* + i_{\beta n}^* \quad (6.15)$$

The denominator in (6.12) and (6.13) is the difference between the squared magnitudes of the positive and negative sequence voltages. During a fault, the positive sequence voltage tends to decrease while there is significant amount of negative sequence voltage. Thus, the denominator may be very small; thereby

leading to large amplitudes of the current references. Therefore, it is proposed that the negative sequence current controller (NSCC) in the WTG-GSC be disabled when there is a high proportion of negative sequence component in the WTG terminal voltage. In this study, the NSCC is blocked when the proportion of the negative sequence voltage component is higher than 70% of the positive sequence voltage component, and only positive sequence current control is applied for the evacuation of the active power, P_{av} . Under such circumstances, the negative sequence voltage components ($v_{\alpha n}$, $v_{\beta n}$) are substituted by $(0, 0)$ in (6.12) and (6.13) and hence only positive sequence current references are generated. The modified equations are given below:

$$i_{\alpha p}^* + ji_{\beta p}^* = \left(\frac{v_{\alpha p} + jv_{\beta p}}{v_{\alpha p}^2 + v_{\beta p}^2} \right) P_{av} \quad (6.16)$$

$$i_{\alpha n}^* + ji_{\beta n}^* = 0 \quad (6.17)$$

It should be noted here that (6.16) and (6.17) replace (6.12) and (6.13) only for the duration while the NSCC is blocked due to high proportion of the negative sequence components ($v_{\alpha n}$, $v_{\beta n}$) in the terminal voltage as described above. With this replacement, (6.14) and (6.15) are used to get the overall current references.

6.4 Simulation Results

The effect of negative sequence current control strategy was studied through simulation of faults in the offshore grid. Faults were applied for 150 ms and the performance of the negative sequence controller in reducing the dc bus voltage overshoot on the HVDC lines was observed. First, single line to ground (SLG) faults at *FA* and *FB* were studied in detail. Afterwards, other types of faults at these two locations were studied.

Since the negative sequence controllers could be applied in the WTG-GSCs and the offshore VSC-HVDC controllers, there were four combinations as given below:

1. Negative sequence controller was enabled in both the WTG-GSC and the offshore VSC-HVDC (*WIHI*)
2. Negative sequence controller was enabled only in the WTG-GSC

(*W1H0*).

3. Negative sequence controller was enabled only in the VSC-HVDC (*W0H1*).
4. All the negative sequence controllers are disabled (*W0H0*).

6.4.1 Single Line to Ground Fault at 'FA'

Figure 6.2 shows the effect of the negative sequence current controllers on the dc over voltage in the VSC-HVDC transmission system.

The peak DC line voltage overshoot was reduced to 1.15 pu for the case *W1H1*, while it was 1.46 pu, 1.22 pu, and 1.52 pu for the cases *W1H0*, *W0H1*, and *W0H0* respectively.

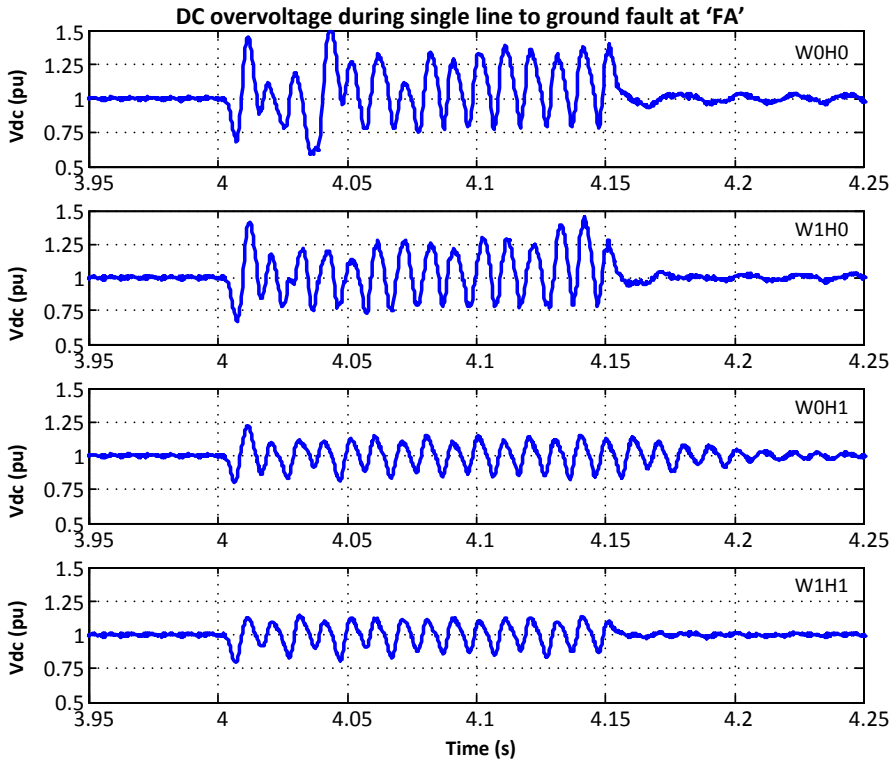


Figure 6.2 DC link voltage over-shoot in the VSC-HVDC system for SLG fault at *FA* for the cases: *W0H0*, *W1H0*, *W0H1*, and *W1H1*.

The effect of these controllers on the power-flow to the HVDC system is shown in Figure 6.3. The power flow was less oscillatory when the NSCCs

were enabled. However, it was observed that the average power transferred to the VSC-HVDC during the fault was higher in *WOH1* than that in *WIH1*. The reason is that the WTG-GSCs went into current limit control mode, and the current references given by NSCC were scaled down, thereby limiting the output power during the fault.

The excess power which could not be evacuated to the VSC-HVDC would have to be dissipated in the WTG-FSC chopper resistors. Power and voltage oscillations were higher and the damping was poor when the NSCCs in the WTG-GSCs were disabled.

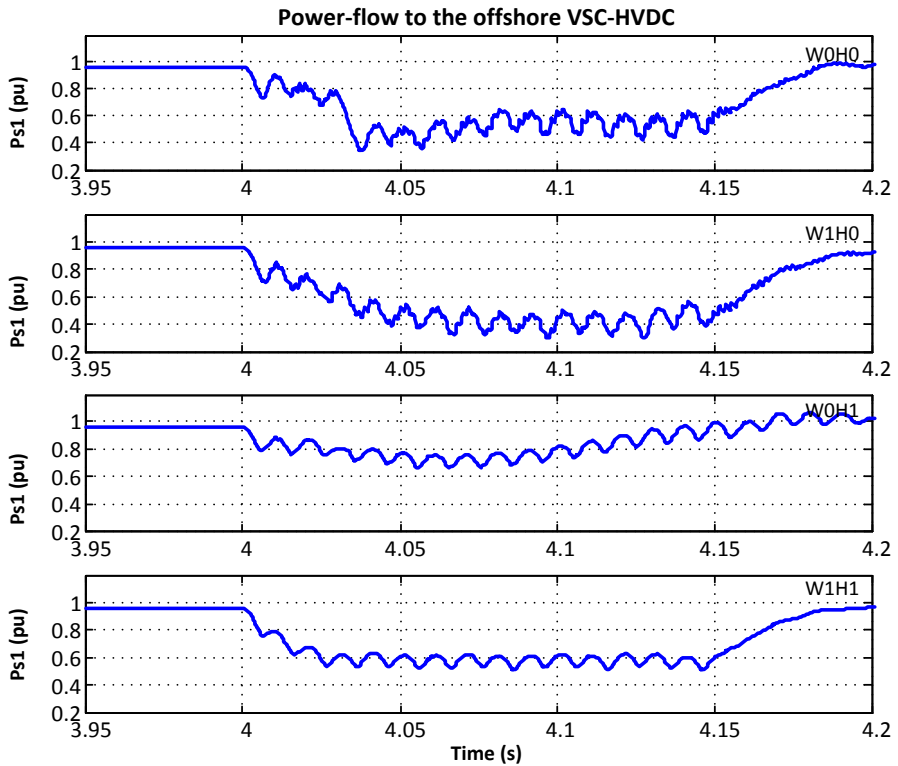


Figure 6.3. Power flow to the offshore VSC-HVDC terminal during the SLG fault at *FA* for the cases: *WOH0*, *WIH0*, *WOH1*, and *WIH1*.

Figure 6.4 shows the three-phase voltage waveforms at the filter bus of the offshore VSC-HVDC for the four cases during the SLG fault at *FA*. A comparison of the cases *WIH1* and *WOH1* against *WIH0* and *WOH0* reveals that the NSCC on the VSC-HVDC was more effective in reducing the high

frequency oscillations in the voltage waveforms. Enabling the NSCC on the WTG-GSC had a small impact in reducing these oscillations. It was justified as the VSC-HVDC was the largest converter in the offshore grid and voltage was measured closer to this converter. The transient peak ac voltage was reduced to 1.35 pu for the case *WIH1* from 2.49 pu for the case *W0H0*. A comprehensive summary of the peak dc voltage overshoot, the minimum power-flow and the ac voltage transient peaks is presented in Table 6.1.

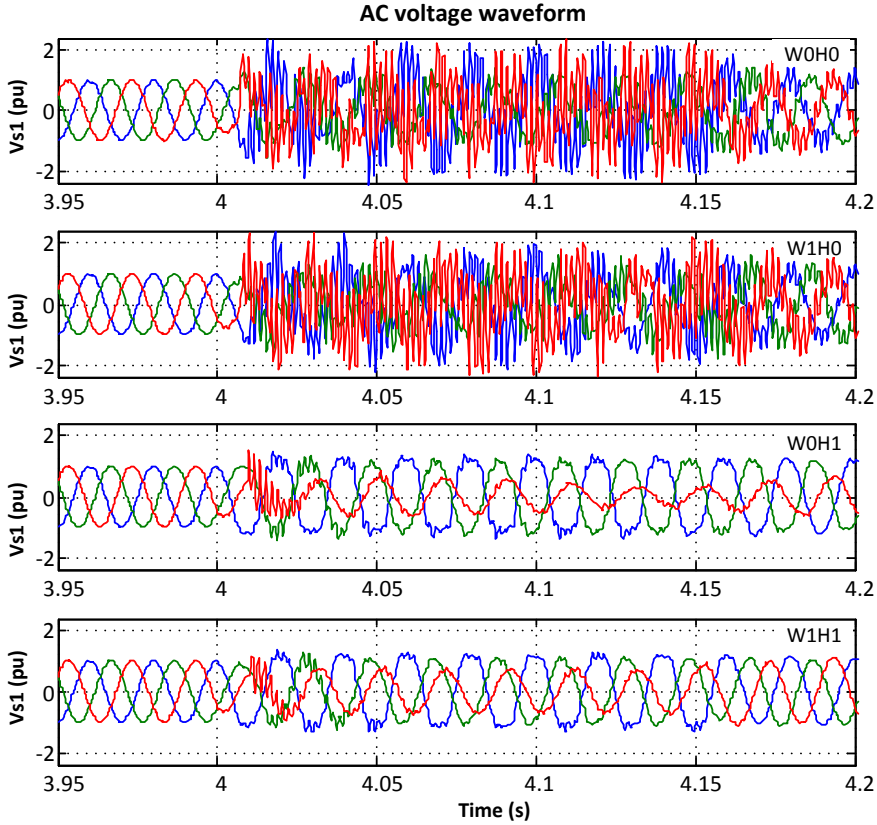


Figure 6.4. Grid voltage at the offshore VSC-HVDC terminal during the SLG fault at *FA* for the cases: *W0H0*, *W1H0*, *W0H1* and *W1H1*.

The power oscillations could not be eliminated as anticipated by (6.8)-(6.9) as the actual negative current flow could not be controlled to the estimated reference levels as shown in Figure 6.5. It happened so as the required ac voltage output was too high for the VSC-HVDC converter.

Table 6.1. Effect of NSCC on the peak values of voltages, currents and power flow during SLG fault at *FA*

| Case | W1H1 | | W1H0 | | W0H1 | | W0H0 | |
|-------------------------------------|-------|------|-------|------|-------|------|-------|------|
| | Min | Max | Min | Max | Min | Max | Min | Max |
| DC line voltage V_{DC} | 0.79 | 1.15 | 0.67 | 1.46 | 0.80 | 1.22 | 0.59 | 1.52 |
| Power-flow to VSC-HVDC | 0.51 | 0.97 | 0.30 | 0.97 | 0.66 | 1.07 | 0.34 | 0.99 |
| AC voltage (at HVDC filters), Ph. A | -1.31 | 1.35 | -2.20 | 2.36 | -1.42 | 1.46 | -2.49 | 2.37 |
| AC voltage (at HVDC filters), Ph. B | -1.26 | 1.29 | -1.75 | 1.63 | -1.47 | 1.35 | -1.61 | 1.46 |
| AC voltage (at HVDC filters), Ph. C | -1.14 | 1.14 | -2.37 | 2.32 | -1.01 | 1.49 | -2.40 | 2.40 |
| Neg. Seq. d -axis current | -0.15 | 0.52 | -0.08 | 0.78 | 0.00 | 0.59 | -0.05 | 0.83 |
| Neg. Seq. q -axis current | -0.28 | 0.30 | -0.04 | 0.21 | -0.36 | 0.06 | -0.48 | 0.22 |

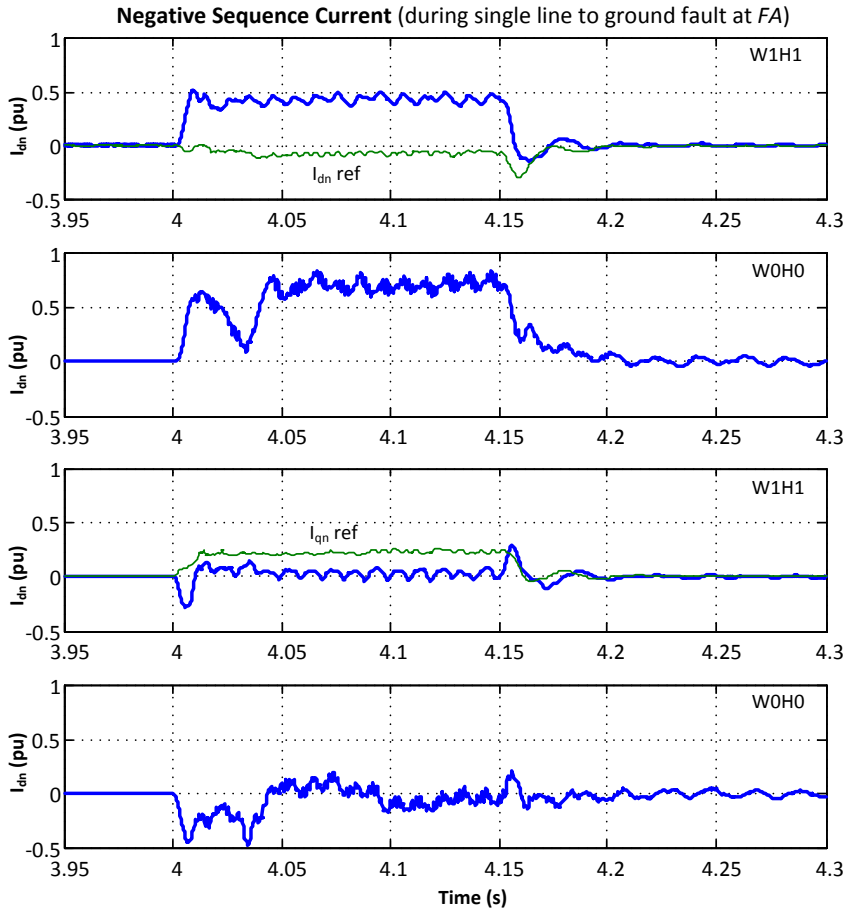


Figure 6.5. Negative sequence d and q axes currents during the SLG fault at *FA* for the cases: *W1H1* and *W0H0*.

Figure 6.5 shows the negative sequence current flows during the SLG fault at *FA* in the cases *W1H1* and *W0H0*.

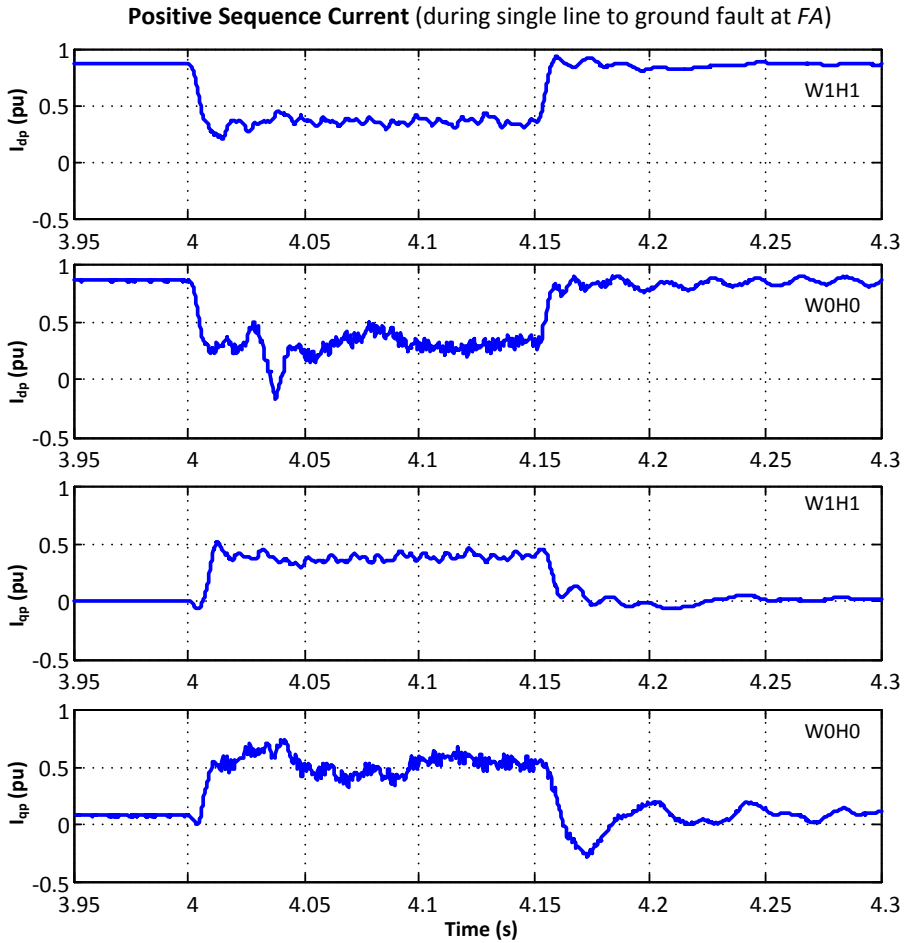


Figure 6.6. Positive sequence d and q axes currents during the SLG fault at FA for the cases: *W1H1* and *W0H0*.

NSCC brought down the d -axis negative sequence current to a level less than 0.52 pu compared to 0.83 pu when it was disabled. Although the NSCC had only a small impact on the q -axis negative sequence current, it showed less oscillation during the fault and during post fault recovery. Without the NSCC, the negative oscillations continued for some time even after the fault had been cleared.

Though the same positive sequence controllers were used in both cases, enabling the negative sequence components led to a reduced level of oscillations in the positive sequence current as shown in Figure 6.6. This signified an overall improvement in the system performance.

When the NSCCs were enabled, positive and negative sequence components of the filter bus voltages were less oscillatory; even though the magnitude of the negative sequence voltage components increased (Figure 6.7). The positive sequence voltage on the d -axis reached a minimum of 0.83 pu in case of *W1H1* while it fell down to 0.52 pu in *W0H0*. Similarly, the positive sequence q -axis voltage was limited within a range of -0.08 pu and 0.15 pu in the case of *W1H1*; while it varied between -0.39 and 0.48 pu in the case of *W0H0*.

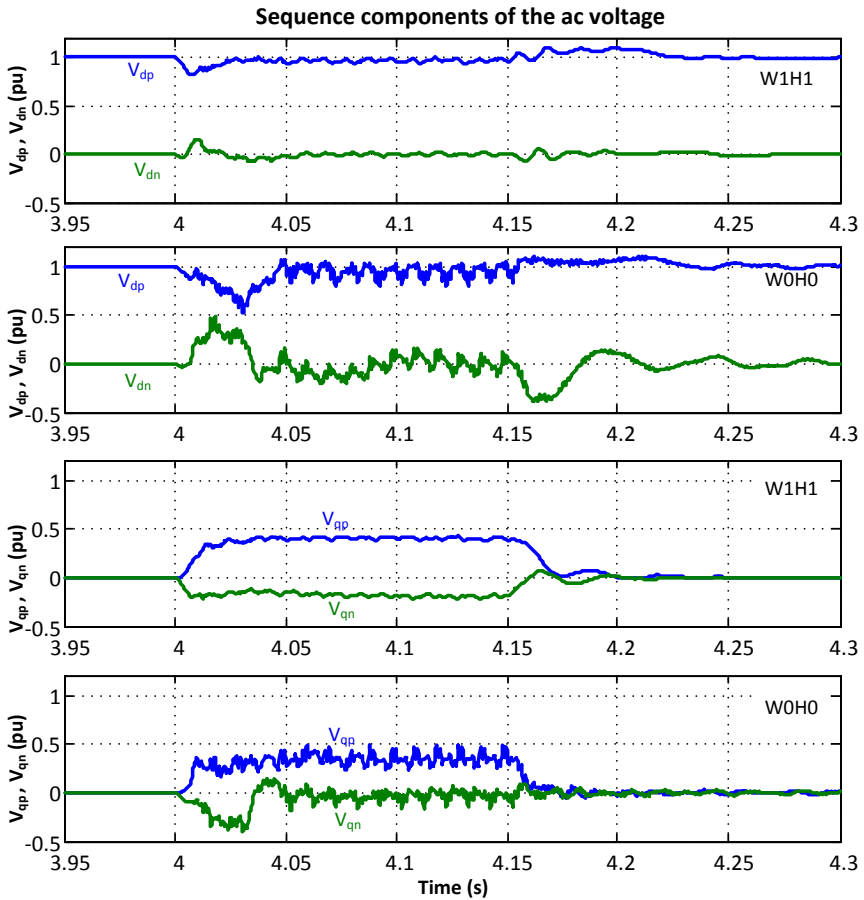


Figure 6.7. Positive and negative sequence d- and q axes voltage components for the SLG fault at FA for the cases: *W1H1* and *W0H0*.

6.4.2 LLG, LLLG and LL Faults at 'FA'

The dc voltage overshoots for the different fault cases, namely LLG, LLLG and LL faults at the point *FA* are shown in Figure 6.8. The NSCCs were most effective during an LL fault as the peak dc voltage overshoot was restricted to 1.20 pu in *W1H1* as compared to 1.31 pu in *W0H0*. For all other faults, there was no significant improvement in minimizing the dc over-voltage. Nevertheless, the over-voltages were observed to be lower than the one which appeared in the case of SLG fault described earlier. During the LLG fault, the dc voltage overshoot increased from 1.12 pu to 1.17 pu. During the LLLG fault, the dc voltage overshoot was 1.19 pu in *W1H1* against 1.22 pu in *W0H0*. Still, there was an overall reduction in peak-to-peak oscillation levels as the minimum dc voltage was higher in *W1H1*. The NSCCs were not expected to have any significant effect during the LLLG fault because of its symmetric fault characteristic. It was studied just to confirm that the NSCCs did not deteriorate the fault.

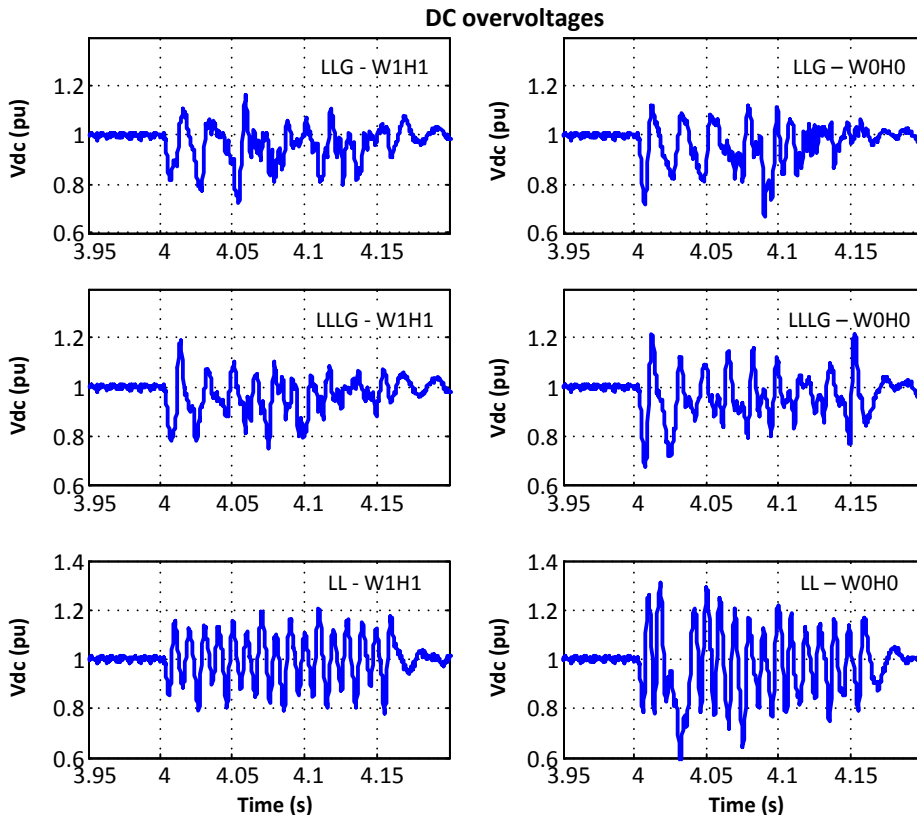


Figure 6.8. DC voltage overshoots in the VSC-HVDC lines for different faults at *FA* for the cases: *W1H1* and *W0H0*.

Figure 6.9 shows the power flow to the offshore VSC-HVDC terminal during the different faults in the offshore collector grid at *FA*. In the case of LL fault, there was some improvement in power-flow as the minimum power-flow level was 0.44 pu in *W1H1*, which was remarkably high in comparison to the minimum power-flow level of 0.08 pu in *W0H0*. However, there was only a small change in power-flow level during the LLG and LLLG faults.

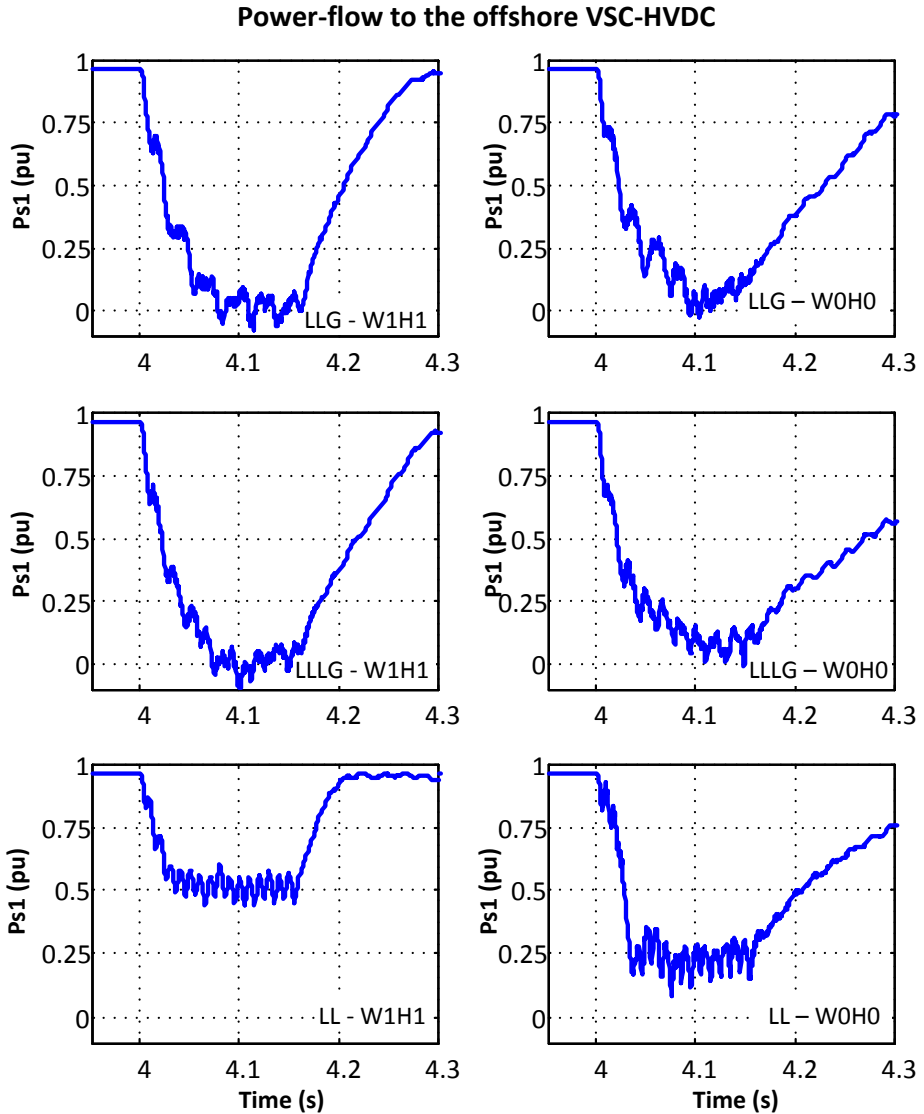


Figure 6.9. Power flow to the offshore VSC-HVDC terminal during different faults at *FA* for the cases: *WIH1* and *WOH0*.

Table 6.2. Effect of NSCC on the Peak Values of dc Voltage Overshoot and Power-flow During Different Faults

| Parameter | Case | SLG | | LLG | | LLL | | LL | |
|-------------------------------|------|------|------|-------|------|-------|------|------|------|
| | | Min | Max | Min | Max | Min | Max | Min | Max |
| Fault at FA | | | | | | | | | |
| DC line voltage (p.u.) | W1H1 | 0.79 | 1.15 | 0.73 | 1.17 | 0.75 | 1.19 | 0.79 | 1.15 |
| | W0H0 | 0.59 | 1.52 | 0.66 | 1.12 | 0.67 | 1.22 | 0.59 | 1.31 |
| Power-flow to VSC-HVDC (p.u.) | W1H1 | 0.51 | 0.97 | −0.08 | 0.96 | −0.09 | 0.96 | 0.51 | 0.97 |
| | W0H0 | 0.34 | 0.99 | −0.03 | 0.96 | −0.01 | 0.96 | 0.08 | 0.96 |
| Fault at FB | | | | | | | | | |
| DC line voltage (p.u.) | W1H1 | 0.75 | 1.28 | 0.64 | 1.12 | 0.68 | 1.10 | 0.75 | 1.28 |
| | W0H0 | 0.68 | 1.34 | 0.74 | 1.09 | 0.69 | 1.06 | 0.70 | 1.39 |
| Power-flow to VSC-HVDC (p.u.) | W1H1 | 0.46 | 1.02 | −0.11 | 0.97 | −0.11 | 0.97 | 0.46 | 1.02 |
| | W0H0 | 0.19 | 0.97 | −0.13 | 0.97 | −0.09 | 0.97 | 0.28 | 0.96 |

Table 6.2 gives a summary of the minimum and maximum values of the dc voltage and power flow to the VSC-HVDC during the different types of faults at *FA*.

6.4.3 Faults at *FB*

The effect of the NSCCs was studied for the different faults on the HV cable feeder at *FB* (Figure 3.1) in the offshore grid, close to the converter transformer terminal. Soon after the fault event, the NSCCs in WTG-GSCs got blocked as described in Section 6.3. Hence, only the positive sequence currents were injected in this case (similar to *WOH1*).

Figure 6.10 shows that, during the SLG fault, the dc voltage overshoot reduced to 1.28 pu in *WIH1* from 1.34 pu in *WOH0*. Similarly, during the LL fault, it reduced to 1.24 pu in *WIH1* from 1.39 pu in *WOH0*. As the NSCCs in the WTG-GSCs got de-blocked after fault clearance, the post fault oscillations were lower in *WIH1* than in *WOH0*.

Besides, there was a marked improvement in power-flow to the VSC-HVDC terminal (Figure 6.11). During the SLG and LL faults, the minimum power-flow level increased to 0.46 pu and 0.54 pu respectively in *WIH1* from 0.19 pu and 0.28 pu respectively in *WOH0*. Although, the case *WIH1* was somewhat oscillatory during the fault, the NSCCs contributed to better

damping of post fault oscillations—these oscillations were lower in the case *W1H1* than in the case *W0H0*.

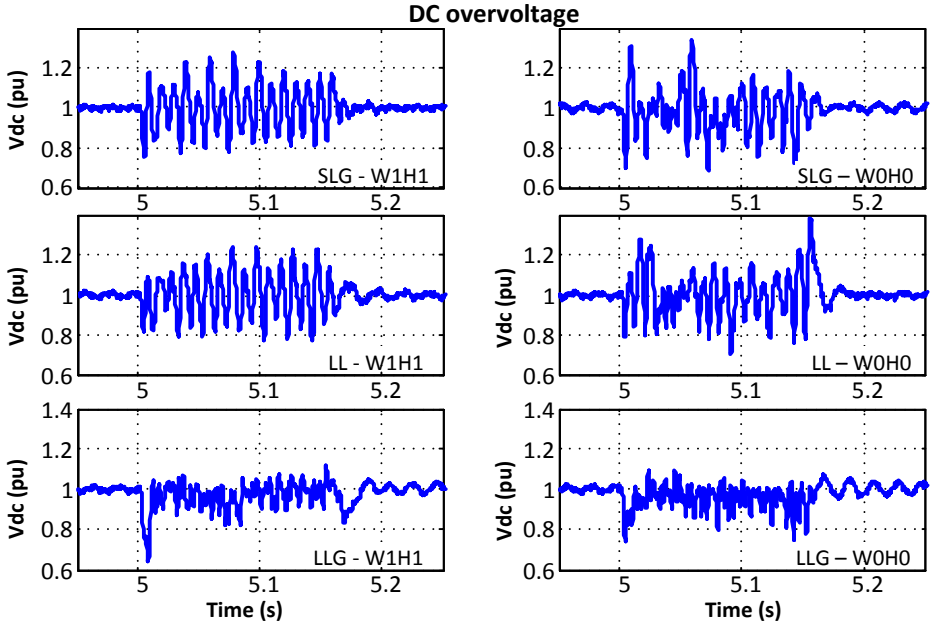


Figure 6.10. DC link voltage over-shoot in the VSC-HVDC system during the SLG, LL and LLG faults at *FB* for the cases: *W1H1* and *W0H0*.

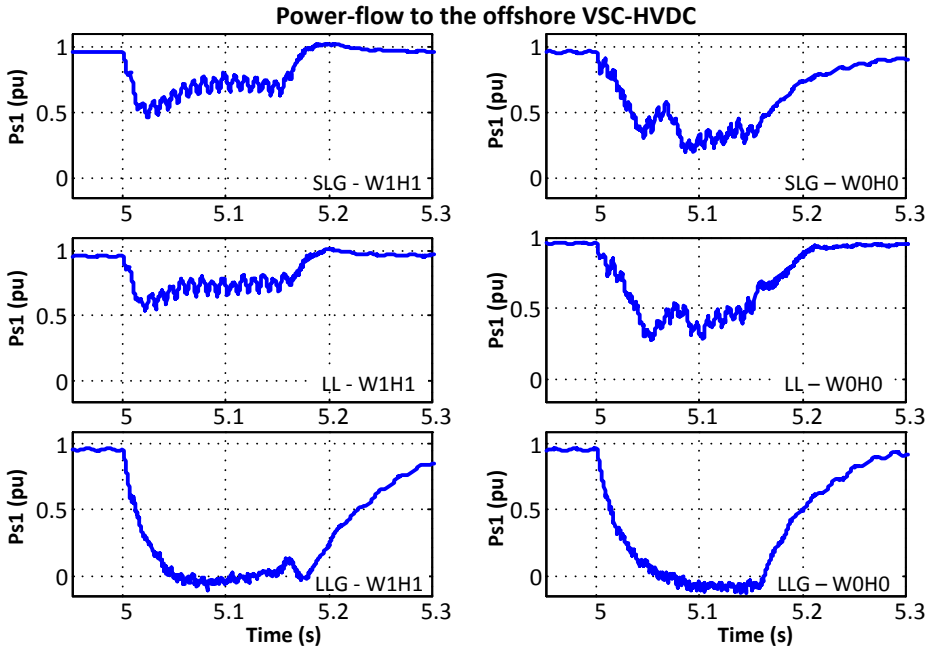


Figure 6.11. Power flow to the offshore VSC-HVDC terminal during the SLG, LL and LLG faults at *FB* for the cases: *W1H1* and *W0H0*.

Figure 6.12 shows the ac voltage waveforms at the VSC-HVDC filter bus during the SLG and LL faults at *FB* for the two cases *W1H1* and *W0H0*. By allowing the negative sequence current control, the converter generated the unbalanced ac voltage waveform with a low harmonic content. The ac current was unbalanced, but it allowed the flow of power transfer. When the NSCC was disabled, a lot of harmonics were generated as the converter attempted to maintain a balanced sinusoidal voltage profile in the network with asymmetrical fault.

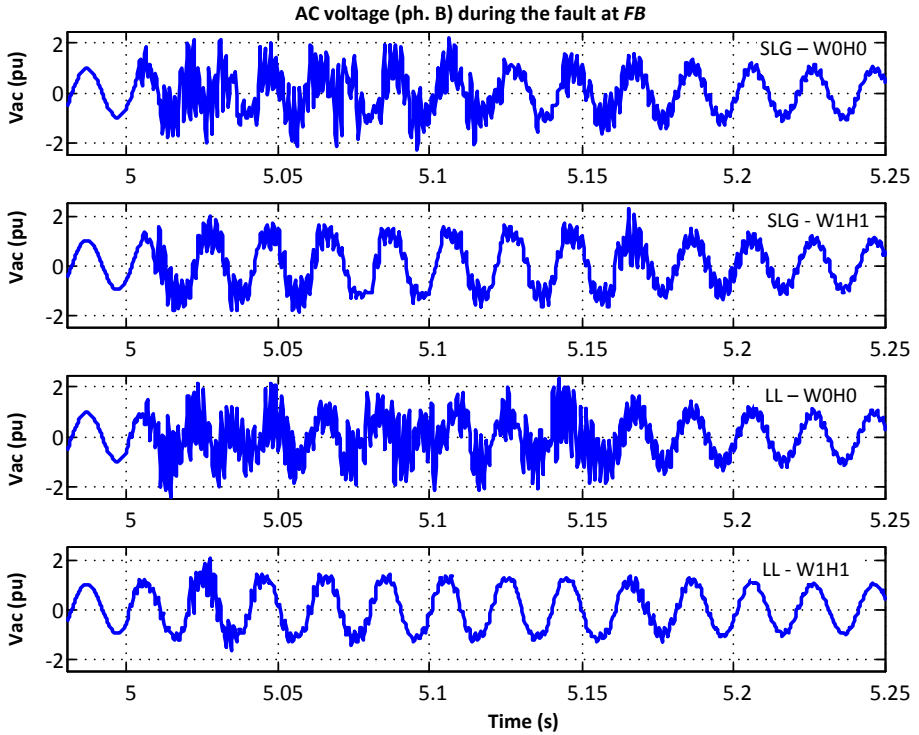


Figure 6.12. Filter bus voltage of the offshore VSC-HVDC terminal during the SLG and LL faults at *FB*.

6.5 Discussion

The simulation results show that maximum over-voltages appear during the SLG and LL faults. Incidentally, the proposed NSCC method (*W1H1*) was most effective in reducing the dc voltage oscillations in these very faults. Moreover, SLG fault is the most common fault of all the faults in a typical power system. When the faults were applied at *FB*, the reduction in dc over-voltage was less in comparison to the reduction observed during the faults at *FA*. Nonetheless, in case of SLG fault at *FB*, it was accompanied by a marked increase in the power-flow during the fault event.

One of the objectives of using the NSCC in the WTG-GSC was to eliminate the power oscillations, and hence the voltage oscillations, in the dc link of the WTG-FSC. However, this study focused on the impact of NSCC on the dc voltage overshoot in the VSC-HVDC and the over-all power-flow.

Enabling the NSCC in WTG-GSC decreased the average power-flow as observed by the comparison of power-flow in the cases *WIH1* and *WIH0* against *WOH1* and *WOH0* (Figure 6.3). It happened so due to the fact that the overall current references demanded by the NSCC as per (6.12)-(6.13) exceeded the maximum current limit of the WTG-GSC (which was assumed as 1.1 pu on its own base); and therefore, they went into current limit mode.

For the SLG and LL faults at *FB*, the NSCCs in the WTG-GSCs got blocked soon after the fault inception due to high proportion of the negative sequence component in the WTG terminal voltage. Consequently, the power transfer was higher, but it was accompanied with relatively higher dc voltage oscillations in the VSC-HVDC system.

Besides when the positive and negative sequence current references are generated as per (6.12) and (6.13) or (6.16) and (6.17), the WTG-GSC cannot control the reactive power. A different strategy might be used such that the WTG-GSC may control active and reactive power injection using positive sequence current control under normal operating conditions. The NSCCs may be enabled only during faults and other unbalanced operating conditions.

Although the NSCC was effective in reducing the dc voltage oscillations, at least during the SLG and LL faults, the power oscillations were not completely eliminated as expected. There was a persistent error between the negative sequence current reference and the actual negative sequence currents as shown in Figure 6.5. Physical limits of the VSC-HVDC terminal, due to nominal dc voltage ratings, limited the maximum ac voltage that could be generated by a voltage source converter. During the SLG fault at *FA*, the peak amplitude of the converter reference voltage for phase *A* was 1.57 pu (i.e. ± 217.9 kV) as shown in Figure 6.2. It would be impossible to achieve when the nominal dc pole-pole voltage of VSC-HVDC was only 1.08 pu (i.e. ± 150 kV). In reality, the dc pole voltage itself was going through transients. Similarly, during the SLG fault at *FB*, the peak amplitude of the converter reference voltages for phase *B* was 1.91 pu (i.e. ± 265.8 kV) as shown in Figure 6.14.

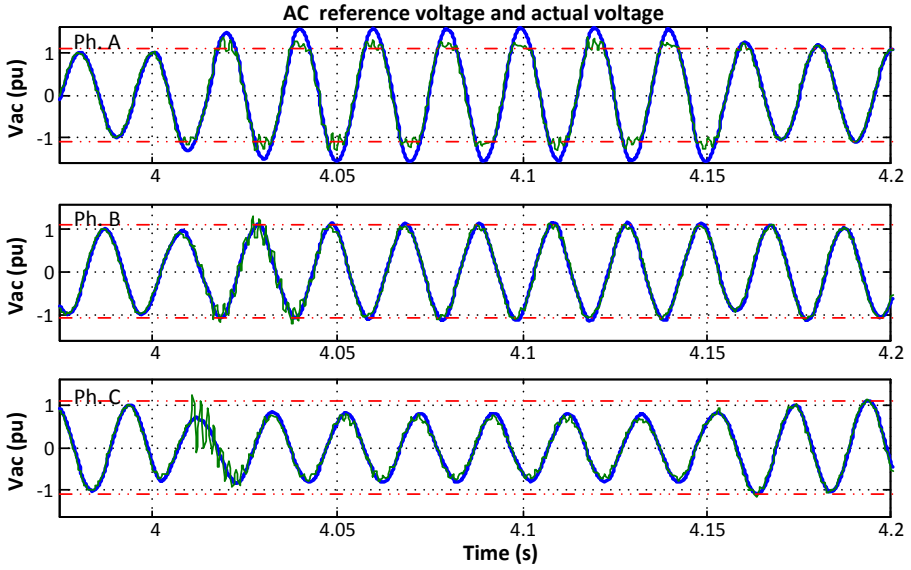


Figure 6.13. AC voltage reference (to the VSC) and actual voltage (measured at the filter bus) during the SLG fault at *FA* in case *WIH1*.

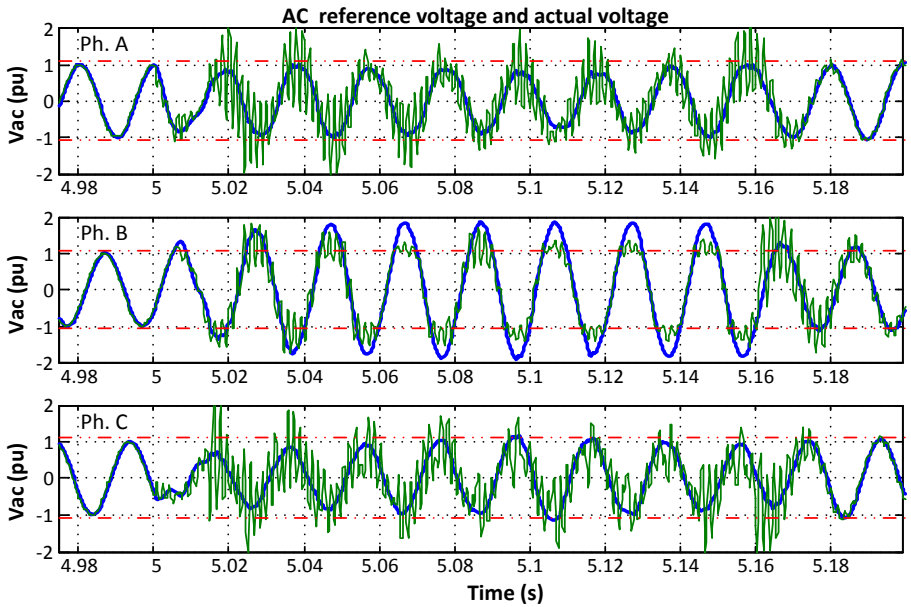


Figure 6.14. AC voltage reference (to the VSC) and actual voltage (measured at the filter bus) during the SLG fault at *FB* and case *WIH1*.

6.6 Summary

Negative sequence current injection control strategy has been formulated here for the special case of offshore wind power plants where the power reference for the VSC-HVDC converter is not available beforehand. Simultaneously the WTG converters have been provided with the negative sequence current control scheme to eliminate the oscillations in the active power.

It is demonstrated here that the simultaneous application of NSCCs in the VSC-HVDC and the WTG-GSCs reduce the dc voltage overshoot and the oscillations in the power flow to the VSC-HVDC, especially during the asymmetric faults. Post fault oscillations decays fast when the NSCCs are enabled. They are also effective in the reduction of high frequency component in the filter bus voltage.

7 RTDS Simulation of the Relay Coordination in the Offshore Grid

RTDS® simulation has been used to verify the proposed relay coordination for the protection of the offshore WPP grid. The test system model has been developed in RTDS, and then interfaced with a physical over-current relay through an amplifier. This chapter shows that the faults are detected, when they lie within the zone of protection and the associated circuit breaker is tripped to isolate the fault.

7.1 Introduction

Computer simulation provides a lot of insight into the real world phenomena. However, the simulation models are idealized to some level as all physical details cannot be modelled and simulated. For instance, the communication time lag, inherent filtering and the delay present in data acquisition, or even stray parameters and noises may affect the interaction between different components and controllers in a power system. Transient network analyzers (TNA) were developed to build an analog equivalent model of the power system such that the switching phenomena on the transmission lines could be studied. Multiple π -sections using inductors and capacitors were used to model the transmission lines, and circuit breakers were modelled by switches to simulate the electromagnetic characteristics in the scaled analog equivalent. In [78], Hirakami and Neugebauer describe the use of mini-computers with the TNA to take advantage of the digital computers and the analog network model. A real time digital TNA was first described in [79]

With the development of computer hardware and different EMT simulation programs, very large system models can be handled in great details nowadays. Even then, it is of prime importance to test the numerous interactions of a physical piece of controller hardware with the power system under different operating conditions.

Real Time Digital Simulator (RTDS®) is a platform which enables the interconnection of physical hardware devices with the digital EMT simulation of power system in real time with a typical time step of 50 μ s. [80]. Power electronic converters can be simulated with a small time step of around 2-3 μ s.

Physical hardware devices like relays or controllers can be interfaced with the simulation, and their performance can be simulated under various operating conditions.

This chapter describes the real time simulation of the offshore grid with a physical relay to assess the performance of the relay coordination and grid protection. In Chapter 5, a coordination method based on nominal current was proposed and simulated in PSCAD/EMTDC. Here the same system is tested using an industrial over-current relay for feeder protection (REF615 from ABB) connected to the system simulation in the RTDS platform

7.2 Experimental Set-up

The test WPP with VSC-HVDC model, which is described in Chapter 3 (Figure 3.1), is implemented in the RTDS platform using the RSCAD software. Digital simulation models of the current transformers are used from RSCAD model library. The test case is digitally simulated in RTDS. The relay CT currents are passed to the analog output cards as scaled voltages in the range of ± 5 V. Such a voltage signal, which is reflective of the CT currents in the digital simulation, is then amplified to the current signals using Omicron CMS156 amplifier. The amplifier is set with a gain of 5 A per volt. The amplified CT current is then applied to the over-current feeder protection relay IED (Intelligent Electronic Device), REF615 from ABB. A block diagram of the layout is shown in Figure 7.1.

The relay IED supports the IEC 61850 standard for GOOSE (Generic Object Oriented Sub-station Event) communication. The relay settings can be programmed using the PCM600 relay interface software and CCT600 for the horizontal communication configuration. The relay communicates the pick-up (start) and trip (operate) signals and it can read the blocking signal from the network.

The GTNET-GSE cards in the RTDS manages the GOOSE communication between the RTDS and the IEDs. It can thus receive the relay states and also send the blocking signal to them.

The test system has several converters. They were described in Chapter 3. Again, they are mentioned here in order to highlight the simplifications.

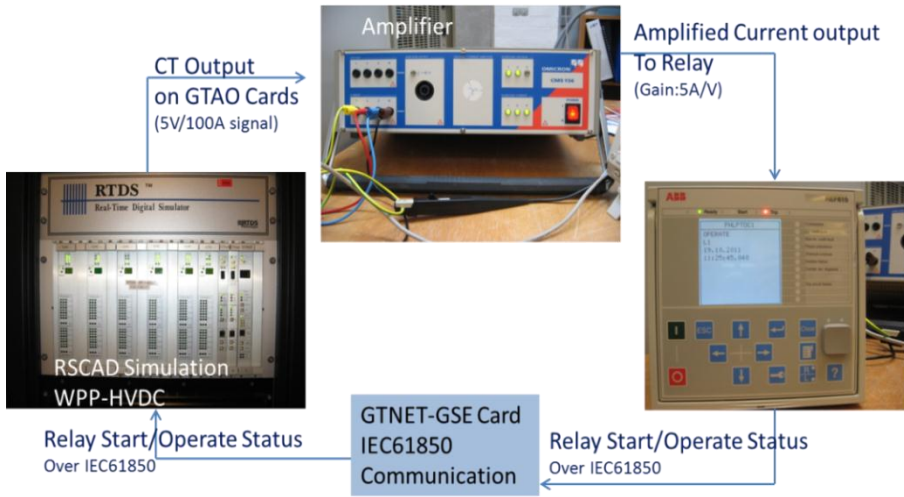


Figure 7.1 Block diagram of the experimental set-up.

7.2.1 WTG with FSC Model

In this study, the grid side inverters in the WTG were modelled as PWM switching inverters supplied by the constant dc voltage sources. The positive sequence terminal voltage is extracted using the SOGI filters and then a positive sequence PLL is used as shown in Figure 3.14 [53]. Vector control in rotating reference frame is used to control the inverter for the specified active power. The reactive power is controlled so as to maintain the nominal voltage across the capacitor of the LCL filter.

7.2.2 VSC HVDC Controllers

The onshore VSC-HVDC converter terminal controls the dc line voltage. Therefore, it evacuates the power absorbed by the offshore VSC-HVDC terminal. Simultaneously, it regulates the ac voltage at the filter bus by controlling the reactive power flow. It is described in Chapter 3 (Figure 3.15).

The basic function of the offshore VSC-HVDC controller is to establish the offshore grid voltage and frequency. Thus it creates a kind of infinite bus in the collector grid. The WTG-FSCs get synchronized with this bus and the generated power is absorbed by the VSC-HVDC converter. A simple ac voltage controller has been implemented here as shown in Figure 7.2. The error in RMS voltage at the PCC is applied to a proportional integral controller

which generates the d -axis voltage reference. The q -axis reference voltage was set to 0. Inverse Park's transformation was applied to get the phase voltage references for the modulation of the VSC-HVDC converter.

7.2.3 Over-current Limit Control in VSC

Active current limits are imposed by blocking the converter gate pulses for brief periods when the measured RMS current exceeds the pre-defined converter current limits (Figure 7.3). Their PI controllers are disabled during the periods when the converter is blocked.

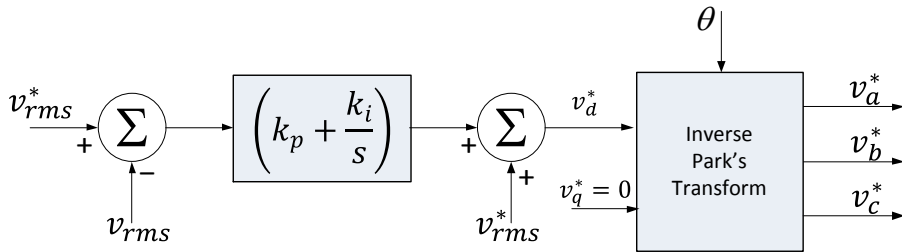


Figure 7.2. Block diagram of the offshore VSC-HVDC voltage controller.

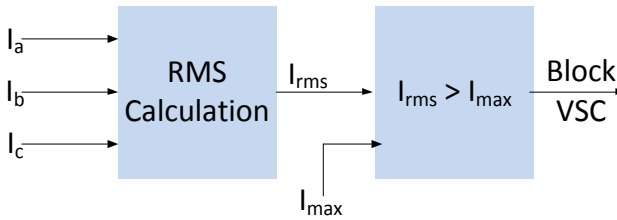


Figure 7.3. Limiting overcurrent by blocking the VSC.

7.2.4 Over-current Protection Functions of the Relay

The numerical relay IED REF615 provides several protection functionalities which can be programmed in the same unit [81]. In view of the non-directional over-current relay coordination, the following protection functions were identified:

1. Three Phase non-directional overcurrent protection 51P/50P
 - a. Low stage (PHLPTOC, $3I>$)
 - b. Instantaneous stage ($\text{PHIPTOC}, 3I>>>$)

2. Neutral overcurrent (Ground fault) protection 51N/50N
 - a. Non-directional - High stage (EFHPTOC, I0>>)
 - b. Directional - High stage (*directional unit disabled*) (DEFHPTOC, I0>>>).

For sake of comparison with the over-current relay coordination studies presented in Chapter 5, only the low stage three phase non-directional overcurrent protection (PHLPTOC, 3I>) was enabled. All other protective functions were turned off.

7.2.5 Over-current Relay Settings

7.2.5.1 MV Feeder relay

$$\text{Nominal current on MV Feeder} = \frac{112.5\text{MVA}}{\sqrt{3} \cdot 36\text{kV}} = 1804\text{A}$$

$$C.T. \text{ Ratio} = 1:400$$

$$GTAO \text{ Gain} = 5\text{V}/100\text{A}$$

$$\text{Amplifier gain} = 5\text{A}/1\text{V}$$

$$\therefore \text{Feeder current to relay current ratio} = 1600:1$$

Setting the relay secondary current as 1A,

$$\text{Nominal relay current} = \frac{1804}{1600} = 1.1275\text{A} = 1.1275\text{xIn}$$

$$\text{Pick up current} = 1.25\text{pu} = 1.41\text{xIn}$$

$$\text{Time multiplier} = 0.05$$

$$\text{Operating curve type} = \text{ANSI Very Inverse}$$

$$\text{Reset curve} = \text{Immediate}$$

7.2.5.2 HV Cable Feeder relay

$$\text{Nominal current on HV Feeder} = \frac{225\text{MVA}}{\sqrt{3} \cdot 150\text{kV}} = 866\text{A}$$

$$C.T. \text{ Ratio} = 1:200$$

$$GTAO \text{ Gain} = 5\text{V}/100\text{A}$$

$$\text{Amplifier gain} = 5\text{A}/1\text{V}$$

$$\therefore \text{Feeder current to relay current ratio} = 800:1$$

Setting the relay secondary current as 1A,

$$\text{Nominal relay current} = \frac{866}{800} = 1.0825\text{A} = 1.0825\text{xIn}$$

Pick up current = 1.25pu = 1.353xIn

Time multiplier = 0.05

Operating curve type = ANSI Very Inverse

Reset curve = Immediate

7.3 GOOSE Communication Set-up

The IED REF615 was configured using the proprietary tool CCT600 to broadcast the following signals —

1. PHIPTOC1.Str, PHIPTOC1.Op
2. PHLPTOC1.Str, PHLPTOC1.Op
3. EFHPTOC1.Str, EFHPTOC1.Op
4. DEFHPTOC1.Str, DEFHPTOC1.Op

As per IEC61850 standards, the names of these signals indicate the corresponding protective function. These are described in Section 7.2.4. The suffix 'Str' indicates the 'start' or the pick up of the relay function and the suffix 'Op' indicates the 'Operate' or the trip of the corresponding function. Since only the non-directional over-current relay (PHLPTOC) was used here, PHLPTOC1.Str and PHLPTOC1.Op were the relevant GOOSE signals for the three phases.

Apart from this, the GTNET-GSE card in the RTDS is configured to send the blocking signal to prevent the relay from picking up when the MV feeder relay has picked up.

7.4 Simulation and Results

7.4.1 Steady State RTDS Simulation:

Figure 7.4 shows the dc voltage, power and current waveforms during the steady state operation of the wind power plant and VSC-HVDC. While the total harmonic distortion for the dc voltage was 6.5%, the peak to peak ripple was within $\pm 3\%$ of the nominal. The four aggregated WTGs were generating 0.85, 0.86, 0.87 and 0.88 pu active power (on 100 MW base).

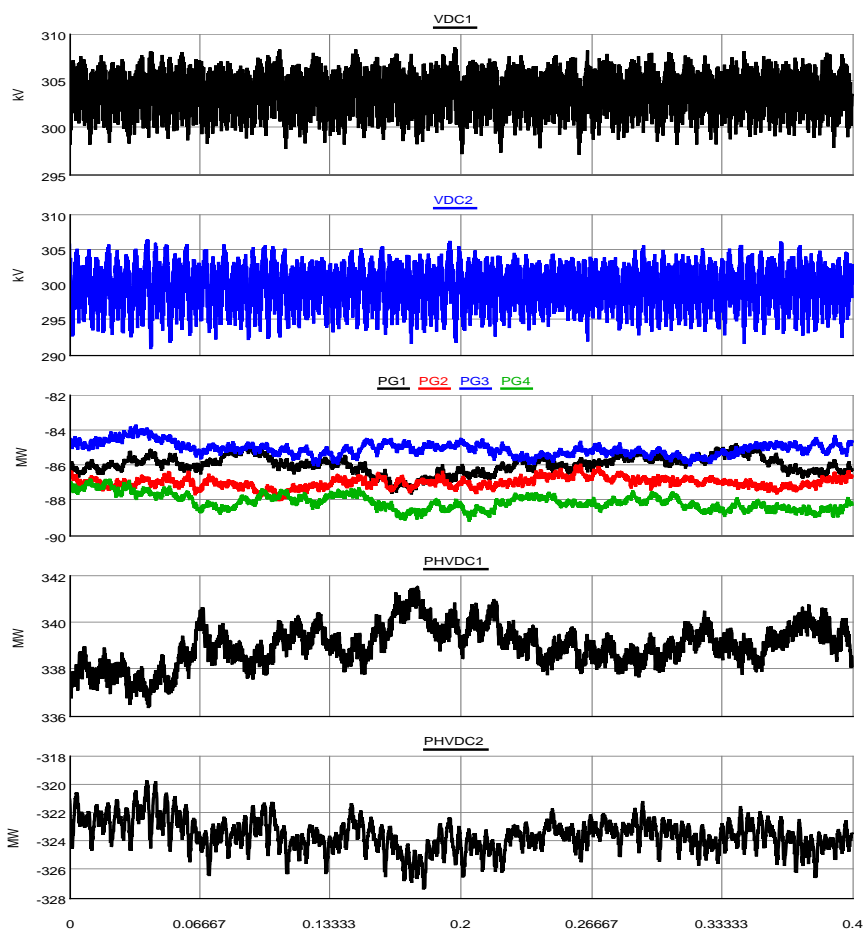


Figure 7.4. Steady state results (in pu) (i)HVDC voltage at offshore terminal (ii) HVDC voltage at the onshore terminal (iii) Power generated by the 4 WTGs (v) Power transmitted to the offshore VSC-HVDC terminal (vi) Power transmitted by the onshore VSC-HVDC terminal

The 400 MW offshore VSC-HVDC transmission system was receiving 0.85 pu power and supplying 0.81 pu power to the onshore grid. Thus there was 0.04 pu power loss in the converters and the 200 km long DC cable. All these power data were measured at the ac terminals of the converters.

Figure 7.5 shows the voltage signal acquired from the RTDS simulation. It represents the current passing through the MV feeder relay CT in steady state. Considering the CT ratio of 400:1, and the scaling factor in the GTAO of 100:5, 260-mV-peak voltage signal corresponded to the 1.47 kA primary current in the steady state. It was amplified to the overlapping IED current

waveform of 1.3A-peak by the Omicron amplifier CMS156 with a current gain of 5A/V.

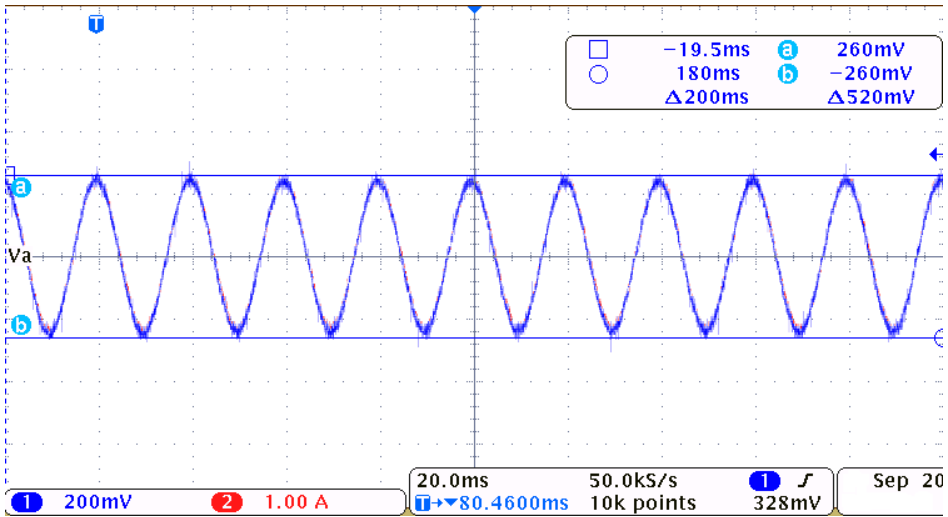


Figure 7.5 Voltage signal at the GTAO output and the overlapping current signal output of the amplifier.

7.4.2 Comparison with PSCAD Simulation Results

First of all the RTDS simulation set-up was compared with the PSCAD simulations carried out earlier for the sake of validation. A single line to ground (SLG) fault was applied on the MV feeder at *FA*. The sudden disturbance resulted in power unbalance. A transient over-voltage of 1.54 pu peak was observed in the HVDC transmission as shown in Figure 7.6. In PSCAD simulation, 1.52 pu DC link over-voltage had been observed in similar simulations in Chapter 6. Power injected into the VSC-HVDC system dropped to a minimum of 0.38 pu in RTDS simulation whereas it was 0.34 pu in PSCAD simulation (as given in Table 6.1). The corresponding PSCAD curves have been included here (from Figure 6.8, Figure 6.9) for a quick comparison and validation of the RTDS model. Similar power and voltage oscillations were observed during the fault events, though the oscillation amplitudes appear to be lower in the RTDS simulation. The oscillations died out after the fault got cleared.

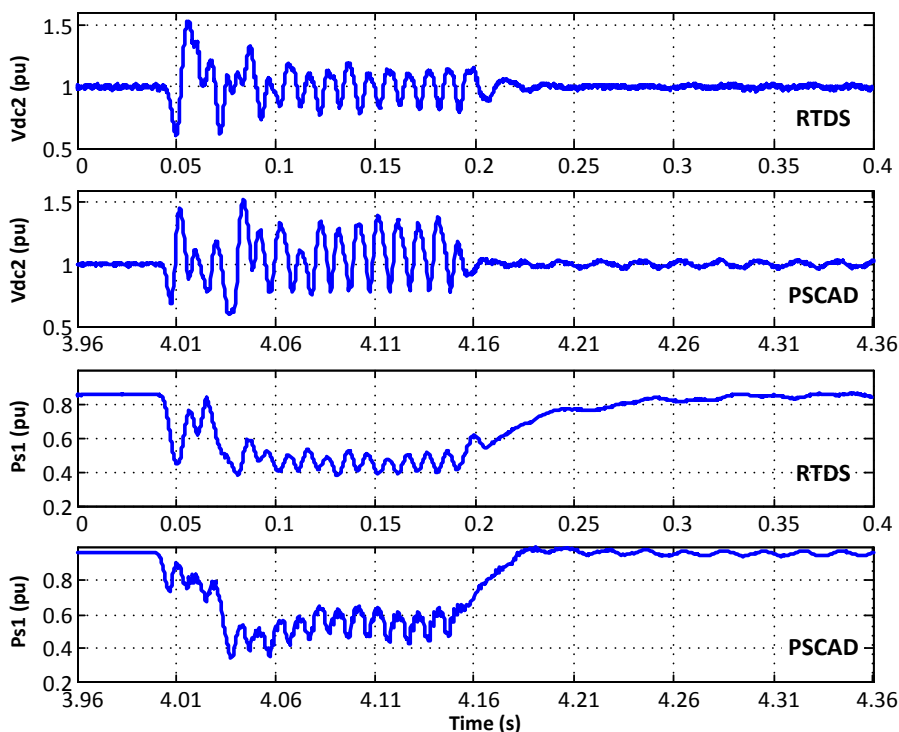


Figure 7.6 DC voltage and power flow during SLG fault on MV feeder. Corresponding curves from PSCAD simulation is included for comparison.

A comparison of the fault and relay CT current waveforms in PSCAD and RTDS simulations is shown in Figure 7.7. The fault current and the MV CT feeder current were almost similar in waveform and peak levels. However, the current waveform for the HV CT showed a deviation. The peaks in RTDS simulation were 2.28 pu; while the peaks were at 3.05-pu level in the PSCAD simulation. Apart from this, the waveform in RTDS had lower amount of harmonic content compared to the waveform obtained from PSCAD simulation.

It must be noted here that the PSCAD simulations were carried out with a time step of 8 μ s, while the RTDS simulation have a fixed time step of 50 μ s for the power system components and 2 μ s for the small time step power converter switching simulations.

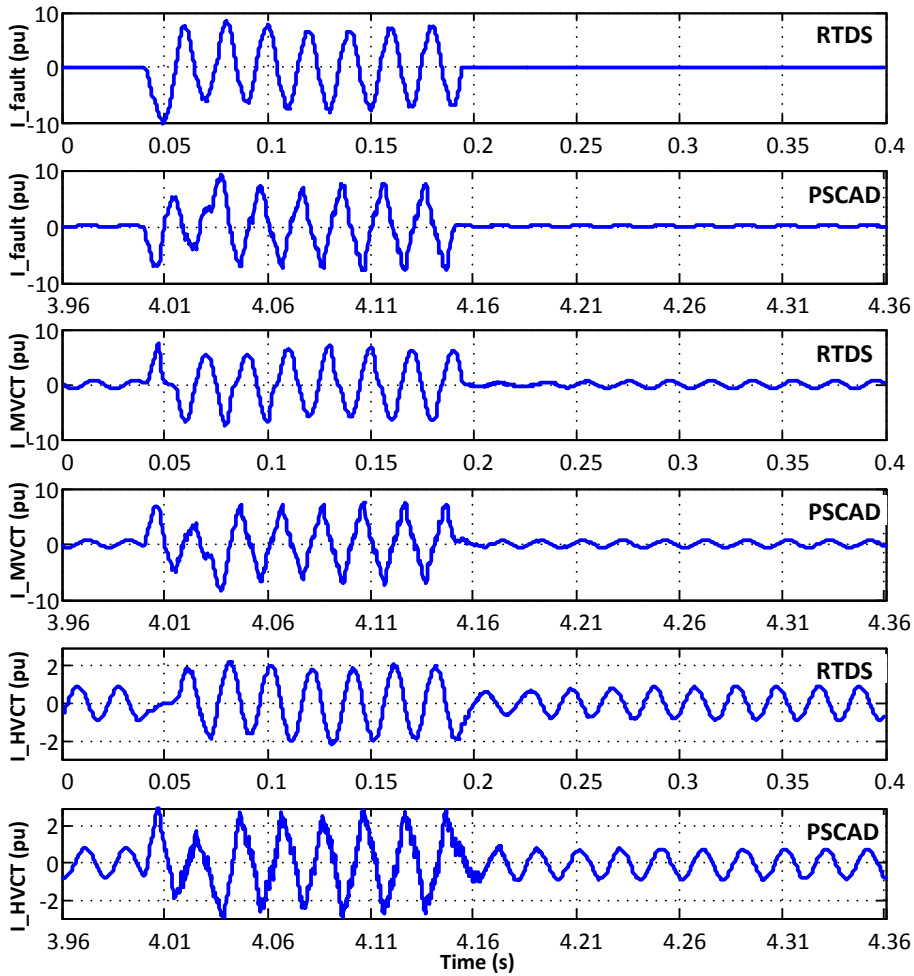


Figure 7.7. Comparison of the RTDS and PSCAD current waveforms during SLG fault at FA.

7.4.3 Single Line to Ground Fault on an MV Feeder

A single line to ground (SLG) fault was applied at *FA* on the 36-kV MV feeder #4. Analog voltage signals were obtained from the secondary current of the relay CT on the analog output cards of the RTDS, as shown in Figure 7.8. It was then amplified into fault current waveform, which is exactly overlapped by the voltage signal.

The RTDS simulation output data were saved as comtrade files, so that they could be recovered later. Since, the fault instant was used as the trigger, the fault instant is recorded as time 0 s. As shown in Figure 7.9, the maximum

absolute peak fault current was 7.99 pu (i.e. 20.38 kA) at 1.04s. The maximum absolute peak currents passing through the MV CT was 45.18 A (7.08 pu) at 0.054 s. (The fault current through the MV CT, in Figure 7.10, is inverted from the one shown in Figure 7.8). Due to the transformer connection, the fault appeared as an LL fault on the HV side. The maximum absolute peak currents through the HV feeder CT was recorded as 12.25 A (2.00 pu) at 0.046 s in phase A and 13.33 A (2.18 pu) at 0.014 s in phase B.

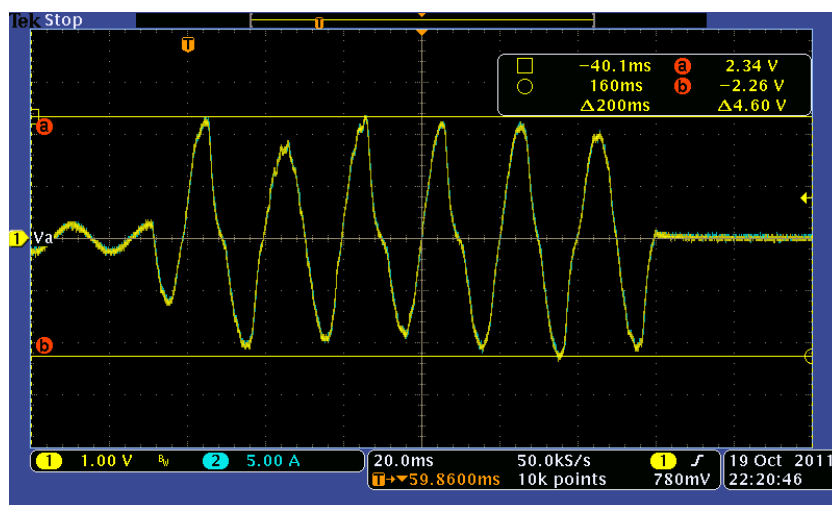


Figure 7.8. Voltage signal from the RTDS simulation and the corresponding amplified current signal (the blue curve under the yellow curve).

The relay IED on the faulted MV feeder started at 12 ms and tripped at 72 ms. Since a delay of 50 ms was assumed for the circuit breaker operation, the breaker opened at 122 ms.

Even the HV feeder relay picked up at 24.8 ms as a large fault current flowed through the HV feeder CT. However, it was blocked from tripping by the MV feeder relay which activated earlier. A delay of 15 ms was assumed for the communication of the blocking signal.

The variations in the dc voltage and the power-flow during the fault are shown in Figure 7.10. The dc voltage as well as the healthy section of the WPP recovered to their normal operation soon after the fault was cleared. The WTG #4 got isolated by the opening of the circuit breaker. Consequently, the power-flow to the HVDC dropped to 0.75 pu from the pre-fault level of 0.98 pu.

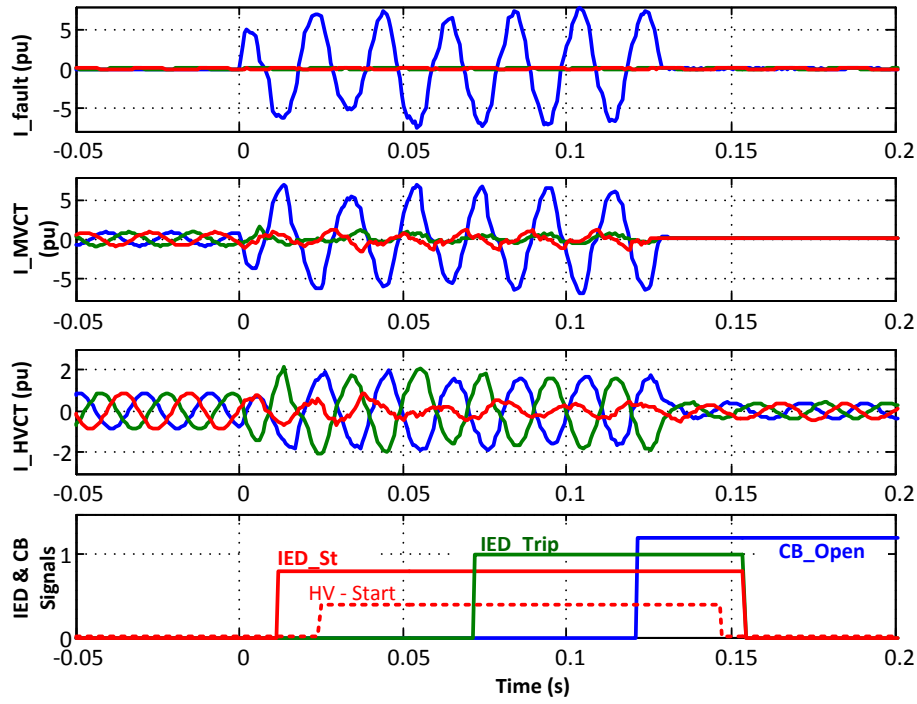


Figure 7.9. Fault currents, the relay signals, and the breaker opening during SLG fault at FA.

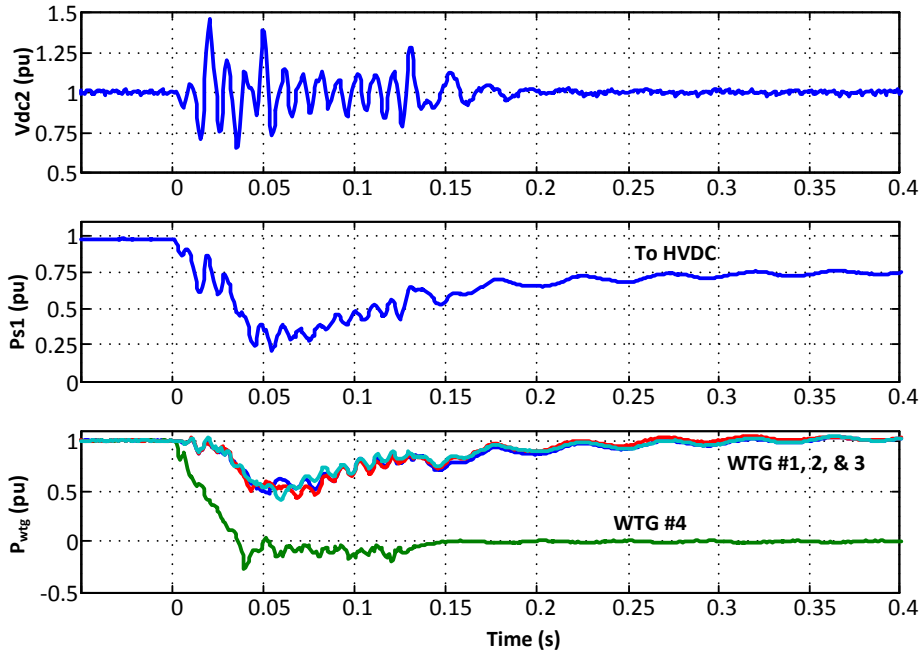


Figure 7.10. Dc voltage and power during SLG fault at FA.

7.4.3.1 Measurement Data Captured in the IED REF615

The fault time current waveforms captured by the relay IED are shown in Figure 7.11. These waveforms are similar to those captured on the oscilloscope (Figure 7.8, phase A only) and in the RTDS scopes (Figure 7.9); except that the waveform in the oscilloscope is inverted. Thus, the real time simulation set-up with the relay gets validated. The current data computed by the relay is given in Table 7.1. Nevertheless, the numerical data captured in the IED appears to be lower than the recorded waveforms. For instance, the maximum current peak in the relay is recorded as 7.45 A. Considering the net gain of the analog output card $\left(\frac{5V}{100A}\right)$ and the amplifier $\left(\frac{5A}{1V}\right)$, it implies a peak fault current of 29.8A in the secondary of the feeder CT, and therefore, 16.86 kA (or 6.61 pu) in the primary winding of the MV feeder CT. As per Figure 7.9, it should be 7.08 pu. The difference could be attributed to the fault current estimation algorithm used in the relay software.

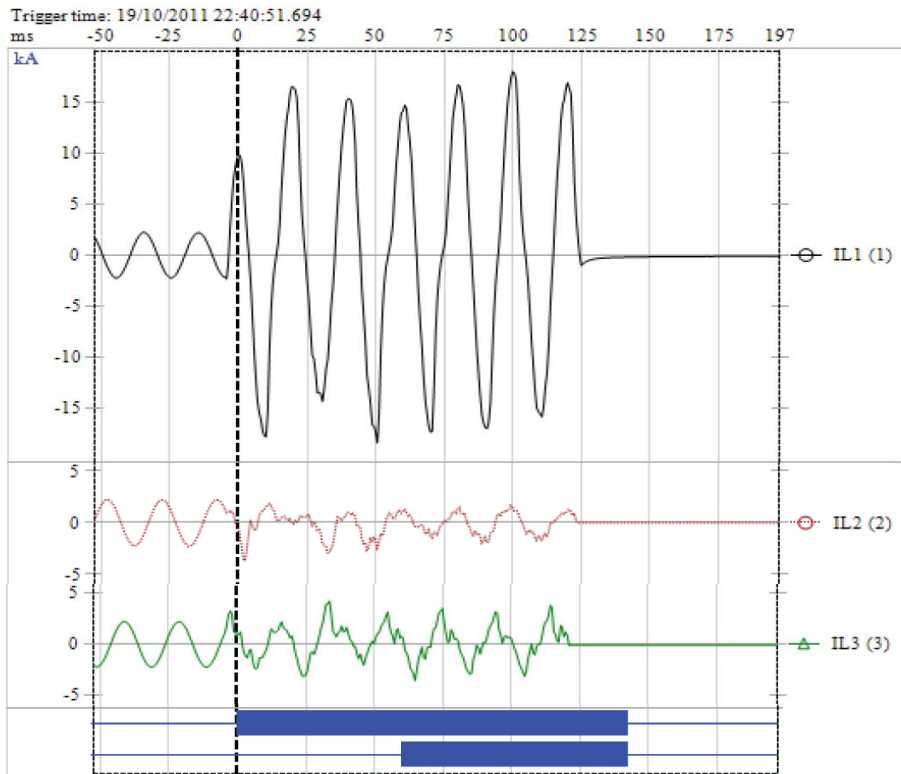


Figure 7.11. Fault current waveforms recorded by REF615 during SLG fault at FA..

Table 7.1 Fault Report Summary for SLG fault at *FA* from the ABB REF615 Relay

| | |
|--|-------------------------|
| Fault Number: 628 / Time and Date: 19.10.2011 22:40:51.694 | |
| Start duration..... | 100% |
| Setting group..... | 1. |
| Max current IL1..... | 7.453...xIn→16.86kA, pk |
| Max current IL2..... | 0.956...xIn→ 2.16kA, pk |
| Max current IL3..... | 1.204...xIn→ 2.72kA, pk |
| Current IL1..... | 6.677...xIn→15.11kA, pk |
| Current IL2..... | 0.738...xIn→ 1.67kA, pk |
| Current IL3..... | 0.711...xIn→ 1.61kA, pk |
| Current Io..... | 0...xIn |
| Current Io-Calc..... | 7.564...xIn→17.12kA, pk |
| Current Ps-Seq..... | 2.218...xIn→ 5.02kA, pk |
| Current Ng-Seq..... | 1.984...xIn→ 4.49kA, pk |

7.4.4 Double Line to Ground (LLG) Fault on an MV Feeder

The RTDS simulation results of a double line to ground (LLG) fault applied at *FA* are shown in Figure 7.12. The peak (maximum of the absolute value) fault current for the LLG fault is 14.83 kA (5.81 pu) in phase A and 20.31 kA (7.96 pu) in phase B. The peak (maximum absolute) fault current in the MV feeder relay CT is 34.20 A (5.36 pu) in phase A, and it is 48.32 A (7.58 pu) in phase B. Similarly, in the HV feeder CT, the peak (maximum absolute) current is 17.98 A (2.94 pu) in phase B, and 15.01 A (2.45 pu) in phase C.

The REF615 IED started at 10.4 ms and it tripped at 90.4 ms. Consequently, the MV circuit breaker opened at 140 ms. WTG #4 was not disconnected and it continued to supply a small fault current for some time. Although, the HV feeder relay picked up at 19.2 ms, its tripping operation was blocked by the blocking signal from the MV feeder relay IED.

The results captured in the relay IED are given in Table 7.2. Likewise the SLG fault data, these currents are lower than the current observed in the RTDS plots.

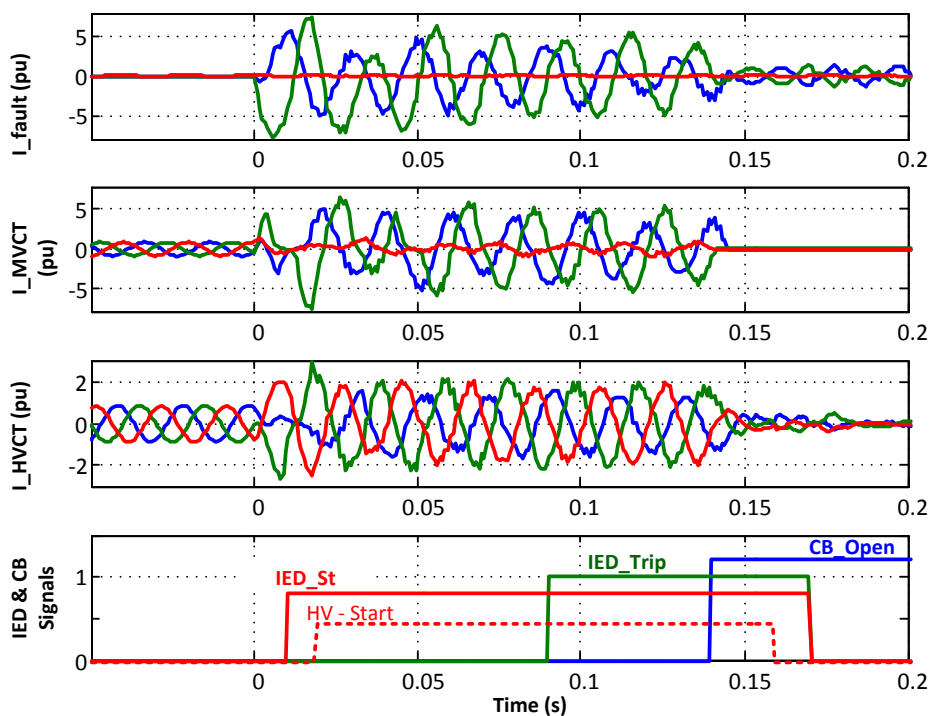


Figure 7.12 Fault currents, relay signals and circuit breaker state during an LLG fault at FA.

Table 7.2 Fault Report Summary for LLG fault at FA from the ABB REF615 Relay

| | | |
|--|--------------|------------|
| Fault Number: 629 / Time and Date: 19.10.2011 22:43:29.884 | | |
| Start duration..... | 100% | |
| Setting group..... | 1 | |
| Max current IL1..... | 5.2 ...xIn→ | 11.77kA,pk |
| Max current IL2..... | 7.246...xIn→ | 16.40kA,pk |
| Max current IL3..... | 1.106...xIn→ | 2.50kA,pk |
| Current IL1..... | 3.854...xIn→ | 8.72kA,pk |
| Current IL2..... | 5.759...xIn→ | 13.03kA,pk |
| Current IL3..... | 0.662...xIn→ | 1.50kA,pk |
| Current Io..... | 0...xIn | |
| Current Io-Calc..... | 5.867...xIn→ | 13.28kA,pk |
| Current Ps-Seq..... | 3.351...xIn→ | 7.58kA,pk |
| Current Ng-Seq..... | 1.041...xIn→ | 2.36kA,pk |

7.4.5 Triple Line to Ground (LLLG) Fault on an MV Feeder

The current waveforms and the relay signals of a triple line to ground fault applied at *FA* on the MV feeder are shown in Figure 7.13 and the data recorded by the relay IED are given in Table 7.3. It is a case of symmetric fault as all the three phases are involved. The maximum amplitudes of the fault current are 16.33 kA (6.40 pu) in phase A, 14.79 kA (5.80 pu) in phase B, and 15.60 kA (6.12 pu) in phase C. The MV feeder CT secondary currents were recorded as 38.42 A (6.02 pu) in phase A at 17 ms, 31.12 A (4.88 pu) in phase B at 14 ms and 35.62 A (5.584 pu) in phase C at 19 ms.

The relay IED started at 11.2s, but it tripped at 196 ms. Therefore, the fault got isolated only at 246 ms. The symmetrical fault case resulted in a lower amplitude of the fault current and hence the relay took a longer time to operate. The HV relay picked up at 17.6ms, but it is prevented from tripping by the blocking signal from the MV relay.

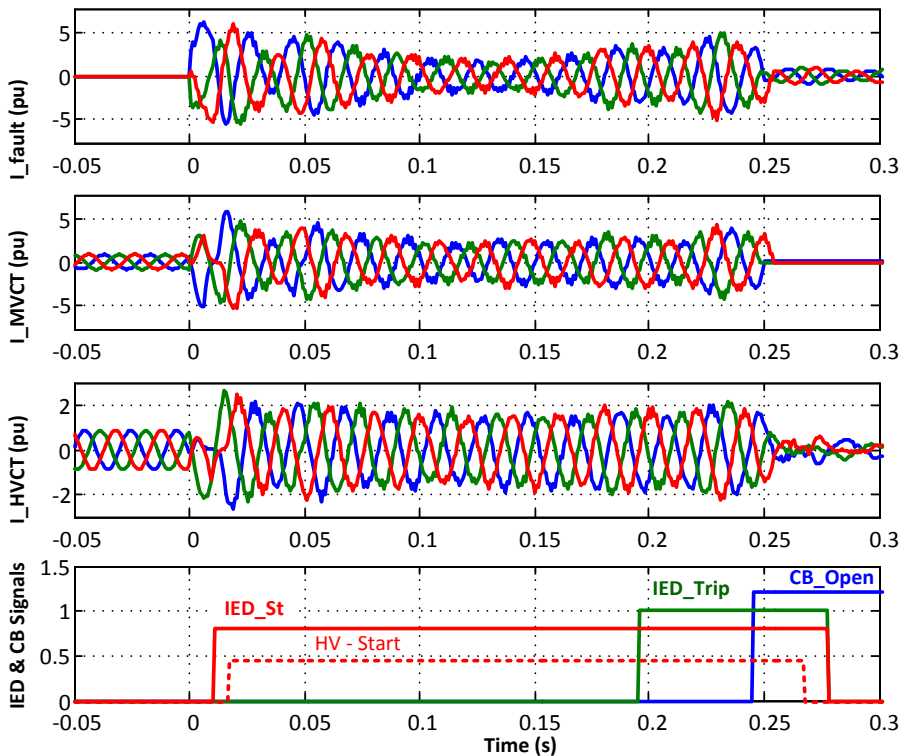


Figure 7.13 Fault currents, relay signals and circuit breaker state during an LLLG fault at *FA*.

Table 7.3 Fault Report Summary for LLLG fault at *FA* from the ABB REF615 Relay

| Fault Number: 630 / Time and Date: 19.10.2011 22:46:19.667 | | |
|--|--------------|-------------|
| Start duration..... | 100% | |
| Setting group..... | 1 | |
| Max current IL1..... | 5.4 ...xIn→ | 12.22kA, pk |
| Max current IL2..... | 4.926...xIn→ | 11.15kA, pk |
| Max current IL3..... | 5.044...xIn→ | 11.41kA, pk |
| Current IL1..... | 2.953...xIn→ | 6.68kA, pk |
| Current IL2..... | 3.051...xIn→ | 6.90kA, pk |
| Current IL3..... | 2.992...xIn→ | 6.77kA, pk |
| Current Io..... | 0...xIn | |
| Current Io-Calc..... | 0.002...xIn→ | 0.00kA, pk |
| Current Ps-Seq..... | 2.998...xIn→ | 6.78kA, pk |
| Current Ng-Seq..... | .07 ...xIn→ | 0.16kA, pk |

7.4.6 SLG Fault on a HV Feeder

Different faults were studied at both the fault locations, *FA* on the MV feeder and *FB* on the HV feeder. The results of a single line to ground (SLG) fault is described in this section. Waveforms for the fault currents, the relay signals, and the breaker state are shown in Figure 7.14.

The maximum value of the fault current peak was 11.1 kA (4.35 pu) during the SLG fault. By virtue of transformer connection, it appeared as the LL fault on the MV feeder. During the fault, the MV feeder CT currents were 8.49 A (1.33 pu) in phase B and 11.25 A (1.76 pu) in phase C. A transient peak of 10.6 A (1.66 pu) was observed in phase A at 3 ms.

The IED on the HV feeder picked up at 10.4 ms and it tripped at 157.6 ms, thereby opening the MV circuit breaker at 207.2 ms. The fault current continued for some more time as the WTG#3 and WTG#4 were not disconnected immediately. The recording from the relay IED is given in Table 7.4. Since it was an SLG fault, there was a strong presence of the negative and zero sequence components.

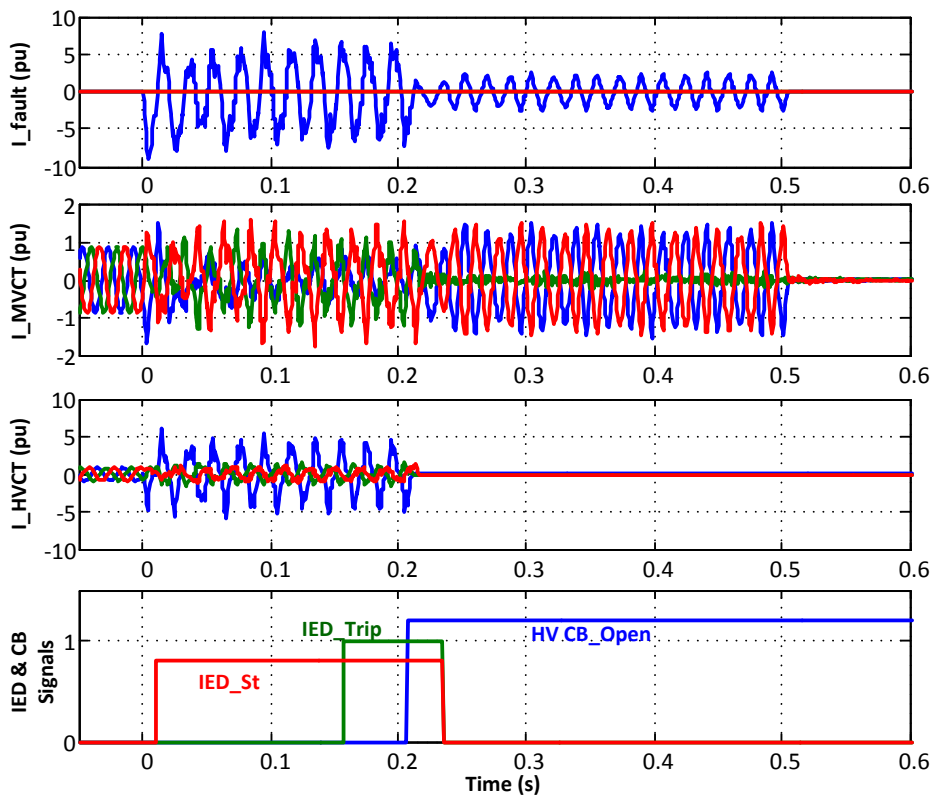


Figure 7.14 Fault currents, relay signals and circuit breaker state during an SLG fault at *FB*.

Table 7.4 Fault Report Summary for SLG fault at *FA* from the ABB REF615 Relay

| | |
|--|------------------------|
| Fault Number: 639 / Time and Date: 20.10.2011 14:01:29.902 | |
| Start duration..... | 100% |
| Setting group..... | 1. |
| Max current IL1..... | 4.059...xIn→4.59kA,pk |
| Max current IL2..... | 1.316...xIn→ 1.49kA,pk |
| Max current IL3..... | 0.985...xIn→ 1.11kA,pk |
| Current IL1..... | 3.963...xIn→ 4.48kA,pk |
| Current IL2..... | 1.109...xIn→ 1.25kA,pk |
| Current IL3..... | 0.814...xIn→ 0.92kA,pk |
| Current Io..... | 0...xIn |
| Current Io-Calc..... | 2.865...xIn→ 3.24kA,pk |
| Current Ps-Seq..... | 1.818...xIn→ 2.06kA,pk |
| Current Ng-Seq..... | 1.284...xIn→ 1.45kA,pk |

7.4.7 Overcurrent Relay Trip Times for the Different Faults

The trip times taken by the REF615 relay IED for the different faults at *FA* on the MV feeder and at *FB* on the HV feeder are presented in Figure 7.15. The results from the PSCAD simulations, described earlier in Chapter 5, are included for the sake of comparison. The two results are closely matching with a deviation of less than 20 ms in most of the cases. Nevertheless, there are higher differences in some cases; like 51 ms (22%) for the LLL fault at *FA*, 60 ms (31%) for the LLG fault at *FB*, and the highest difference of 164 ms (45%) for the LL fault at *FB*. In general, there was a good match between the simulated and practically observed cases; and the exact cause of the variation was not investigated in this project.

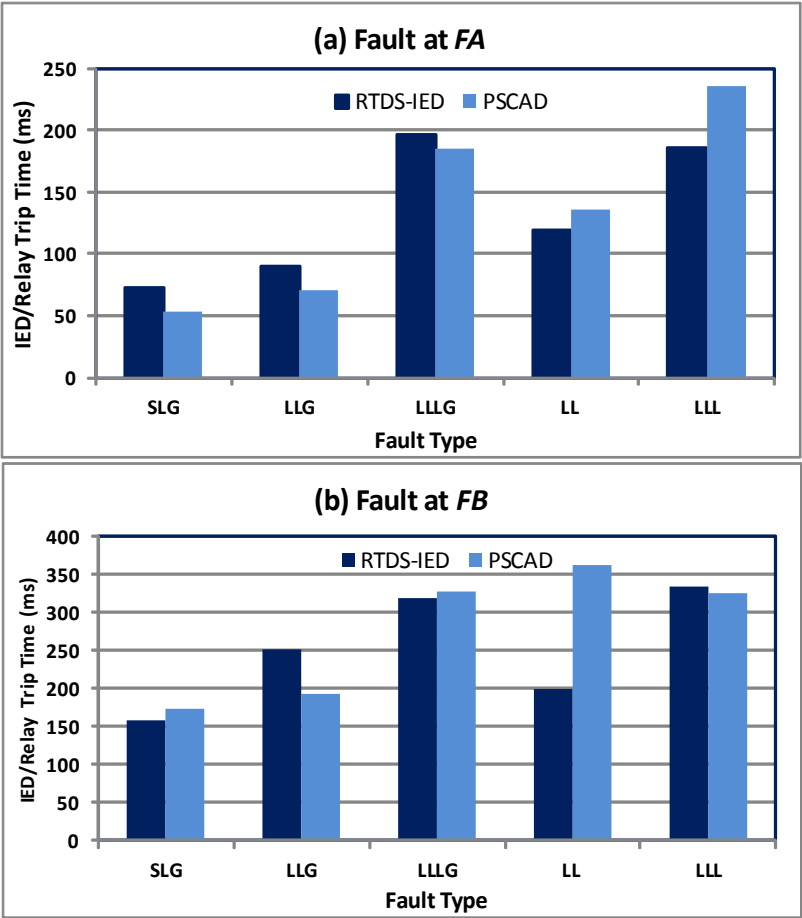


Figure 7.15 Trip times for the different faults. (a) at *FA* on the MV feeder; (b) at *FB* on the HV feeder.

In both the PSCAD and the RTDS simulations, it was found that the relay took longer time to trip for symmetrical faults (LLL and LLLG) compared to the asymmetric faults. In case of symmetric faults, the fault current had a high amplitude in the first cycle, but soon it had a low content of the fundamental component as shown in Table 5.4.

Apart from this, the HV feeder relay took longer time to trip for the faults on the HV feeder in comparison to the time taken by the MV feeder relay for the faults in the MV feeder. It is so because the HV feeders are rated for twice the power rating of the MV feeders. The slow response of the HV feeder relay was advantageous in the sense that the undesirable tripping of the HV feeder relay for the faults on the MV feeder was delayed. This allowed for the communication based interlocking of the HV feeder relay by the relay pick-up signal from the MV feeder relay.

7.5 Summary

The experimental set-up for the testing of the offshore grid relay coordination has been described in this chapter. The relay tripping behaviour for the faults on the MV feeder has been recorded and compared with the results obtained from PSCAD simulations. The relay coordination on the basis of nominal current ratings along with the inter-locking mechanism has been demonstrated to work satisfactorily in all the cases.

The performance and discrimination could be further enhanced using other available protective functions like a combination of the high stage over-current relays, the instantaneous overcurrent relay, and the earth fault over-current relay. The experimental set up is ready and the study will be extended to come out with a more comprehensive protective solution.

The RTDS simulation set-up provided a platform for multiple simulation studies of the fault cases in the offshore grid. It can be used to study hundreds of potential cases for testing the relay and control hardware in the converter connected grid like the offshore WPP grids.

8 Conclusions and Future Work

This chapter summarizes the thesis and highlights some areas for further research in the domain of grid integration of offshore wind power using VSC-HVDC transmission.

8.1 Conclusions

A test system for the study of wind power plants with VSC-HVDC connection to the onshore grid has been proposed. It is elaborate enough to include the detailed switching model of the VSC-HVDC transmission system. The offshore grid is modelled in terms of four aggregated wind turbine generators, the associated filters, and the ac collector grid network. The system is suitable for the simulation study of faults and other transients in the offshore WPP grid as well as steady state response analyses.

A new controller for the offshore VSC-HVDC converter terminal has been proposed. It is an adaptation of the standard vector control by adding the feed-forward WPP current terms calculated from the measured active and reactive power injection to the VSC-HVDC terminal. Its robustness is evident from the numerous fault studies done on the test system.

Different frequency control scheme through VSC-HVDC has been implemented and demonstrated.

Fault ride through capability of an offshore grid with VSC-HVDC connection has been demonstrated. Elimination of braking resistors on the VSC-HVDC transmission system was analysed with different LVRT algorithms. It was concluded that the rapid reduction of the offshore grid voltage would produce the minimum over-voltage in the HVDC system. If communication is used, very fast and reliable communication has to be used.

Several different faults in the offshore WPP collector grid have been investigated through EMT simulations in PSCAD. A detailed layout of the test wind power plant system with collector grid and VSC-HVDC connection the onshore grid is developed in Chapters 3 and 4. The use of simple over-current relays has been proposed along with their coordination scheme for the protection of the offshore WPP and their performance is demonstrated through

PSCAD simulations. The results are further corroborated through a real time simulation in RTDS with an industrial relay from ABB. The RTDS simulation model and hardware in loop configuration with IEC 61850 process bus communication set-up can be used to investigate the different control and protective features of modern numerical relays.

The system is designed for three phase balanced positive sequence operation. However, asymmetric faults may lead to unbalanced voltage conditions and current flows. In Chapter 6, the unbalanced voltage and currents are separated into the positive and negative sequence components and an expression for the power oscillation has been derived. Negative sequence current controller for the offshore VSC-HVDC system has been formulated using the estimated positive sequence current, and both positive and negative sequence voltage. The controller performance in minimizing the dc voltage oscillations is demonstrated through EMT simulations. The controller can remain active all the time, but it affects the system only when the negative sequence voltage components appear in the system.

8.2 Main Contributions

A layout of an offshore WPP with collector grid system and VSC-HVDC connection to the onshore grid has been developed in PSCAD. A new converter control algorithm has been proposed for the offshore VSC-HVDC terminal. It is implemented in the test system and the different operating modes as well as faults have been simulated to verify the control and plant efficacy. The offshore VSC-HVDC controller was improved by including the WPP current injection terms derived from the measured active and reactive power at the offshore HVDC-terminal.

A simple numerical method has been presented for the estimation of fault current levels in the event of offshore grid faults in the collector grid. The limitations and the shortcomings of the proposed method has been highlighted. The scheme is demonstrated through EMT simulations in PSCAD. Later, these are compared with those of an industrial relay connected with the real time simulation.

A new algorithm of negative sequence current control using only the current and voltage measurements in the offshore VSC-HVDC terminal has

been proposed to reduce the power, and hence, the dc voltage oscillations in the VSC-HVDC transmission. It does not depend upon the instantaneous power references. Simulation studies have been carried out to demonstrate the efficacy of having the negative sequence current control in the VSC-HVDC system and the WTG converters.

8.3 Future Work

Recently the modular multilevel converter (MMC) topologies have been developed for the VSC-HVDC transmission. These converters are claimed to have a better dynamic performance and improved controllability in comparison to the two-level or three-level VSC-HVDC transmission. All the new wind power plants in the North Sea are going to be connected using MMC-HVDC. The control and operation of wind power plants with MMC-HVDC and the impact upon the protection schemes needs further investigation.

Moreover, a dc super-grid overlay has been envisaged using MMC-HVDC. The coordinated operation of the multi-terminal HVDC systems needs more research.

On the protection side, the IEC61850 based process bus communication can provide improved control and protection capabilities for the operation and control of wind power plants.

This thesis is focussed upon the offshore grid. The work can be extended to investigate the impact of wind power plants with VSC-HVDC connection on the onshore grid, especially with regard to inertia emulation, frequency regulation and fault ride through in the multi-terminal VSC-HVDC systems with multiple inter-connections between the offshore wind power plants and ac power grid networks.

8.4 Author's Publication List

8.4.1 Paper Published

- [1] S. K. Chaudhary, R. Teodorescu, P. Rodriguez, "Wind Farm Grid Integration Using VSC Based HVDC Transmission - An Overview," in IEEE Energy 2030 Conference, 2008. ENERGY 2008. IEEE, 2008.

- [2] S. K. Chaudhary, R. Teodorescu, P. Rodriguez, P.C. Kjær and P. W. Christensen, "Chopper Controlled Resistors in VSC-HVDC Transmission for WPP with Full-scale Converters," in Proc. of Conference on Sustainable Alternative Energy (SAE), 2009.
- [3] S. K. Chaudhary, R. Teodorescu, P. Rodriguez, P.C. Kjær and P. W. Christensen, "Modelling and Simulation of VSC-HVDC Connection for Wind Power Plants," in Proc. of the 5th Nordic Wind Power Conference : Power System Integration and Electrical Systems of Wind Turbines and Wind Farms. 2009.
- [4] S. K. Chaudhary, R. Teodorescu, R. N. Mukerjee, P. Rodriguez, P.C. Kjær and P. W. Christensen, "Simulation Study of WPP-HVDC-Grid Integrated System," in Proc. of the Simulation Study of WPP-HVDC-Grid Integrated System, Energynautics GmbH, 2009.
- [5] S. K. Chaudhary, R. Teodorescu, P. Rodriguez, P.C. Kjær and P. W. Christensen, "Modelling and Simulation of VSC-HVDC Connection for Offshore Wind Power Plants," in Proc. of the Danish PhD Seminar on Detailed Modelling and Validation of Electrical Components and Systems 2010. Energinet.dk, 2010, 53-57.
- [6] S. K. Chaudhary, R. Teodorescu and P. Rodriguez, "Control and Operation of Wind Turbine Converters during Faults in an Offshore Wind Power Plant Grid with VSC-HVDC Connection," IEEE-PES General Meeting 2011, 24-28 July 2011.
- [7] S. K. Chaudhary, R. Teodorescu, P. Rodriguez, P. C. Kjær, "Application of Over-current Relay in Offshore Wind Power Plant Grid with VSC-HVDC Connection," in 10th International Workshop on Large-Scale Integration of Wind Power into Power Systems as well as on Transmission Networks for Offshore Wind Power Plants. Aarhus, Denmark on October 25 - 26, 2011.

8.4.2 Co-authored Publications

- [8] U. N. Gnanarathna, S. K. Chaudhary, A. M. Gole and R. Teodorescu, "Modular Multi-level converter based HVDC System for Grid Connection of Offshore Wind Power Plant," in Proc. of the 9th International Conference on AC and DC Power Transmission 2010.
- [9] U. N. Gnanarathna, S. K. Chaudhary and A. M. Gole, "Multilevel Modular Converter for VSC-HVDC Transmission Applications: Control and Operational Aspects," in Proc. of the 16th National Power Systems Conference, NPSC 2010. Osmania University, 2010. pg. 405-410

- [10] U. N. Gnanarathna, A. M. Gole, A. D. Rajapakse, and S. K. Chaudhary, 'Loss Estimation of Modular Multi-Level Converters using Electro-Magnetic Transients Simulation' IPST 2011, Delft, The Netherlands.

8.4.3 Poster Publication

- [11] S. K. Chaudhary, R. Teodorescu, P. Rodriguez, A. M. Gole and P.C. Kjær, "Negative Sequence Controllers to Reduce Power Oscillations During Electric Faults in the Offshore Wind Power Grid," in IEEE-PES General Meeting 2010, Minneapolis. *It was awarded the 1st prize in the 'Graduate Student Poster Contest', at IEEE PES GM 2010 in Minneapolis.*

8.4.4 Paper Submitted to Journals

- [12] S. K. Chaudhary, R. Teodorescu, P. Rodriguez, and A. M. Gole, 'Negative Sequence Current Control in Wind Power Plants with VSC-HVDC Connection.' Submitted to *IEEE Trans. of Sust. Energy* on 24-Jun-2011. [Manuscript ID TSTE-00344-2011].

References

- [1] European Wind Energy Association, "Pure Power Wind Energy Targets for 2020 and 2030," 2009 update. Available at: <http://www.ewea.org>
- [2] Global Wind Energy Council, "Global Wind Report – Annual market update 2010," April 2010. Available at: <http://www.gwec.net>
- [3] P. Bresesti, W. L. Kling, R. L. Hendriks, and R. Vailati, "HVDC Connection of Offshore Wind Farms to the Transmission System," *IEEE Transactions on Energy Conversion*, vol. 22, no. 1, pp. 37-43, Mar. 2007.
- [4] S. K. Chaudhary, R. Teodorescu and P. Rodriguez, "Wind Farm Grid Integration Using VSC Based HVDC Transmission - An Overview," *Energy 2030 Conference, 2008. ENERGY 2008. IEEE*, pp. 1-7, 2008.
- [5] N. Flourentzou, V. G. Agelidis and G. D. Demetriades, "VSC-Based HVDC Power Transmission Systems: An Overview," *Power Electronics, IEEE Transactions on*, vol. 24; 24, pp. 592-602, 2009.
- [6] K. Eriksson, C. Liljegren and K. Sobrink, "HVDC light experiences applicable for power transmission from offshore wind power parks," in *42nd AIAA Aerospace Sciences Meeting and Exhibit, Reno, Nevada*. 2004.
- [7] L. Harnefors, "Control of VSC-HVDC transmission," in Tutorial Presented at the IEEE PESC, Rhodes, Greece, Jun 15-19, 2008. 2008.
- [8] F. Iov, P. Sorensen, A. -. Hansen and F. Blaabjerg, "Grid connection of active stall wind farms using a VSC based DC transmission system," *Power Electronics and Applications, 2005 European Conference on*, pp. 10 pp., 2005.
- [9] C. Feltes and I. Erlich, "Variable Frequency Operation of DFIG based Wind Farms connected to the Grid through VSC-HVDC Link," *Power Engineering Society General Meeting, 2007. IEEE*, pp. 1-7, 2007.
- [10] L. Xu, B.W. Williams, and L. Yao, "Multi-terminal DC transmission systems for connecting large offshore wind farms," *2008 IEEE PES General Meeting - Conversion and Del. of Electrical Energy in the 21st Century*, IEEE, 2008, pp. 1-7.
- [11] Grid Code for High and Extra High Voltage, E.ON Netz GmbH Bayreuth, April 1, 2006.
- [12] Requirements for Offshore Grid Connections in the E.ON Netz Network, E.ON Netz GmbH Bayreuth, April 1, 2008.
- [13] Wind Turbines Connected to Grids with Voltages above 100kV – Technical regulation for the properties and the regulation of wind turbines,

Regulation TF 3.2.5, registered with the Danish Energy Authority on Dec 3, 2004.

- [14] A. A. Meer, R. L. Hendriks and W. L. Kling, "A survey of fast power reduction methods for VSC connected wind power plants consisting of different turbine types," presented at 2nd EPE Wind Energy Chapter Seminar, KTH, Stockholm, 23-24 April 2009.
- [15] C. Feltes, H. Wrede, F. W. Koch and I. Erlich, "Enhanced Fault Ride-Through Method for Wind Farms Connected to the Grid Through VSC-Based HVDC Transmission," *Power Systems, IEEE Transactions on*, vol. 24, pp. 1537-1546, 2009.
- [16] S. M. Mueeen, R. Takahashi, T. Murata, J. Tamura, M. H. Ali, Y. Matsumura, A. Kuwayama and T. Matsumoto, "Low voltage ride through capability enhancement of wind turbine generator system during network disturbance," *Renewable Power Generation, IET*, vol. 3; 3, pp. 65-74, 2009.
- [17] S. M. Mueeen, R. Takahashi, M. H. Ali, T. Murata and J. Tamura, "Transient Stability Augmentation of Power System Including Wind Farms by Using ECS," *Power Systems, IEEE Transactions on*, vol. 23; 23, pp. 1179-1187, 2008.
- [18] Annex of O.P. 12.2 Restricted to the technical requirements of wind power and photovoltaic facilities (Draft), by Red Electrica in October 2008 www.ree.es (translated in English by Spanish Wind Association AEE www.aeolica.es).
- [19] J. Morren, S. W. H. de Haan, W. L. Kling, and J. a Ferreira, "Wind Turbines Emulating Inertia and Supporting Primary Frequency Control," *IEEE Transactions on Power Systems*, vol. 21, no. 1, pp. 433-434, Feb. 2006.
- [20] N. R. Ullah, T. Thiringer, and D. Karlsson, "Temporary Primary Frequency Control Support by Variable Speed Wind Turbines— Potential and Applications," *IEEE Transactions on Power Systems*, vol. 23, no. 2, pp. 601-612, May. 2008.
- [21] B. H. Chowdhury and H. T. Ma, "Frequency regulation with wind power plants," 2008 IEEE Power and Energy Society General Meeting - Conversion and Delivery of Electrical Energy in the 21st Century, pp. 1-5, Jul. 2008.
- [22] S. Jensen, F.W. Fuchs, C.-albrechts-university Kiel, and D.- Kiel, "Load-Frequency Control of Synchronous Areas Using a Wind Farm

Connected via HVDC-VSC,” *2nd EPE Wind Energy Chapter Seminar, KTH, Stockholm, 23-24 April*, Stockholm, Sweden: 2009.

- [23] A. Lesnicar and R. Marquardt, “A new modular voltage source inverter topology,” in *Proc. EPE*, 2003.
- [24] B. Jacobson, P. Karlsson, G. Asplund, L. Harnefors, and T. Jonsson, “VSC-HVDC Transmission with Cascaded Two-Level Converters Converter Topology and Main Circuit,” in *CIGRE Session 2010*, 2010.
- [25] Huang H., “Multilevel Voltage-Sourced Converters for HVDC and FACTS Applications,” *Cigré SC B4 2009 Colloquium, B4-401, Bergen, Norway*.
- [26] C. Davidson and D. Trainer, “Innovative concepts for hybrid multi-level converters for HVDC power transmission,” in *AC and DC Power Transmission, 2010. ACDC. 9th IET International Conference on*, 2010, pp. 1–5.

Chapter 2

- [27] M. Liserre, R. Cardenas, M. Molinas, and J. Rodriguez, “Overview of Multi-MW Wind Turbines and Wind Parks,” *IEEE Transactions on Industrial Electronics*, vol. 58, Apr. 2011, pp. 1081-1095
- [28] A. D. Hansen, “Generators and Power Electronics for Wind Turbines”, in *Wind Power in Power Systems*, Ed. T. Ackermann, Chicester, U.K. Wiley, 2006, ISBN:0-470-85508-8.
- [29] J.G. Slootweg, H. Polinder, and W.L. Kling, “Reduced Order Modelling of Wind Turbines”, in *Wind Power in Power Systems*, Ed. T. Ackermann, Chicester, U.K. Wiley, 2006, ISBN-0-470-85508-8.
- [30] S. Heier, *Grid Integration of Wind Energy Conversion Systems*, Chicester, U.K. Wiley, 2006.
- [31] H. Li and Z. Chen, “Overview of different wind generator systems and their comparisons,” *Renewable Power Generation, IET*, vol. 2, 2008, pp. 123-138.
- [32] P. Anderson and A. Bose, “Stability Simulation of Wind Turbine Systems,” *IEEE Transactions on Power Apparatus and Systems*, vol. 102, no. 12, pp. 3791-3795, Dec. 1983.
- [33] N. P. W. Strachan and D. Jovcic, “Stability of a Variable-Speed Permanent Magnet Wind Generator With Weak AC Grids,” *IEEE Transactions on Power Delivery*, vol. 25, no. 4, pp. 2779-2788, Oct. 2010.

- [34] N. P. W. Strachan and D. Jovicic, "Improving wind power quality using an integrated Wind Energy Conversion and Storage System (WECSS)," *2008 IEEE Power and Energy Society General Meeting - Conversion and Delivery of Electrical Energy in the 21st Century*, pp. 1-8, Jul. 2008.
- [35] P. Christiansen, K. Jørgensen, and A. Sørensen, "Grid connection and remote control for the Horns Rev 150 MW offshore wind farm in Denmark," in *Proceedings of the 2nd International Workshop on Transmission Networks for Offshore Wind Farms*, 2008, pp. 29–30.
- [36] P. Kundur, *Power system stability and control*, Ed. N. J. Balu, M. G. Lauby, McGraw-Hill, 1994, ISBN-0-07-035958.
- [37] T. Ackermann, "Transmission Systems for Offshore Wind Farms", in *Wind Power in Power Systems*, Ed. T. Ackermann, Chicester, U.K. Wiley, 2006.
- [38] http://www.tennetso.de/pages/tennetso_en/Tasks/Offshore/Our_projects/index.htm
- [39] B. Normark and E. K. Nielsen, "Advanced power electronics for cable connection of offshore wind," presented at the Copenhagen OffshoreWind Conf., Copenhagen, Denmark, Oct. 26–28, 2005
- [40] T. Ahndorf, R. Witzmann, and S. Bopp, "The German offshore grid—A successful integration of offshore wind power," in *European Offshore Wind Conference*, 2007, December, pp. 4-6.
- [41] U. N. Gnanarathna, S. K. Chaudhary, A. M. Gole and R. Teodorescu, "Modular Multi-level converter based HVDC System for Grid Connection of Offshore Wind Power Plant," in *Proc. of the 9th International Conference on AC and DC Power Transmission 2010*.
- [42] U. N. Gnanarathna, S. K. Chaudhary and A. M. Gole, "Multilevel Modular Converter for VSC-HVDC Transmission Applications: Control and Operational Aspects," in *Proc. of the 16th National Power Systems Conference, NPSC 2010*. Osmania University, 2010. pg. 405-410
- [43] U. N. Gnanarathna, A. M. Gole, A. D. Rajapakse, and S. K. Chaudhary, 'Loss Estimation of Modular Multi-Level Converters using Electro-Magnetic Transients Simulation' *IPST 2011*, Delft, The Netherlands.

Chapter 3

- [44] D. G. Holmes and T. A. Lipo, *Pulse Width Modulation for Power Converters: Principles and Practice*, John Wiley & Sons, Inc., 2003.

- [45] C. Du, VSC-HVDC for Industrial Power Systems, Ph.D Thesis, Chalmers University of Technology, Göteborg, Sweden 2007.
- [46] P. Sandeberg and L. Stendius, "Large scale offshore wind power energy evacuation by hvdc light®," *European Wind Energy Conference & Exhibition*, 2008.
- [47] IEEE PES wind plant collector system design working group "Wind power plant collector system design considerations", IEEE, 2009.
- [48] E. Muljadi, C.P. Butterfield, a Ellis, J. Mechenbier, J. Hochheimer, R. Young, N. Miller, R. Delmerico, R. Zavadil, and J.C. Smith, "Equivalencing the collector system of a large wind power plant," *2006 IEEE Power Engineering Society General Meeting*, 2006, p. 9 pp.
- [49] R. van de Sandt, J. Lowen, J. Paetzold, and I. Erlich, "Neutral earthing in off-shore wind farm grids," *2009 IEEE Bucharest PowerTech*, pp. 1-8, Jun. 2009.
- [50] C. Feltes, R. van de Sandt, F. Koch, F. Shewarega, and I. Erlich, "Neutral grounding in wind farm medium voltage collector grids," in *2011 IEEE/PES Power Systems Conference and Exposition*, 2011, pp. 1-7.
- [51] A. S. Locker and M. S. Scarborough, 'Safer and Smarter Systems', *IEEE Industry Applications Magazine*, Vol. 16, No. 5, Sep-Oct 2010.
- [52] E.R. Detjen and K.R. Shah, "Grounding transformer applications and associated protection schemes," *IEEE Transactions on Industry Applications*, vol. 28, 1992, pp. 788-796.
- [53] P. Rodriguez, A. Luna, M. Ciobotaru, R. Teodorescu, and F. Blaabjerg, "Advanced Grid Synchronization System for Power Converters under Unbalanced and Distorted Operating Conditions," in *IECON 2006 - 32nd Annual Conf. on IEEE Ind. Electron.*, 2006, no. 2, pp. 5173-5178.

Chapter 4

- [54] P. Rodriguez, A. Luna, I. Candela, R. Mual, R. Teodorescu, and F. Blaabjerg, "Multiresonant Frequency-Locked Loop for Grid Synchronization of Power Converters Under Distorted Grid Conditions," *IEEE Transactions on Industrial Electronics*, vol. 58, no. 1, pp. 127-138, Jan. 2011.
- [55] ABB review 4/2008: The future is now (on the offshore HVDC light link NordE.ON 1, germany). Available: <http://www.abb.com/>

- [56] N.. Mohan, T. M. Undeland and W. P. Robbins, *Power Electronics Converters, Applications, and Design*; 3rd ed., NJ: John Wiley & Sons, 2003.
- [57] J. Conroy and R. Watson, "Aggregate modelling of wind farms containing full-converter wind turbine generators with permanent magnet synchronous machines: transient stability studies," *Renewable Power Generation, IET*, vol. 3, pp. 39-52, 2009.
- [58] A. A. van der Meer, R. L. Hendriks, and W. L. Kling, "A survey of fast power reduction methods for VSC connected wind power plants consisting of different turbine types," in *2nd EPE Wind Energy Chapter Seminar, KTH, Stockholm, 23-24 April, 2009*.

Chapter 5

- [59] S. Patel, "GLOBAL MONITER", *Power*, Vol. 154 Issue 11, pp. 8-15, Nov. 2010.
- [60] D. Turcotte and F. Katiraei, "Fault contribution of grid-connected inverters," in *2009 IEEE Electrical Power & Energy Conference (EPEC)*, 2009, pp. 1-5.
- [61] G. Ramtharan, A. Arulampalam, J. B. Ekanayake, F. M. Hughes, and N. Jenkins, "Fault ride through of fully rated converter wind turbines with AC and DC transmission systems," *IET Renewable Power Generation*, vol. 3, no. 4, p. 426, 2009.
- [62] A. D. Hansen and G. Michalke, "Multi-pole permanent magnet synchronous generator wind turbines' grid support capability in uninterrupted operation during grid faults," *IET Renewable Power Generation*, vol. 3, no. 3, p. 333, 2009.
- [63] E. J. Coster, J. M. A. Myrzik, B. Kruimer, and W. L. Kling, "Integration Issues of Distributed Generation in Distribution Grids," *Proceedings of the IEEE*, vol. 99, no. 1, pp. 28-39, Jan-2011.
- [64] S. M. Brahma and A. A. Girgis, "Development of Adaptive Protection Scheme for Distribution Systems With High Penetration of Distributed Generation," *IEEE Transactions on Power Delivery*, vol. 19, no. 1, pp. 56-63, Jan. 2004.
- [65] H. J. Laaksonen, "Protection Principles for Future Microgrids," *Power Electronics, IEEE Transactions on*, vol. 25, no. 12, pp. 2910-2918, 2010.
- [66] J. Cardenas, V. Muthukrishnan, D. McGinn, and R. Hunt, "Wind farm protection using an IEC 61850 process bus architecture," in *10th IET*

International Conference on Developments in Power System Protection (DPSP 2010). Managing the Change, 2010, p. P10-P10.

- [67] P. Christiansen, K. Jørgensen, and A. Sørensen, "Grid connection and remote control for the Horns Rev 150 MW offshore wind farm in Denmark," in *Proceedings of the 2nd International Workshop on Transmission Networks for Offshore Wind Farms*, 2008, pp. 29–30. Available: http://www.hornsrev.dk/engelsk/nyheder/nyh_aug_02/grid_control.pdf
- [68] *IEEE Standard Inverse-Time Characteristic Equations for Over-Current Relays*, IEEE Std C37.112-1996, Sep. 1996.
- [69] IEEE PES Wind Plant Collector System Design Working Group, "Wind plant collector system fault protection and coordination," *IEEE PES Trans. and Dist. Conf. and Exposition 2010*, , Apr. 2010

Chapter 6

- [70] C.H. Ng, L. Ran, and J. Bumby, "Unbalanced-Grid-Fault Ride-Through Control for a Wind Turbine Inverter," *IEEE Trans. on Ind. Appl.*, vol. 44, 2008, pp. 845-856.
- [71] R. Teodorescu, I. Liserre, Marco, and P. Rodriguez, "Control of Grid Converters under Grid Faults," *Grid Converters for Photovoltaic and Wind Power Systems*, IEEE-Wiley, 2011.
- [72] S. Alepuz, S. Busquets-Monge, J. Bordonau, J. a Martinez-Velasco, C. a Silva, J. Pontt, and J. Rodriguez, "Control Strategies Based on Symmetrical Components for Grid-Connected Converters Under Voltage Dips," *IEEE Trans. Ind. Electron.*, vol. 56, Jun. 2009, pp. 2162-2173.
- [73] D. Roiu, R.I. Bojoi, L.R. Limongi, and a Tenconi, "New Stationary Frame Control Scheme for Three-Phase PWM Rectifiers Under Unbalanced Voltage Dips Conditions," *IEEE Trans. Ind. Appl.*, vol. 46, 2010, pp. 268-277.
- [74] L. Xu, B.R. Andersen, and P. Cartwright, "VSC Transmission Operating Under Unbalanced AC Conditions—Analysis and Control Design," *IEEE Trans. on Power Del.*, vol. 20, Jan. 2005, pp. 427-434.
- [75] L. Xu, L. Yao, and C. Sasse, "Grid Integration of Large DFIG-Based Wind Farms Using VSC Transmission," *IEEE Trans. on Power Syst.*, vol. 22, pp. 976-984, Aug. 2007.
- [76] P. Rodriguez, A. Luna, M. Ciobotaru, R. Teodorescu, and F. Blaabjerg, "Advanced Grid Synchronization System for Power Converters under

Unbalanced and Distorted Operating Conditions,” in *Proc. of IECON*, Nov. 2006, pp. 5173-5178.

- [77] P. Rodriguez, A.V. Timbus, R. Teodorescu, M. Liserre, and F. Blaabjerg, “Flexible Active Power Control of Distributed Power Generation Systems During Grid Faults,” *IEEE Trans Ind. Electron.*, vol. 54, pp. 2583-2592, Oct. 2007.

Chapter 7

- [78] M. Hirakami and W. Neugebauer, “Transient Network Analyzer Operation with Digital Computer Control and Analysis,” *IEEE Transactions on Power Apparatus and Systems*, vol. 100, no. 4, pp. 1597-1607, Apr. 1981.
- [79] R. C. Durie and C. Pottle, “An extensible real-time digital transient network analyzer,” *IEEE Transactions on Power Systems*, vol. 8, no. 1, pp. 84-89, 1993.
- [80] P. Forsyth, T. Maguire, and R. Kuffel, “Real time digital simulation for control and protection system testing,” in *2004 IEEE 35th Annual Power Electronics Specialists Conference (IEEE Cat. No.04CH37551)*, 2004, pp. 329-335.
- [81] ABB Oy, Distribution Automation, ‘Feeder Protection and Control REF615 Product Guide’. Available at: www.abb.com/substationautomation
- [82] H. Kirmann, ‘Sampling Redundancy,’ in *ABB Review -Special Report IEC 61850*, ABB Group R & D and Technology, Switzerland 2010. ISSN: 1013-3119. Available at: www.abb.com/abbreview.
- [83] A. Hakala-Ranta, O. Rintamaki, and J. Starck, “Utilizing possibilities of IEC 61850 and GOOSE,” in *Electricity Distribution-Part 1, 2009. CIRED 2009*.

Appendix A - Main Circuit Parameters

A.1. Onshore Grid

Short circuit capacity, $S_k = 10$

Rated WPP Power, $P_n = 400 \text{ MW}$

Assuming a power factor of 0.9 gives system MVA of 444.44 MVA.
System base is taken as 450MVA

Grid Angle, $\phi_g = 84.3^\circ$

Angular Frequency, $\omega = 2\pi 50 \text{ Hz} = 314.16 \frac{\text{rad}}{\text{s}}$

Grid Impedance, $Z_g = \left(\frac{kV_n^2}{P_n} \right) \frac{1}{S_k} = \frac{400^2}{444.4} = 35.96 \Omega \angle 84.3^\circ$

Grid Resistance, $R_g = Z_g \cos \phi_g = 3.57 \Omega$

Grid Reactance, $X_g = Z_g \sin \phi_g = 35.78 \Omega$

Grid Inductance, $L_g = \frac{X_g}{\omega} = 113.9 \text{ mH}$

A.2. Converter Transformer:

Voltage Ratio: $\frac{400 \text{ kV}}{170 \text{ kV}}$ (onshore), $\frac{150 \text{ kV}}{170 \text{ kV}}$ (offshore)

Leakage Reactance, $x_{tr} = 0.14 \text{ pu}$

$MVA = \frac{400}{0.9} = 444.44 \sim 450 \text{ MVA}$

No load losses = 0.005 pu

Copper losses = 0.005 pu

A.3. Tuned Shunt Filters:

A.3.1. Filter-I (39th harmonic)

Resonant Frequency, $\omega_{10} = 2\pi 1950 = 12,353 \text{ rad} \cdot \text{s}^{-1}$

Quality Factor, $Q_1 = 25$

Var Compensation, $\text{Var}_1 = 0.06 \text{ pu} = 27 \text{ Mvar}$

Capacitance, $C_1 = \frac{\text{Var}_1}{2\pi f \cdot V_n^2} = 2.97 \mu\text{F}$

Resistance, $R_1 = \frac{Q_1}{\omega_{10} C_1} = 686.1 \Omega$

$$\text{Inductance, } L_1 = \frac{1}{\omega_{10}^2 C_1} = 2.24 \text{ mF}$$

$$\text{Impedance at 1950 Hz, } \omega_{r1} = 1.097 \Omega, \angle -2.2^\circ$$

A.3.2. Filter#2 parameters

$$\text{Resonant Frequency, } \omega_{10} = 2\pi 3900 = 24504 \text{ rad} \cdot \text{s}^{-1}$$

$$\text{Quality Factor, } Q_2 = 6$$

$$\text{Var Compensation, } Var_2 = 0.03 \text{ pu} = 13.5 \text{ Mvar}$$

$$\text{Capacitance, } C_2 = \frac{Var_2}{2\pi f \cdot V_n^2} = 1.91 \mu\text{F}$$

$$\text{Resistance, } R_2 = \frac{Q_2}{\omega_{20} C_2} = 128.2 \Omega$$

$$\text{Inductance, } L_{12} = \frac{1}{\omega_{20}^2 C_2} = 0.872 \text{ m}$$

Table A.1 Filter Impedance at the fundamental, 3rd harmonic and resonance

| | Impedance at 50 Hz | Impedance at 150 Hz | Impedance at Resonance |
|--------------------------------------|-----------------------|------------------------|---------------------------|
| Filter-I (39 th harmonic) | 1069.7Ω, ∠-90° | 354.7 Ω, ∠-90° | 1.1 Ω, ∠-2.3° |
| Filter#2 (78 th harmonic) | 2140.4 Ω, ∠-90° | 712.5 Ω, ∠-90° | 4.5 Ω, ∠-9.4° |

A.4. Phase Reactor

$$\text{pu impedance} = 0.12$$

$$\text{Base impedance, } Z_b = \frac{kV^2}{MVA} = \frac{170^2}{450} = 50\Omega$$

$$\text{Inductance, } L_{pr} = 0.12 Z_b * \frac{50}{2\pi f} = 24.5 \text{ mH}$$

A.5. VSC –HVDC System

$$\text{Switching Frequency} = 1950 \text{ Hz}$$

$$\text{DC link voltage, } V_{DC} = 300 \text{ kV (pole to pole)}$$

$$\text{DC Power, } P_{DC} = 400 \text{ MW}$$

$$\text{DC Current, } I_{DC} = \frac{P_{DC}}{V_{DC}} = 1.333 \text{ kA}$$

$$\text{Dc capacitor time constant, } \tau_{DC} = 2 \text{ ms}$$

$$\text{DC capacitance, } C_{dc} = 2 * \frac{P_{DC} \tau_{DC}}{V_{DC}^2} = 17.78 \mu\text{F}$$

A.6. DC cable parameters

Copper cable with 1.2 A per sq. mm current density is assumed. XLPE insulation thickness of 12 mm is assumed for ± 150 kV DC cables.

$$\text{Current density} = 1.2 \text{ A. mm}^{-2}$$

$$\text{Cross Section, } A = \frac{1334}{1.2} = 1112 \text{ mm}^2$$

$$\text{Cu. -core radius} = 18.8 \text{ mm}$$

$$\text{Insulation thickness} = 12 \text{ mm}$$

$$\rho_{cu} = 1.68 \times 10^{-8} \Omega \cdot \text{m}$$

$$\text{Length, } l = 200 \text{ km}$$

$$\text{Resistance, } R_{cable} = \frac{\rho_{cu} l}{A} = 3.09 \Omega$$

$$\text{Capacitance, } C_{cable} = \frac{2\pi\epsilon_0\epsilon_r}{\ln\left(\frac{r_2}{r_1}\right)} = 0.315 \mu\text{F/km}$$

$$\text{Inductance, } L_{cable} = 0.2 \ln\left(\frac{GMD}{GMR}\right) = 0.2 \ln\frac{0.1}{0.7788 * 0.0188} = 0.384 \frac{\text{mH}}{\text{km}} = 76.85 \text{ mH}$$

Considering shielding by sheath at a radius of 30.8 mm, the inductance is given by,

$$\text{Inductance, } L_{cable} = 0.2 \ln\left(\frac{GMD}{GMR}\right) = 0.2 \ln\frac{0.0308}{.7788 * 0.0188} = 0.1487 \frac{\text{mH}}{\text{km}} = 29.74 \text{ mH}$$

A.7. 150 kV AC cable parameters

There are two 2-km long 150-kV cables connecting the converter transformer to the two plant step-up transformers at the collector bus. The nominal power rating of the plant is 400 MW implies that each cable should handle 200 MW. Further assuming a power factor of 0.9, each cable has to be rated for,

$$S_{cable150} = \frac{200}{0.9} = 222 \approx 225 \text{ MVA}$$

$$V_{cable150} = 150 \text{ kV}$$

$$I_{cable150} = \frac{S_{cable150}}{\sqrt{3}V_{cable150}} = 855.4 \text{ A}$$

Single core copper cable with 1200 mm² cross section has been selected from Table 4 of ABB XLPE cables data sheet. Cross bonded cable layout in flat formation gives a maximum current carrying capacity of 850 A and 1050 A for a temperature rise of 65°C and 90°C respectively. As per table 21, the

maximum dc resistance is $0.0151 \Omega/\text{km}$ at 20°C . In flat formation, the cable inductance is $0.5 \text{ mH}/\text{km}$ and its capacitance is $0.26 \mu\text{F}/\text{km}$.

A.8. Plant step up transformer

Three-winding transformers have been considered as plant step-up transformers.

Voltage ratio: 36/36/150 kV.

MVA = 111/111/222 MVA

Vector Connection: DDYn

Leakage Reactance: 0.24 pu between the 36kV windings
0.12 pu between the 36kV and 150kV windings

A.9. Grounding Transformer

The zig-zag connected grounding transformers have been considered here for the grounding of the medium voltage (MV) WTG cable feeders. The transformer leakage reactance is assumed to be 0.1 pu, on a base of 100 MVA. No load and core losses are assumed to 0.005 pu each.

A.10. L-C-L filter for WTG

The LCL filter was designed for the GSC of a 6.6 MVA WTG-FSC operating at the 3.3kV rms ac line-line voltage. The LCL parameters were:

| | | |
|---------------------|------------------|----------|
| $MVA_b =$ | 6.6 MVA | |
| $kV_b =$ | 3.3 kV | |
| $L1 =$ | $481\mu\text{H}$ | 0.093 pu |
| $L2 =$ | $260\mu\text{H}$ | 0.05 pu |
| $C =$ | $372\mu\text{F}$ | 5.238 pu |
| $L_t + L_g + L_2 =$ | $936\mu\text{H}$ | 0.18 pu |
| $L_t + L_g =$ | $676\mu\text{H}$ | 0.13 pu |

It has been scaled to an equivalent LCL filter for a 111MVA WTG-FSC operating at the 3.3 kV RMS ac line-line voltage. This change will effectively decrease the impedances by a factor of $\frac{111}{6.6} = 16.82$. The admittances will be increased by the same factor. Thus, the new values are given by,

$$\begin{aligned}
MVA_{b2} &= 111 \text{ MVA} \\
kV_b &= 3.3 \text{ kV} \\
L1 &= 28.6 \mu H & 0.093 \text{ pu} \\
L2 &= 15.46 \mu H & 0.05 \text{ pu} \\
C &= 6256 \mu F & 5.238 \text{ pu} \\
L_t + L_g + L_2 &= 55.65 \mu H & 0.18 \text{ pu} \\
L_t + L_g &= 40.19 \mu H & 0.13 \text{ pu}
\end{aligned}$$

A.11. WTG unit transformer

The unit transformer for the aggregated WTG have been selected with the following ratings:

$$\begin{aligned}
MVA &= 111 \text{ MVA} \\
kV &= 3.3/36 \text{ kV} \\
Config. &= ynd \\
x_l &= 15.46 \mu H \\
Losses &= 0.005 \text{ pu (no load),} \\
&0.005 \text{ pu (Cu loss)}
\end{aligned}$$

A.12. WTG feeder cables

A typical layout of WTGs in a wind power plant is shown in Figure 3.7. The WTG string can be made up of cables with increasing cross sections depending upon the number of WTGs connected to it. In this case, two cross sections have been considered for the cables.

Each WTG is rated for 6.7MW or 7.41MVA at 0.9 power factor. Therefore, each WTG will supply a current of 118.7A in the 36 kV cable strings. The combined current of the first two WTGs will be 237.4A, and hence 95 sq.mm core copper cable has been considered for the connection of first two WTGs in the string. When the next two WTGs are connected, the total feeder current becomes 474.7A. A 240 sq. mm cable has been selected for this section of the WTG string. The combined current of all 5 WTGs is 593.4 A. Hence a 400 sq. mm cable section is used to connect the 5 WTG units with the collector bus. It is assumed that there is a distance of 1km cable length between two adjacent WTG units and between the collector bus and its adjacent WTG unit.

The cable selection is based upon the underground cable datasheet [A-2]. Considering a temperature rise of 65°C in cross-bonding and trefoil layout, the current carrying capacities are 270A and 6590 A for the selected cables. It should be updated with the submarine cable datasheet.

Cable parameters:

- (1) $X_{1_section} = 95 \text{ mm}^2, 270 \text{ A}$ $r_1 = 0.193 \text{ } \Omega/\text{km}$ $l_1 = 0.69 \text{ mH/km}$ $c_1 = 0.17 \text{ } \mu\text{F/km}$
 (2) $X_{2_section} = 240 \text{ mm}^2, 475 \text{ A}$ $r_2 = 0.0754 \text{ } \Omega/\text{km}$ $l_2 = 0.60 \text{ mH/km}$ $c_2 = 0.23 \text{ } \mu\text{F/km}$
 (3) $X_{3_section} = 400 \text{ mm}^2, 625 \text{ A}$ $r_3 = 0.047 \text{ } \Omega/\text{km}$ $l_3 = 0.57 \text{ mH/km}$ $c_3 = 0.28 \text{ } \mu\text{F/km}$

For the equivalent cable string shown in **Error! Reference source not found.(b)**, the
 able parameters are given by,

$$Z_{eq} = \frac{\sum_{m=1}^n m^2 Z_m}{n^2}$$

$$B_{tot} = \sum_{i=1}^n B_i$$

The parameters of the equivalent cable string is thus,

$$Eq. \text{ cable string} \quad r_{eqstr} = 0.161 \text{ } \Omega \quad l_{eqstr} = 1.308 \text{ mH} \quad c_{eqstr} = 1.08 \text{ } \mu\text{F}$$

The parameters of the aggregated WTG feeder can be calculated by the parallel combination of these strings, which gives the parameters of the aggregated cable feeder as follows,

$$r_{fr} = \frac{r_{eqstr}}{3} = 0.0537 \text{ } \Omega \quad l_{fr} = \frac{l_{eqstr}}{3} = 0.436 \text{ mH} \quad c_{fr} = 3c_{eqstr} = 3.24 \text{ } \mu\text{F}$$

References:

- [A-1] E. Muljadi, C.P. Butterfield, a Ellis, J. Mechenbier, J. Hochheimer, R. Young, N. Miller, R. Delmerico, R. Zavadil, and J.C. Smith, "Equivalencing the collector system of a large wind power plant," *2006 IEEE Power Engineering Society General Meeting*, 2006, p. 9 pp.
 [A-2] XLPE Cable Systems, User's Guide, ABB Ltd

Appendix B -Phase Transformations and Sequence Components

The three phase voltage or current variables are assumed along three axes separated in space by 120° so as to reflect their phase angle relationship. These can be transformed into space phasors along the two orthogonal axes. The Park's and Clarke's transformations are the two standard transformations.

B.1 Park's Transformation

It transforms a three phase voltage (or current) to the two phase components at quadrature in the synchronously rotating reference frame.

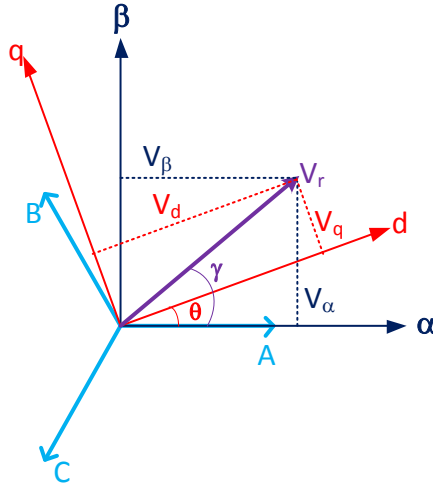


Fig. B. 1 Three phases, and space vectors in stationary and rotating reference frames.

In most of the applications, the rotating reference frame is rotating at the synchronous speed, ω .

$$\theta = \omega t \quad (B.1)$$

$$\gamma = \theta + \delta \quad (B.2)$$

$$V_r = v_d + jv_q = v_a e^{-j\gamma} + v_b e^{-j(\gamma - \frac{2\pi}{3})} + v_c e^{-j(\gamma - \frac{4\pi}{3})} \quad (B.3)$$

$$v_d + jv_q = V_r e^{j(\gamma - \theta)} = v_a e^{-j\theta} + v_b e^{-j(\theta - \frac{2\pi}{3})} + v_c e^{-j(\theta - \frac{4\pi}{3})} \quad (B.4)$$

$$\begin{bmatrix} v_d \\ v_q \\ v_0 \end{bmatrix} = \frac{2}{3} \begin{bmatrix} \cos \theta & \cos\left(\theta - \frac{2\pi}{3}\right) & \cos\left(\theta - \frac{4\pi}{3}\right) \\ -\sin \theta & -\sin\left(\theta - \frac{2\pi}{3}\right) & -\sin\left(\theta - \frac{4\pi}{3}\right) \\ \frac{1}{2} & \frac{1}{2} & \frac{1}{2} \end{bmatrix} \begin{bmatrix} v_a \\ v_b \\ v_c \end{bmatrix} \quad (\text{B.5})$$

or, $[v_{dq0}] = [T_{abc2dq}][v_{abc}]$

The inverse transformation is given by,

$$\begin{aligned} \therefore [v_{abc}] &= [T_{abc2dq}]^{-1} [v_{dq0}] \\ \begin{bmatrix} v_a \\ v_b \\ v_c \end{bmatrix} &= \begin{bmatrix} \cos \theta & -\sin \theta & 1 \\ \cos\left(\theta - \frac{2\pi}{3}\right) & -\sin\left(\theta - \frac{2\pi}{3}\right) & 1 \\ \cos\left(\theta - \frac{2\pi}{3}\right) & -\sin\left(\theta - \frac{4\pi}{3}\right) & 1 \end{bmatrix} \begin{bmatrix} v_d \\ v_q \\ v_0 \end{bmatrix} \end{aligned} \quad (\text{B.6})$$

In complex phasor notation,

$$v_a = \text{Re}\{(v_d + jv_q)e^{-j\theta}\} + v_0 \quad (\text{B.7})$$

$$v_b = \text{Re}\left\{(v_d + jv_q)e^{-j\left(\theta - \frac{2\pi}{3}\right)}\right\} + v_0 \quad (\text{B.8})$$

$$v_c = \text{Re}\left\{(v_d + jv_q)e^{-j\left(\theta - \frac{4\pi}{3}\right)}\right\} + v_0 \quad (\text{B.9})$$

The coefficient 2/3 ensures that the magnitudes of v_d and v_q remain the same as the peak magnitude of v_a , for a balanced three phase system. This transformation is not power invariant. The instantaneous power is given by,

$$\begin{aligned} P_t &= [v_a \quad v_b \quad v_c][i_a \quad i_b \quad i_c]^t = [v_{abc}]^t[i_{abc}] \\ \text{Or,} \\ P_t &= ([T_{abc2dq}]^{-1}[v_{dq0}])^t ([T_{abc2dq}]^{-1}[i_{dq0}]) \\ \therefore [T_{abc2dq}]^{-1} &= \frac{3}{2} [T_{abc2dq}]^t \\ P_t &= \frac{3}{2} [v_{dq0}]^t [i_{dq0}] = \frac{3}{2} (v_d i_d + v_q i_q + v_0 i_0) \end{aligned} \quad (\text{B.10})$$

8.5 Clarke's Transformation

Clarke's transformation transforms the phase variable in the stationary frame of reference. The stationary reference frame has the two axes, α and β and the α axis is aligned with the axis of phase 'A', i.e. $\theta = 0$. Thus, the

stationary reference frame components can be obtained by substituting $\theta = 0$ in (B.5).

$$\begin{bmatrix} v_\alpha \\ v_\beta \\ v_0 \end{bmatrix} = \frac{2}{3} \begin{bmatrix} 1 & -\frac{1}{2} & -\frac{1}{2} \\ 0 & \frac{\sqrt{3}}{2} & -\frac{\sqrt{3}}{2} \\ \frac{1}{2} & \frac{1}{2} & \frac{1}{2} \end{bmatrix} \begin{bmatrix} v_a \\ v_b \\ v_c \end{bmatrix} \quad (\text{B.11})$$

The inverse Clarke's transformation is given by,

$$\begin{bmatrix} v_a \\ v_b \\ v_c \end{bmatrix} = \begin{bmatrix} 1 & 0 & 1 \\ -\frac{1}{2} & \frac{\sqrt{3}}{2} & 1 \\ -\frac{1}{2} & -\frac{\sqrt{3}}{2} & 1 \end{bmatrix} \begin{bmatrix} v_\alpha \\ v_\beta \\ v_0 \end{bmatrix} \quad (\text{B.12})$$

8.6 Relationship between Park's and Clarke's Transformations

The transformations between the rotating reference frame (Park's transformation) and the stationary reference frame, Clarke's transformation are given by,

$$(v_d + jv_q) = (v_\alpha + jv_\beta)e^{-j\theta}$$

$$\text{Or, } \begin{bmatrix} v_d \\ v_q \end{bmatrix} = \begin{bmatrix} \cos \theta & \sin \theta \\ -\sin \theta & \cos \theta \end{bmatrix} \begin{bmatrix} v_\alpha \\ v_\beta \end{bmatrix} \quad (\text{B.13})$$

$$(v_d + jv_q) = (v_\alpha + jv_\beta)e^{-j\theta}$$

$$\text{Or, } \begin{bmatrix} v_\alpha \\ v_\beta \end{bmatrix} = \begin{bmatrix} \cos \theta & -\sin \theta \\ \sin \theta & \cos \theta \end{bmatrix} \begin{bmatrix} v_d \\ v_q \end{bmatrix} \quad (\text{B.14})$$

8.8 Relationship between the Sequence Components and Clarke's Transformation

From (B.11) we have,

$$\begin{bmatrix} v_\alpha \\ v_\beta \end{bmatrix} = \frac{2}{3} \begin{bmatrix} 1 & -\frac{1}{2} & -\frac{1}{2} \\ 0 & \frac{\sqrt{3}}{2} & -\frac{\sqrt{3}}{2} \end{bmatrix} \begin{bmatrix} v_a \\ v_b \\ v_c \end{bmatrix} = [T_{\alpha\beta}] \begin{bmatrix} v_a \\ v_b \\ v_c \end{bmatrix} \quad (\text{B.15})$$

In absence of the negative sequence components, we can write,

$$\begin{bmatrix} v_a \\ v_b \\ v_c \end{bmatrix} = \left(\frac{3}{2}\right) [T_{\alpha\beta}]^T \begin{bmatrix} v_\alpha \\ v_\beta \end{bmatrix} \quad (\text{B.16})$$

Fortescue's transformation relates the positive and negative sequence components to the three-phase components by,

$$\begin{bmatrix} v_a^+ \\ v_b^+ \\ v_c^+ \end{bmatrix} = \frac{1}{3} \begin{bmatrix} 1 & \alpha & \alpha^2 \\ \alpha^2 & 1 & \alpha \\ \alpha & \alpha^2 & 1 \end{bmatrix} \begin{bmatrix} v_a \\ v_b \\ v_c \end{bmatrix} = [T_{abc}^+] \begin{bmatrix} v_a \\ v_b \\ v_c \end{bmatrix} \quad (\text{B.17})$$

$$\begin{bmatrix} v_a^- \\ v_b^- \\ v_c^- \end{bmatrix} = \frac{1}{3} \begin{bmatrix} 1 & \alpha^2 & \alpha \\ \alpha & 1 & \alpha^2 \\ \alpha^2 & \alpha & 1 \end{bmatrix} \begin{bmatrix} v_a \\ v_b \\ v_c \end{bmatrix} = [T_{abc}^-] \begin{bmatrix} v_a \\ v_b \\ v_c \end{bmatrix} \quad (\text{B.18})$$

If Clarke's transformation is applied on the positive sequence components in the phase domain, we get the positive sequence components in the stationary reference frame as follows,

$$\begin{bmatrix} v_\alpha^+ \\ v_\beta^+ \end{bmatrix} = \frac{2}{3} \begin{bmatrix} 1 & -\frac{1}{2} & -\frac{1}{2} \\ 0 & \frac{\sqrt{3}}{2} & -\frac{\sqrt{3}}{2} \end{bmatrix} \begin{bmatrix} v_a^+ \\ v_b^+ \\ v_c^+ \end{bmatrix} = [T_{\alpha\beta}] \begin{bmatrix} v_a^+ \\ v_b^+ \\ v_c^+ \end{bmatrix} \quad (\text{B.19})$$

From (B.18) and (B.19), we get

$$\begin{bmatrix} v_\alpha^+ \\ v_\beta^+ \end{bmatrix} = [T_{\alpha\beta}] [T_{abc}^+] \begin{bmatrix} v_a \\ v_b \\ v_c \end{bmatrix} \quad (\text{B.20})$$

From (B.17) and (B.20), we get

$$\begin{bmatrix} v_{\alpha}^{+} \\ v_{\beta}^{+} \end{bmatrix} = \left(\frac{3}{2}\right) [T_{\alpha\beta}] [T_{abc}^{+}] [T_{\alpha\beta}]^T \begin{bmatrix} v_{\alpha} \\ v_{\beta} \end{bmatrix}$$

$$\text{or,} \quad \begin{bmatrix} v_{\alpha}^{+} \\ v_{\beta}^{+} \end{bmatrix} = \frac{1}{2} \begin{bmatrix} 1 & -q \\ q & 1 \end{bmatrix} \begin{bmatrix} v_{\alpha} \\ v_{\beta} \end{bmatrix} \quad (\text{B.21})$$

where, $q = -\sqrt{-1} = e^{-j\frac{\pi}{2}}$

Similarly, the relationship between the negative sequence components and the stationary reference frame components can be derived as,

$$\begin{bmatrix} v_{\alpha}^{-} \\ v_{\beta}^{-} \end{bmatrix} = \left(\frac{3}{2}\right) [T_{\alpha\beta}] [T_{abc}^{-}] [T_{\alpha\beta}]^T \begin{bmatrix} v_{\alpha} \\ v_{\beta} \end{bmatrix}$$

$$\text{or,} \quad \begin{bmatrix} v_{\alpha}^{-} \\ v_{\beta}^{-} \end{bmatrix} = \frac{1}{2} \begin{bmatrix} 1 & q \\ -q & 1 \end{bmatrix} \begin{bmatrix} v_{\alpha} \\ v_{\beta} \end{bmatrix} \quad (\text{B.22})$$

Appendix C - Design of a PI Controller for the VSC-HVDC Controllers

Usually, the two terminals of a VSC-HVDC transmission system are identical as they have to handle the same amount of active power at the same voltage. The reactive power capabilities of the individual converter may differ in some cases. In the VSC-HVDC transmission described in chapter 3, the offshore grid converter establishes the ac reference voltage and frequency in the offshore grid. The onshore VSC-HVDC terminal regulates the dc line voltage and the ac voltage magnitude (or reactive power). In both cases, the main control function which may be the control of dc voltage, ac voltage or the reactive power, is implemented in the outer control loop. The outer controller sets the desired current reference which is attained by the fast inner current control loop. The block diagrams are given in Figure 3.14, 3.15 in Chapter 3. Here the tuning of the proportional integral controllers is described. Fig. C-1 gives the block diagram of the PI controllers and the plant.

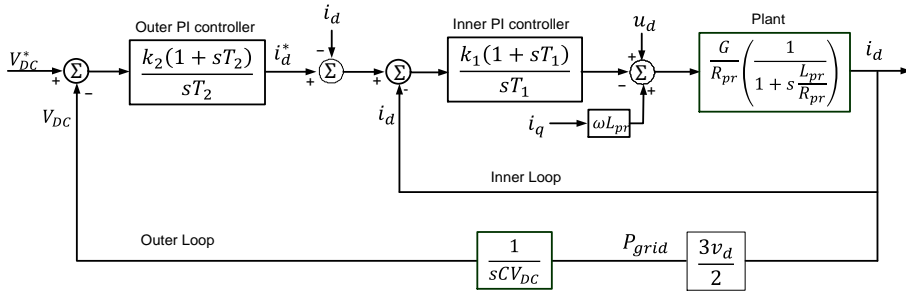


Fig. C. 1 Proportional-integral controller for the VSC-HVDC

C.1. Inner Current Loop

The plant comprises of a VSC connected to the filter bus through a phase reactor with the inductance (L_{pr}) and resistance (R_{pr}) as given below,

$$L_{pr} = 0.02453 \text{ H}, R_{pr} = 0.060 \Omega \rightarrow \tau = \frac{L}{R} = 0.4088s \quad (C.1)$$

$$\therefore T_1 = 0.4088s$$

After the open loop poles get cancelled, the remaining open loop transfer function is $\left(\frac{K_1 G}{s R_{pr} T_1}\right)$. In this implementation, the controller gain, G , is considered as unity. This means the VSC output is same as the controller reference. The closed loop transfer function becomes,

$$\frac{K_1 G}{K_1 G + s R_{pr} T_1} = \frac{1}{1 + s \left(\frac{R_{pr} T_1}{K_1 G}\right)} \quad (C.2)$$

Switching frequency is 1950 Hz. The bandwidth is selected as half decade lower than the switching frequency, i.e. 390 Hz (or 780π rad/sec). Hence,

$$\frac{1}{1 + s \left(\frac{R_{pr} T_1}{K_1 G}\right)} = \frac{1}{1 + \frac{s}{780\pi}} \quad (C.3)$$

$$\begin{aligned} \because T_1 &= 0.4088, G = 1, R_1 = 0.06\Omega \rightarrow K_1 \\ &= \frac{R_{pr} T_1}{G} 780\pi = 60.11, \end{aligned} \quad (C.4)$$

In PSCAD implementation of the PI controller, the parameters are given by,

$$K_p = K_1 = 60.11, T_1 = \left(\frac{T_1}{K_1}\right) = \frac{0.4088}{30.05} = 0.0068 \quad (C.5)$$

C.2. Outer DC-Voltage Control Loop (considering $T_s=1/1950s$)

After pole cancellation, the effective inner loop transfer function is $\left(\frac{1}{1 + \frac{s}{780\pi}}\right)$ Pole cancellation can be achieved by setting, $T_2 = \frac{1}{780\pi} = 0.00041$ s.

For the outer loop, the integral function $\left(\frac{1}{s}\right)$ is replaced by (ΔT) , which implies multiplication by the time period. Then the open loop transfer function becomes, $\left(\frac{K_2}{s T_2} \cdot \frac{3v_d \Delta T}{2CV_{DC}}\right) = \left(\frac{3v_d K_2 T_s}{2s CV_{DC} T_2}\right)$

The close loop transfer function is, $\left(\frac{1}{1 + \frac{2sCV_{DC}T_2}{3v_dK_2T_S}} \right)$

One decade lower bandwidth is selected at 19.5 Hz or $\left(39\pi \frac{rad}{s} \right)$.

$$\frac{2CV_{DC}T_2}{3v_dK_2T_S} = \frac{1}{39\pi} \leftrightarrow K_2 = 39\pi \left(\frac{2CV_{DC}T_2}{3v_dT_S} \right) = 0.00942$$

In PSCAD implementation, $K_{p2} = K_2 = 0.00942$ and $T_{i2} = \frac{T_2}{K_2} = 0.04332$

C.3. Reactive power control loop

For the reactive power control loop, the open loop transfer function is

$$\frac{K_{2q}}{sT_2} \left(\frac{3v_d}{2} \right) = \frac{3v_dK_{2q}}{2sT_2} \text{ The close loop transfer function becomes } \left(\frac{1}{1 + \frac{2sT_2}{3v_dK_{2q}}} \right).$$

Here, half-decade lower bandwidth is selected at 39 Hz or $\left(78\pi \frac{rad}{s} \right)$, on the basis of trial.

$$\frac{2T_2}{3v_dK_{2q}} = \frac{1}{78\pi} \leftrightarrow K_{2q} = 78\pi \left(\frac{2T_2}{3v_d} \right) = 0.00048 \text{ for 170 kV base.}$$

$$T_{i2q} = \frac{T_2}{K_{2q}} = 0.8497 \text{ for 170 kV ac bus voltage.}$$

C.4. Offshore ac voltage controller tuning

Neglecting the current injection from the WPP, the filter bus voltage and the current are related by the phase equation,

$$i_f^{abc} = C_f \frac{dv_f^{abc}}{dt}$$

Park's transformation gives,

$$\begin{aligned} i_f^d &= -\omega C_f v_f^q + C_f \frac{dv_f^d}{dt} \\ i_f^q &= \omega C_f v_f^d + C_f \frac{dv_f^q}{dt} \end{aligned}$$

If the cross coupling terms are ignored, and the current is considered constant for a switching cycle, the current to voltage gain is $\frac{v_f^d}{i_f^d} = \frac{\Delta T}{C_f} = \frac{T_S}{C_f}$

The open loop transfer function is, $\frac{\Delta v_f}{v_f^*(s)} = \frac{K_{2v}}{sT_2} \left(\frac{\Delta T}{C_f} \right) = \frac{K_{2v}}{sT_2} \left(\frac{T_S}{C_f} \right) = \frac{K_{2v}T_S}{sT_2C_f}$

The closed loop transfer function becomes, $\left(\frac{\frac{1}{sT_2C_f}}{1 + \frac{K_{2v}T_S}{sT_2C_f}} \right)$

Half decade lower bandwidth is selected at 39 Hz or $\left(78\pi \frac{\text{rad}}{s} \right)$.

$$\frac{T_2C_f}{K_{2v}T_S} = \frac{1}{78\pi} \leftrightarrow K_{2v} = 78\pi \left(\frac{T_2C_f}{T_S} \right) = 0.000858$$

$$T_{i2v} = \frac{T_2}{K_{2v}} = 0.4756$$

Table C. 1 PI controller parameters : Calculated values, and the values used in PSCAD simulation.

| Control Loop | Calculated Parameters | | Parameters used | |
|--------------------------------------|-----------------------|--------|-----------------|--------|
| | K_p | T_i | K_p | T_i |
| Current Control | 60.1 | 0.0068 | 47.3 | 0.0068 |
| Negative Sequence Current controller | 60.1 | 0.0068 | 60 | 1.0 |
| Dc voltage controller | 0.0094 | 0.0433 | 0.0056 | 0.0721 |
| Reactive power controller | 0.0005 | 0.850 | 0.0005 | 0.850 |
| AC voltage controller | 0.001 | 0.476 | 0.001 | 0.349 |
